

Heat transfer during transient spray cooling: An experimental and analytical study

Vom Fachbereich Maschinenbau
der Technischen Universität Darmstadt
zur
Erlangung des Grades eines Doktor-Ingenieurs (Dr.-Ing.)
genehmigte

Dissertation

vorgelegt von

Fabian Michael Tenzer, M.Sc.

aus Heppenheim

Berichterstatter:	Prof. Dr.-Ing. Cameron Tropea
1. Mitberichterstatter:	Apl. Prof. Dr. Ilia V. Roisman
2. Mitberichterstatter:	Prof. Dr.-Ing. Eckehard Specht
Tag der Einreichung:	20.01.2020
Tag der mündlichen Prüfung:	26.03.2020

Darmstadt 2020

Tenzer, Fabian Michael:

Heat transfer during transient spray cooling: An experimental and analytical study

Darmstadt, Technische Universität Darmstadt

Jahr der Veröffentlichung der Dissertation auf TUprints: 2020

Tag der mündlichen Prüfung: 26.03.2020

Bitte zitieren Sie dieses Dokument als:

URN: urn:nbn:de:tuda-tuprints-113442

URL: <https://tuprints.ulb.tu-darmstadt.de/id/eprint/11344>

Dieses Dokument wird bereitgestellt von TU Prints, E-Publishing-Service der Technischen Universität Darmstadt <http://tuprints.ulb.tu-darmstadt.de>
tuprints@ulb.tu-darmstadt.de



Veröffentlicht unter CC BY-SA 4.0 International:

Namensnennung - Weitergabe unter gleichen Bedingungen

<https://creativecommons.org/licenses/by-sa/4.0/>

Für Tom

Abstract

Spray cooling features a very high, homogeneously distributed cooling performance. Therefore it is used in various industrial applications, like cooling of high powered electronics, for quenching during metalworking or cooling of tools during hot forging. The cooling efficiency is influenced by a large number of parameters: drop diameter and velocity, mass flux, surface temperature, spray fluid and temperature, surface material and conditions, etc. The entire process is extremely complex and to date only few physical models exist describing the heat transfer rates as a function of these parameters. Instead, the heat flux is mainly predicted using empirical correlations, which are often not suited for conditions other than those from which they were derived - universality of these correlations is lacking. The present study strives to replace these empirical correlations with theories based on physics.

In this study the transient spray cooling of a hot thick target is experimentally and analytically investigated. The locally resolved temporal evolution of the heat flux and surface temperature of an initially homogeneously heated substrate is measured during continuous spray impact. This experimental quantification captures the influence of various spray features (droplet diameter, velocity and mass flux), spray impact angle, spray fluid temperature, wall thermal properties and wall surface roughness, whereby the mass flux is found to be the dominating factor in determining cooling performance. Furthermore, visual observations of spray impact at high surfaces temperatures beyond the Leidenfrost point identifies no closed liquid film separated from the surface by a vapor layer, as it is often imagined for these conditions. Instead, the spray impact is governed by a superposition of single drop impacts at a dry wall. Therefore, there is no risk of unintentionally flooding the surface, thus limiting the heat flux due to an inordinately high mass flux. Spraying a surface at an oblique angle, as well as spraying with hot fluid decreases the heat flux. Increasing the surface roughness or using substrates which have a high thermal conductivity results in higher cooling performances.

Theoretical models to predict the heat flux during spray cooling are developed and validated with experimental results. A model for the film boiling regime accounts for spray and wall properties and predicts the temporal evolution of surface temperature and heat flux. It agrees well with experimental data.

A theory for the nucleate boiling regime indicates that the heat flux is limited by the thermal inertia of the substrate material and is not a function of the spray properties.

Furthermore, the Leidenfrost point is found to be nearly independent of the spray properties. Instead, it is strongly influenced by the material of the substrate and fluid: A high thermal effusivity leads to a low Leidenfrost temperature and vice versa. This influence is captured in a newly developed theoretical prediction.

Kurzfassung

Die Sprühkühlung zeichnet sich durch eine sehr hohe und gleichmäßig verteilte Kühlleistung aus. Deshalb wird sie in einer großen Bandbreite von industriellen Prozessen eingesetzt, wie beispielsweise bei der Kühlung von Hochleistungselektronik, zum Abschrecken während der Metallherstellung oder zur Kühlung von Schmiedewerkzeugen in der Massivumformung. Die Effizienz der Kühlung wird von einer Vielzahl von Größen beeinflusst. Dazu zählen unter anderem: Tropfendurchmesser und -geschwindigkeit, Beaufschlagungsdichte, Oberflächentemperatur, das Spraymedium sowie dessen Temperatur, Material und Beschaffenheit der Oberfläche und viele mehr. Der gesamte Prozess ist extrem komplex und bis jetzt existieren nur sehr wenige physikalische Modelle, die diesen beschreiben. Stattdessen müssen zur Vorhersage des Wärmestroms empirische Korrelationen verwendet werden, die auf Grund von fehlender Universalität nicht immer zur entsprechenden Anwendung passen.

In dieser Arbeit wird die transiente Sprühkühlung eines heißen, dicken Körpers experimentell und analytisch untersucht. Hierbei wird die zeitliche Entwicklung der Wärmestromdichte und der Oberflächentemperatur während der kontinuierlichen Sprühkühlung des zu Beginn homogen erwärmten Körpers gemessen. Diese experimentelle Quantifizierung umfasst den Einfluss verschiedener Arten des Sprays (Tropfendurchmesser, Geschwindigkeit und Beaufschlagungsdichte), des Winkels des Sprayaufpralls, der Wassertemperatur des Sprays, der thermischen Eigenschaften des gekühlten Materials und der Rauigkeit der Oberfläche. Die Ergebnisse zeigen, dass die Beaufschlagungsdichte die maßgebende Einflussgröße für eine hohe Kühlleistung ist. Weiterhin zeigen die visuellen Beobachtungen keinen geschlossenen Wasserfilm, der durch einen Dampffilm von der Oberfläche getrennt ist. Somit ergibt sich in den meisten Anwendungen kein Risiko, durch eine zu große Beaufschlagungsdichte die Oberfläche zu überschwemmen und damit den Wärmestrom zu limitieren.

Die Kühlung einer schrägen Oberfläche sowie das Kühlen mit heißem Wasser reduziert die Kühlleistung, während Oberflächenrauigkeit und Verwendung eines Substrats mit hoher Wärmeleitfähigkeit die Wärmestromdichte erhöhen.

Weiterhin wurden während dieser Arbeit theoretische Modelle zur Vorhersage der Wärmestromdichte entwickelt und mit den experimentellen Ergebnissen validiert. Ein Modell für das „film boiling regime“ berücksichtigt den Einfluss verschiedener Sprays und Substrateigenschaften. Es beschreibt die zeitliche Entwicklung der Wärmestromdichte und Oberflächentemperatur und stimmt sehr gut mit den experimentellen Ergebnissen überein.

Weiterhin zeigt eine Theorie für das „nucleate boiling regime“, dass die Wärmestromdichte durch die thermische Trägheit des Substrats limitiert wird und nahezu unabhängig von den Sprayeigenschaften ist.

Der Leidenfrostpunkt ist ebenfalls unabhängig von den Sprayeigenschaften. Stattdessen wird er stark vom Material des Substrats und Fluids beeinflusst: Ein großer Wärmeeindringkoeffizient erzeugt eine geringe Leidenfrosttemperatur und umgekehrt. Dieser Einfluss wird durch die entwickelte Theorie gut vorhergesagt.

Danksagung

Zuallererst möchte ich mich bei *Prof. Dr.-Ing. Cameron Tropea* für die Anstellung am Fachgebiet „Strömungslehre und Aerodynamik“ und die Möglichkeit diese Dissertation anzufertigen bedanken. Ich konnte mich jederzeit auf seine Zusagen und einen strukturellen Rahmen verlassen, der wenige bis keine Einschränkungen bedeutete. Weiterhin geht mein ganz besonderer Dank an *Apl. Prof. Dr. Iliia V. Roisman*, der mir beim Verständnis der physikalischen Vorgänge während der Sprühkühlung und deren Modellierung essenziell geholfen hat. Die freudvollen Diskussionen endeten häufig mit neuen Erkenntnissen und manchmal nur mit noch mehr Fragen. Bei *Prof. Dr.-Ing. Eckehard Specht* möchte ich mich vielmals für die Übernahme des Korreferats dieser Arbeit bedanken.

Weiterhin möchte ich mich bei der *Deutschen Forschungsgemeinschaft (DFG)* bedanken, die diese Forschung im Rahmen des Sonderforschungsbereichs SFB-TRR 75 erst finanziell möglich gemacht hat. Ohne die tat- und sachkräftige Förderung durch den *Industrieverband Massivumformung e.V.* wäre dies ebenfalls nicht möglich gewesen. Vielen Dank hierfür und die vielen Projekttreffen der Patengruppe, die immer wieder aufs Neue den Bezug zur industriellen Anwendung sichergestellt haben.

Ich danke weiterhin den Studenten *Julian Hofmann*, *Till Kaupe*, *Minh Khang Pham* und *Sebastian Wolter*, die durch ihre Mühe und ihren Ehrgeiz diese Arbeit wesentlich unterstützt haben. Ein ganz besonderer Dank geht an die Griesheimer Jungs, die durch zahlreiche Diskussionen, gemeinsame Kochaktionen zur Mittagspause, allerlei Unfug während und nach der Arbeit und ein ganz besonderes Arbeitsklima das Arbeiten in der Exklave lebenswert, äußerst produktiv und sozial verträglich gemacht haben. Dazu zählen: *Andreas Bauer*, *Alexander Beck*, *Jan Breitenbach*, *Sebastian Brulin*, *Johannes Feldmann*, *Julian Hofmann*, *Till Kaupe*, *Johannes Kissing*, *Maximilian Kuhn-henn*, *Max Luh*, *Klaus Schiffmann*, *Benedikt Schmidt*, *Bernhard Simon* und *Martin Stenger*. Danke für die immer wiederkehrende gegenseitige Motivation!

Weiterhin danke ich dem Werkstatt-Team in Griesheim um *Timm Geelhaar*, *Joachim Heyl*, *Ilona Kaufhold* und *Martin Weiß* für die Unterstützung beim Bau der Versuchsanlage.

Obwohl zuletzt genannt, geht mein allergrößter Dank an meine Familie und Freunde. Ich möchte meinen Eltern *Georg* und *Marina Tenzer* und meiner Schwester *Anne Tenzer* für die nicht endende Unterstützung und den immer währenden Rückhalt danken. Ihr habt durch eure Erziehung und Verbundenheit den Grundstein für alles gelegt. Mein größter Dank geht an *Meike*, die mich unzählige Male bestärkt hat weiterzumachen sowie sich ebenso oft bahnbrechenden Erkenntnisse über Sprühkühlung anhören durfte, was sie sicherlich immer brennend interessiert hat. Ohne dich wäre mir vieles deutlich schwerer gefallen.

Danke,

Fabian

Contents

Abstract	i
Kurzfassung	iii
Danksagung	v
1 Introduction	1
1.1 Motivation	1
1.2 Fundamentals of spray cooling	4
1.3 Objective and outline of this thesis	10
2 Experimental setup and methods	13
2.1 Overview of the setup	13
2.2 Spraying test rig	14
2.2.1 Phase Doppler technique	16
2.2.2 Patternator	17
2.2.3 Results of experimental spray characterization	18
2.3 Cooling test rig	22
2.3.1 Mechanical and thermodynamic construction	24
2.3.2 Measurement technique for heat flux and surface temperature	26
2.3.3 Observation system	29
3 Typical results of transient spray cooling	31
3.1 Measurements of the heat flux	31
3.2 Visualization of the spray impact	34
3.3 Influence of various parameters	40
3.3.1 Spray impact parameters	42
3.3.2 Spray impact angle	45
3.3.3 Initial spray water temperature	47
3.3.4 Initial substrate temperature	54

3.3.5	Wall thermal properties	55
3.3.6	Wall surface roughness	58
4	Heat transfer in film boiling regime	61
4.1	Analysis of heat transfer during spray cooling	61
4.2	Modelling of temperature and heat flux evolution	62
4.3	Model validation	66
4.4	Application of the model	71
4.5	Transitional spray cooling regime below the Leidenfrost point	74
5	Heat transfer in nucleate boiling regime	77
5.1	Modelling heat flux as a remote asymptotic solution	77
5.2	Model validation	79
5.3	Heat flux and its upper boundary	82
5.4	Application of the model	83
6	Leidenfrost point	87
6.1	Influences on the Leidenfrost point	87
6.2	Comparison with literature	91
6.3	Theoretical prediction of the Leidenfrost point	94
7	Conclusion and outlook	103
	Nomenclature	107
	Bibliography	111
	List of Figures	123
	List of Tables	127

1 Introduction

The present chapter provides a short introduction into the topic of spray cooling. The first part gives a motivation, why research and progress in the field of spray cooling is of interest for a broad community. In the subsequent section an overview of the literature indicates questions which remain open. The present chapter ends with the objectives and outline of this thesis. Parts of this chapter have already been published in Tenzer et al. (2019b) and appeared in Tenzer et al. (2020).

1.1 Motivation

Spray cooling is a process capable of achieving a very high, nearly uniform heat flux, and therefore high cooling performance. A comparison of the heat transfer coefficients of different cooling technologies is shown in Fig. 1.1. Of all shown technologies spray cooling clearly has the highest cooling performance. Therefore it is used in various industrial applications, like cooling of micro-chips and other high powered electronics or electrical parts (Mudawar, 2001; Bar-Cohen et al., 2006; Ebadian & Lin, 2011), cooling of metal products in metallurgy during quenching processes, in metalworking (Chen & Tseng, 1992), cooling of tools for hot forging (Pola et al., 2013), of solar panels (Nizetić et al., 2016; Sargunanathan et al., 2016) and in many other technological processes.

These completely different applications indicate the complex nature and versatility of the term spray cooling. A rough classification regarding the temperature range, range of spray properties and temporal evolution helps to understand the different features of each application. For example, spray cooling of high power electronics is performed at rather low surface temperatures. The mass flux as well as the sprayed surface is small. The process is stationary, therefore the surface temperature remains nearly constant. In contrast, spray cooling for quenching during steel-making exhibits a com-

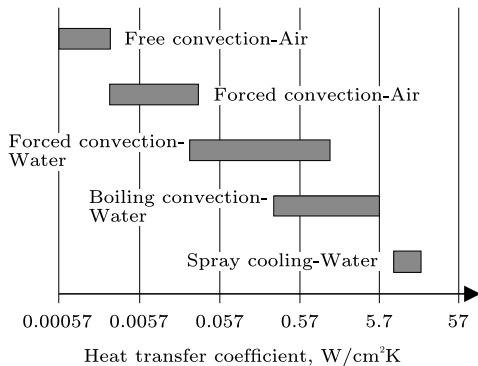


Figure 1.1: Heat transfer coefficient of different cooling technologies. (Adapted from Sienski et al. (1996), with permission of IEEE. © 1996 IEEE.)

pletely different behavior. The surface temperatures are very high. The mass flux and the sprayed surface are large. The process is transient, meaning the surface temperature continuously decreases with increasing time and therefore different hydrodynamic and thermodynamic phenomena occur over time at the surface.

The motivation for this project is focused on cooling during hot forging. Here metal blanks are heated up to 1260 °C and pressed between forging dies to reach the desired geometry. This process is used for the production of various parts that require high strength. Exemplary parts are crankshafts, gears and other parts used in industrial machinery and consumer products. Since the heated parts stay in contact with the forging dies, the temperature of the dies also rise; therefore, to prevent overheating and damage they need to be cooled. This is most often achieved by spray cooling. By shortening the necessary cooling time, the entire process time for the production of each part can be reduced. This directly leads to an increased productivity and economic efficiency. One goal of the present work is to help to overcome the bottleneck of spray cooling by achieving a better understanding of the physical processes which determine the cooling rate and by developing reliable models describing these processes, eventually leading to shortened cycle times in the cooling phase.

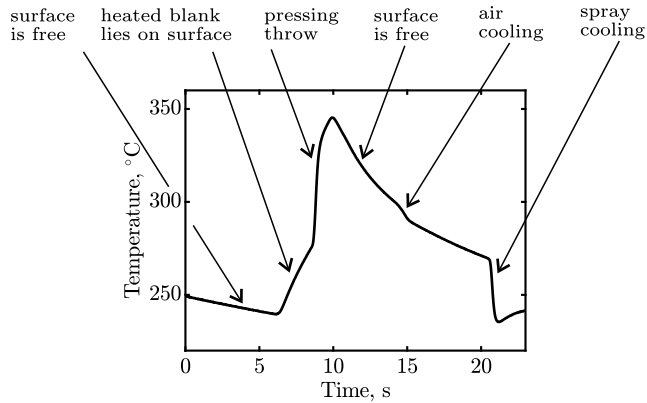


Figure 1.2: Exemplary temporal evolution of the temperature 1 mm below the surface of a workpiece during a hot forging process.

To gain a first impression of the temperatures and timescales during hot forging a preliminary experiment during a hot forging process was performed. Cylindrical steel blanks (60 mm diameter, 90 mm height) having a temperature of 1230 °C were compressed to disks (110 mm diameter, 30 mm height). The corresponding temperature inside the tool was acquired using a thermocouple, placed 1 mm below the surface.

In Fig. 1.2 the temperature reading from this experiment is plotted as a function of time. The corresponding process steps at the surface are indicated in the diagram. We can clearly identify each of the steps from the temperature response inside the target. The highest temperature of approximately 350 °C is reached at the end of the pressing throw. Although the temperature reading is not exactly the surface temperature, it is representative. This preliminary example experiment leads to a general impression of the temperature range this study should cover. Therefore, the test facility developed during this study is designed to operate at surface temperatures of up to 500 °C, as will be shown in Section 2.3.

1.2 Fundamentals of spray cooling

The phenomena of spray impingement onto a very hot substrate is significantly influenced by the wall temperature since the flow generated by each drop impact is influenced by various micro-scale thermodynamic effects, governed by intensive evaporation. The hydrodynamics and heat transfer during single drop impact onto a heated wall have been extensively investigated (Chandra & Avedisian, 1991; Bernardin et al., 1997; Bertola, 2015; Staat et al., 2015). The regimes of single drop impact observed in the experiments include single phase cooling, nucleate boiling, transition regime, thermal atomization (Roisman et al., 2018) and film boiling, the latter case occurring if the wall temperature rises above the Leidenfrost condition.

For the investigation of heat transfer during spray cooling it is often reasonable to plot the heat flux as a function of the surface temperature, as illustrated in Fig. 1.3. By representing the data in this way, the typical boiling regimes, which are known from pool boiling experiments (Nukiyama, 1966), become apparent: At high surface temperatures in the film boiling regime the heat flux decreases slightly with decreasing surface temperature. At a certain surface temperature the heat flux reaches its minimum. This point is called the Leidenfrost point. Accordingly, the equivalent surface temperature is called Leidenfrost temperature. At surface temperatures above the Leidenfrost point, a droplet that is placed on the surface has no contact to the surface, but is separated from it by a vapor layer (Leidenfrost, 1966). At temperatures below the Leidenfrost point the heat flux strongly increases with decreasing surface temperature. This regime is called the transition boiling regime. It ends at the critical heat flux which is the maximum of the curve. In the following nucleate boiling regime the heat flux again continuously decreases with decreasing surface temperature.

A detailed review of the current state of the art concerning the prediction of heat transfer during spray cooling is dispensed with here since there are many comprehensive reviews available in the literature: Liang & Mudawar (2017b,c); Cheng et al. (2016); Kim (2007); Breitenbach et al. (2018b). Many studies deal with the influence of various parameters on the performance of spray cooling. These studies are mostly focused on the determination of the critical (maximum) heat flux and on obtaining the boiling curves which describe the dependence of the heat flux on the substrate temperature. An

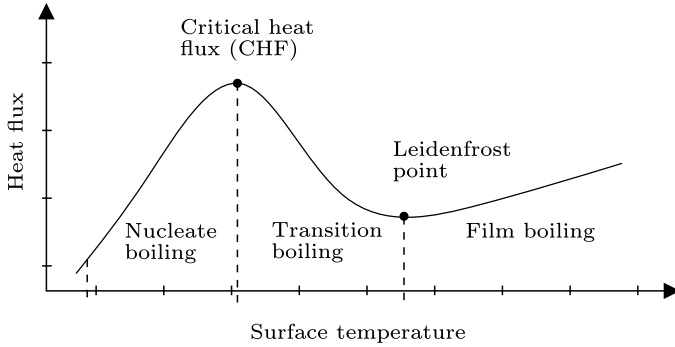


Figure 1.3: Exemplary evolution of the heat flux as a function of the surface temperature during spray cooling.

example for empirical correlations can be found in Mudawar & Deiters (1994). Among the governing parameters are spray properties, like droplet velocity, droplet diameter, mass flux, or liquid properties (Puschmann & Specht, 2004; Wendelstorf et al., 2008; Yang et al., 1996; Chen et al., 2002; Estes & Mudawar, 1995). Moreover, experiments of Cebo-Rudnicka et al. (2016) with different target materials demonstrated that the heat transfer is influenced also by the thermal conductivity of the surface.

Most of the models for the heat flux and for the critical heat flux are completely empirical. The main goal of the present study is to develop a predictive theoretical model for fast transient cooling of a very hot thick substrate by spray impact. The model should be based on the identification of the main influencing physical parameters. These influencing parameters are different for the film boiling regime and for the nucleate boiling regime.

The following subsections address some selected issues and influencing parameters during spray cooling which are covered to a lesser extent in the review literature cited above.

The Leidenfrost point The following section gives an overview of the state of the art regarding the understanding of the Leidenfrost point and its influencing parameters.

The physics of the transition from the nucleate boiling regime to the film boiling regime at the Leidenfrost point is not yet completely known in that the Leidenfrost temperature cannot be reliably predicted. Several theoretical models have been developed based on the hydrodynamic stability analysis of the vapor/liquid interface Jerome (1960); Zuber (1958); Kakac & Bon (2008) or thermocapillary stability Aursand et al. (2018). Some authors assume that the Leidenfrost temperature is determined by the foam limit Spiegler et al. (1963); Wang et al. (2019b), which is the maximum temperature to which a liquid can be superheated, or by the limiting minimum vapor thickness Cai et al. (2020) when it becomes comparable with the surface roughness. However, the influence of the surface roughness is not yet clearly delineated and requires further investigations.

During single drop impacts: Numerous studies deal with the Leidenfrost point during single drop impact (Quéré, 2013; Biance et al., 2003; Castanet et al., 2015; Tran et al., 2012), showing a difference between the static Leidenfrost temperature T_{Ls} of a sessile droplet and the dynamic Leidenfrost temperature T_{Ld} of an impacting droplet. In these studies the dynamic Leidenfrost point is often observed as the transition between a wet and dry rebound. A review on the static Leidenfrost temperature can be found in Bernardin & Mudawar (1999).

Although, there is an ongoing discussion about the influencing parameters on this point (Liang & Mudawar, 2017a), there exists some agreement that the dynamic Leidenfrost point depends on the Weber number. Therefore, common correlations for the dynamic Leidenfrost temperature in the form of

$$T_{Ld} = T_{Ls} + C_1 We^{C_2} \quad (1.1)$$

can be found (Bertola, 2015; Yao & Cai, 1988). Here the dynamic Leidenfrost temperature is linked to the static one by an influence of the Weber number. Although Eq. (1.1) is used in many studies, the values found for the empirical constants C_1 and C_2 span a large range, depending on which study is quoted. The studies have in common that $C_2 < 0.5$. This leads to a somewhat diffuse picture of the physics involved in the Leidenfrost point. Nevertheless, since $C_2 < 0.5$, Eq. (1.1) indicates that for a sufficiently large Weber number the

second term in Eq. (1.1) will converge to a constant. Therefore the influence of the Weber number becomes small and the Leidenfrost temperature is nearly constant for sufficiently large Weber numbers.

Wang et al. (2019b) performed experiments with various substrate materials for single drop impacts having a Weber number in the range $We = 30 - 120$. The results indicate no influence of the Weber number. Instead different substrate materials lead to different Leidenfrost temperatures. The authors conclude that a higher thermal effusivity leads to a higher Leidenfrost temperature. They further compared their experimental data to a Leidenfrost point model proposed by Bjornard & Griffith (1977) which is based on the homogeneous nucleation theory. They find a good agreement between their experimental data and the theory.

In sprays: The studies of Sozbir et al. (2010) and Sozbir et al. (2003) indicate an higher Leidenfrost temperature for higher mass fluxes. Furthermore, their study shows an increasing Leidenfrost temperature for increased air velocity of a pneumatic atomizer. The same influence of the mass flux is reported in Hoogendoorn & den Hond (1974). Here the range of Leidenfrost temperatures is 350 to 900 °C. The authors also conclude that outcomes concerning the Leidenfrost point of single droplets cannot be transferred to the Leidenfrost point in sprays. The same influence of rising Leidenfrost temperature with rising mass flux is confirmed by Gottfried et al. (1966); Al-Ahmadi & Yao (2008). Al-Ahmadi & Yao (2008) report a insignificant influence of the droplet diameter and velocity. They correlated their data for $\dot{m} = 1.5 - 30 \text{ kg/m}^2\text{s}$ with the expression

$$T_L = 536.8 \dot{m}^{0.116}. \quad (1.2)$$

Here T_L is the Leidenfrost temperature and \dot{m} the mass flux. Additionally, the authors show that the Leidenfrost temperature depends on the substrate material. Their experiments performed with stainless steel have much higher Leidenfrost temperature than those with copper or aluminum.

Based on a dimensional analysis Yao & Cox (2002) derived a modified Reynolds and Weber number using spray relevant parameters to represent the inertia of the entire spray instead of that of a single droplet. These spray

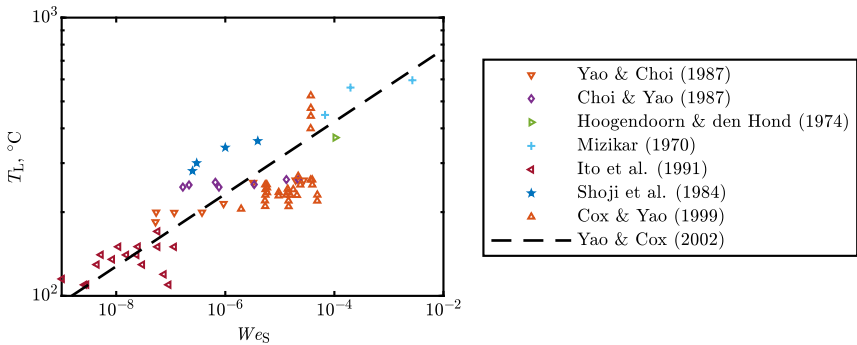


Figure 1.4: Dependence of the Leidenfrost temperature on the spray Weber number and application of correlation Eq. (1.5). (Adapted from Yao & Cox (2002), with permission of Taylor & Francis. © 2002 Taylor & Francis.)

Reynolds and spray Weber numbers are defined as

$$Re_S = \frac{\dot{m}D}{\eta} \text{ and} \quad (1.3)$$

$$We_S = \frac{\dot{m}^2 D}{\rho\sigma}, \quad (1.4)$$

where D , η , ρ and σ are a mean diameter, dynamic viscosity, density and surface tension. The authors identify a positive correlation between spray Weber number We_S and Leidenfrost temperature. The same effect is reported by Labergue et al. (2015). Yao & Cox (2002) used their own experimental data in combination with results from various other studies and derived the following correlation:

$$T_L = 1400 We_S^{0.13} \quad (1.5)$$

The correlation as well as the underlying data is shown in Fig. 1.4.

Bernardin & Mudawar (2004) developed a model for the Leidenfrost temperature of impacting droplets and sprays which accounts for the droplet velocity U ,

$$T_L = 162 + 24.3U^{0.64}. \quad (1.6)$$

The model is applied to experimental data of Klinzing et al. (1992) and Bernardin & Mudawar (1996) and indicates only an influence of the droplet velocity.

In summary, the literature dealing with the Leidenfrost point for sprays is rather sparse. For single drop impacts there is some agreement on an influence of the Weber number on the Leidenfrost temperature. Although, there is some agreement that the Leidenfrost point during spray impact mainly depends on the mass flux, the overall picture is not clear. Concerning the Leidenfrost point in sprays, there currently exist no physical models or explanations, but only a few empirical correlations, which themselves exhibit large scatter.

Influence of the initial spray water temperature Spray cooling involves single drop impact. Depending on the regime and the number flux of spray droplets, the heat flux can even be described by a superposition of single drop impacts (Breitenbach et al., 2017b). Therefore it is worth starting the review of the existing literature with studies dealing with single drops.

In Hiroyasu et al. (1974) the influence of the initial drop temperature on the drop lifetime of a benzene drop is investigated for different surface temperatures. The lifetime becomes smaller at all surface temperatures for the warmer drop.

The findings in Bernardin & Mudawar (1999) indicate no effect of the liquid subcooling on the Leidenfrost temperature of a sessile drop. This is explained by the very fast heating to saturation temperature of the small amount of liquid contained in the drop. This outcome is in accordance with other studies.

In Xu & Gadala (2006) the influence of the water temperature during jet cooling is investigated. Hot water results in a lower heat flux at all surface temperatures and also in a lower Leidenfrost temperature. The film boiling regime is only present in the case of low water temperatures. The authors conclude that the film boiling regime only exists for high water temperatures.

The outcomes of Nimi et al. (2012) show a strong shift of the Leidenfrost point during spray cooling towards lower temperatures for higher initial water temperatures.

We can summarize: First, the fluid temperature strongly influences the heat flux during spray and jet cooling. Second, it has an impact on the Leidenfrost point for spray and jet cooling. Third, there is no influence on the Leidenfrost point of a single drop.

1.3 Objective and outline of this thesis

Spray cooling is used in many different industrial applications because of its high cooling capability. In recent years various applications of spray cooling demand an even higher and more predictive cooling performance. For example: In the forging industry, a higher cooling performance leads to a shorter cooling time, shorter cycle times and therefore higher productivity. High power electronics could be more powerful when equipped with better cooling devices. These trends require a deeper understanding of the physics of spray cooling and reliable models to design and predict the cooling process. To date, the overall physical picture is not complete and existing predictive tools are highly empirical and not universal.

The goal of the present thesis is to improve the knowledge of spray cooling and develop models predicting the heat flux. For this purpose measurements of heat transfer and its dependence on various parameters like spray or wall properties are performed. The results are linked with visualizations of the hydrodynamics during spray impact. This leads to a new understanding of certain regimes of spray cooling and to new predictive models.

Chapter 2 describes the experimental setup and measurement techniques used for the experimental investigations.

Chapter 3 starts with an illustration of the typical outcomes of transient spray cooling. First the heat flux and surface temperature are investigated and connected to observations of the spray impact. This is followed by remarks about the influence of various parameters, like spray impact or wall parameters.

In **Chapter 4** the heat transfer in the film boiling regime is analyzed. A predictive model for the heat transfer, which accounts for various spray and wall properties, is developed and validated.

In **Chapter 5** a predictive model for the heat transfer in the nucleate boiling regime is developed. The model acts as an upper boundary of the heat flux and is validated against various influencing parameters.

Chapter 6 deals with the Leidenfrost point and its influencing parameters. The experimental data is analyzed and compared to existing data from literature. The main influence is characterized and correlated to predict what conditions determine the Leidenfrost point.

Chapter 7 concludes this thesis and offers an outlook for topics to be addressed in future studies.

2 Experimental setup and methods

This chapter describes the different experimental setups and measurement techniques used for the acquisition of the experimental data in this study, with some exemplary results shown for illustration.

Parts of this chapter have already been published in Tenzer et al. (2018, 2019a,b). In addition Wolter (2018) supported the construction of the experimental setup and performed first measurements.

2.1 Overview of the setup

In this study two different setups are used, as shown in Fig. 2.1. The test rig on the left side is used for performing the cooling experiments and is therefore called the *cooling setup*. It consists of the heated target equipped with thermocouples connected to a data acquisition system. This forms the measurement system for the acquisition of the surface temperature and the heat flux at the surface where the spray impact takes place. A high speed camera equipped with a long distance microscope or other lens in combination with a back light illumination is used for visual observation of the hydrodynamics during spray impact. The spray is produced by conventional atomizers driven by a water supply system.

The test rig on the right side is called *spraying setup* and features all instrumentation for a precise characterization of the spray. The atomizer and water supply system is exactly the same as in the previously described cooling setup. A phase Doppler (PD) measurement system consisting of a PD receiver, PD transmitter and data acquisition is used to measure the droplet diameters and velocities. A custom built patternator measures the local mass flux.

During post processing, data from both test rigs are combined to correlate the local heat transfer, accompanied by the visual observation of the hydrodynamics during spray impact, with the local spray properties. By changing

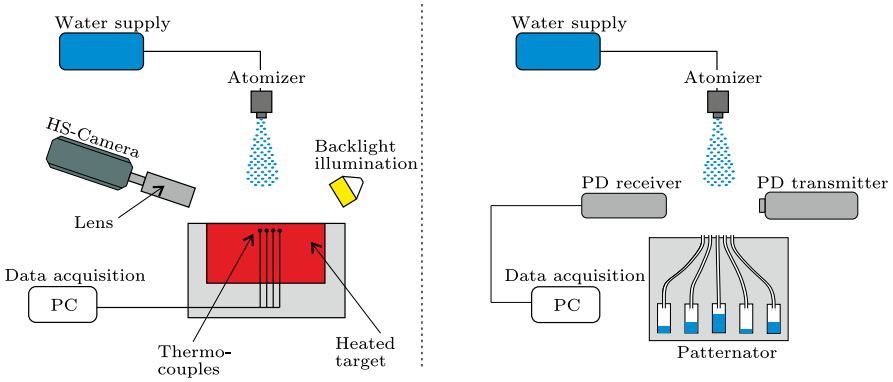


Figure 2.1: Schematic of experimental setup. Left: Heat flux measurements with thermocouples and visualization with HS-camera. Right: Spray characterization with phase Doppler measurement system and patterator. (Adapted from Tenzer et al. (2019b), with permission of Cambridge University Press. © 2019 Cambridge University Press.)

the type of atomizer, the supply pressure of the atomizer and the distance between the atomizer and the heated target, different kinds of sprays can be produced. Geometric constraints limit the distance between the atomizer and target to 50 – 350 mm. The entire setup is completely automated and controlled by a PC running *Labview*, which is also used for acquiring and recording the data.

A more detailed description of this equipment follows in the subsequent sections of this chapter.

2.2 Spraying test rig

A detailed sketch of all components involved in the process of spray generation is shown in Fig. 2.2. Purified water from a reverse osmosis device is stored in a tank (1). In cases of experiments with elevated spray water temperature, the water is heated by an immersion heater (2) connected to a temperature controller (3). In other cases the water remains at ambient temperature. A gear pump (4) is used to supply the atomizer. A pressure (5) and a temperature sensor (6) acquire the corresponding quantities of the water. The

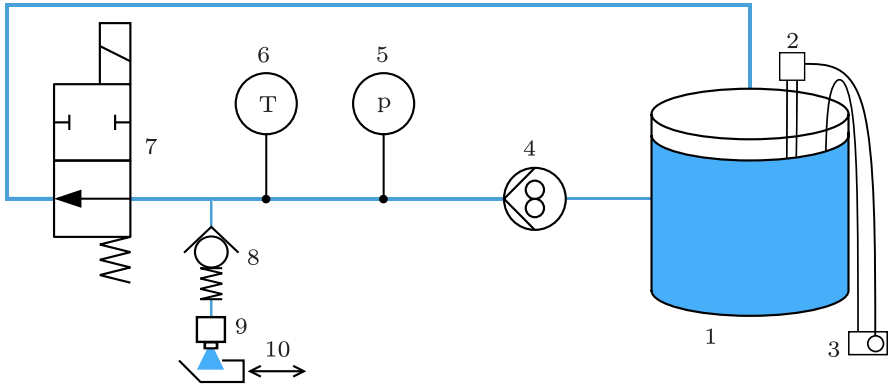


Figure 2.2: Detailed sketch of the atomizer and water supply system used for spray generation.

atomizer (9) is separated from the supply line by a check valve (8). The supply line is connected to the recirculation line through a directional valve (7). A movable shutter (10) is located directly below the orifice of the atomizer. This device is able to collect all spray that exits the atomizer. It is quickly pushed into or out of the spray stream by a pneumatic cylinder. The shutter is opened only when the spray has reached its steady state. This avoids larger fluid ligaments, which are typical for the unsteady starting phase of an atomizer, from reaching the heated surface or patternator.

The setup allows the water to circulate through the entire system when the directional valve is in open position. The check valve remains closed since the pressure upstream is lower than its opening pressure and therefore no water leaves the atomizer. During this circulation phase the circulating water heats all components of the system to the desired water temperature to ensure a constant spray water temperature during spraying. When the directional valve is closed the pressure upstream of the check valve rises until finally the check valve opens and the water leaves the atomizer as a spray. The check valve creates a pressure loss of 0.2 bar which is registered during operation. However, since the same spraying system is used for all experiments the pressure drop does not have to be considered further. The desired atomizer operation pressure is kept constant using a controller, which controls the speed of the gear pump based on the pressure sensor data.

Table 2.1: Overview of atomizers used for the experiments and their operational parameters.

Atomizer	Bore diameter, mm	Spray angle	Operation pressure, bar	Mass flow rate, kg/h
Lechler 490.403	1.25	45°	1.5 – 10	51 – 135
Lechler 490.603	2	45°	2 – 5	186 – 266
Spraying Systems 3002.5	0.79	30°	1.5 – 10	46 – 102
Spraying Systems 3001.4	0.79	30°	2 – 10	28 – 64

The atomizers are mainly one component, pressure swirl, full-cone type, which are available from various companies. For this work four different atomizers are chosen, with the aim of obtaining a broad span of spray parameters. The designation and typical operational parameters of the four atomizers are summarized in Table 2.1. The bore diameter and spray angle are taken from the manufacturer’s data sheet. The operation pressure and the mass flow rates were acquired during the phase Doppler measurements. For this purpose a Coriolis mass flow meter (*Optimass 7400 C* from *Krohne*) was installed upstream of the atomizer. Due to the limited capacity of the gear pump, the pressure range for the largest atomizer is limited.

Preliminary experiments were performed using a pneumatic atomizer, which uses a secondary air stream to enhance the atomization process. The designation of that atomizer is *Lechler 136.115*. Generally a pneumatic atomizer produces a spray having smaller and faster droplets and a lower mass flux. Since only a few experiments were performed with this atomizer, a detailed description of its spray properties have been omitted below.

2.2.1 Phase Doppler technique

The local drop diameter and two-component drop velocity vector is acquired using a phase Doppler measurement system operated in the dual-mode configuration. The system is built by *DantecDynamics* and consists of a transmitting and a receiving optic and a processing unit. A detailed description of this measurement system is given in Albrecht et al. (2013); Tropea (2011); Tropea

Table 2.2: Parameters of the phase Doppler measurement system.

Parameter	Setting
Laser type	DPSS laser
Laser power	18 – 300 mW
Wavelength 1	532 nm
Wavelength 2	561 nm
Beam spacing	60 mm
Transmitter focal length	500 mm
Receiving system	112 mm Dual PDA
Receiver focal length	500 mm
Scattering angle	28°
Refractive index water	1.33

et al. (1996). The relevant system parameters are summarized in Table 2.2. Laser power and other operational parameters were adjusted according to Araneo & Tropea (2000) to ensure the best measurement results and validation rates. The interchangeable receiving aperture mask was selected depending on the droplet size range of each atomizer and operating pressure. More details about the setup and experimental procedure can be found in Wolter (2018).

2.2.2 Patternator

A measurement device for the acquisition of the local mass flux is called a patternator (Lefebvre, 1988). During this work two different custom made mechanical patternators were used. Both devices use tubes to collect the amount of spray water m that hits a part of an surface area A in a given time t . Since the collection area A is small compared to the overall sprayed surface, the mass flux \dot{m} used in this work is a local quantity. It can be calculated by

$$\dot{m} = \frac{m}{At}. \quad (2.1)$$

The difference of the two patternators employed in this study lies in the method with which the amount of collected water was measured. The first device measures the mass of the collected liquid by weighing. The water is gathered by 17 small tubes of inner diameter of 4 mm, placed in a row with a

distance of 6 mm from one another. These tubes feed the water to containers which are then weighed. A more detailed description can be found in Wolter (2018).

Due to the necessity of weighing each container, these measurements take a long time. To overcome this drawback an automated patternator was developed. The collection surface was increased to $6 \times 6 \text{ mm}^2$ which is still small enough to capture any spray inhomogeneities. The weighing is replaced by a capacitive measurement of the fluid level in each of the cells. Details of the working principle and the construction can be found in Kaupe (2017) and Hofmann (2019). With the addition of an automated drain system the measurement time is greatly reduced.

The measurement axis of the patternator was aligned with the position at which the temperature measurements were performed, ensuring that both quantities are acquired at the same position.

2.2.3 Results of experimental spray characterization

In the following section only exemplary results are discussed in detail, simply to show the typical behavior of the spray. Since the remaining results exhibit the same trends, they are only summarized in an overview.

Exemplary results of droplet diameter and velocity Phase Doppler data is acquired without the target on horizontal planes at distances to the nozzle from 25 to 300 mm. Further decreasing the distance is not possible due to a strong decrease of the validation rate, since the breakup process is not completed and many droplets are non-spherical, prohibiting measurement using the phase Doppler technique. Above 300 mm there is no significant change of the spray properties.

Figure 2.3a shows the mean droplet diameter D_{10} at 100 mm distance from the nozzle and at certain positions along the radial axis, where 0 corresponds to the geometrical center of the nozzle. The experiments were performed using the *Lechler 490.403* atomizer. As expected, the droplet diameter reaches a minimum in the center of the nozzle and increases slightly towards the periphery. With increasing pressure the mean droplet diameter decreases, which is also expected.

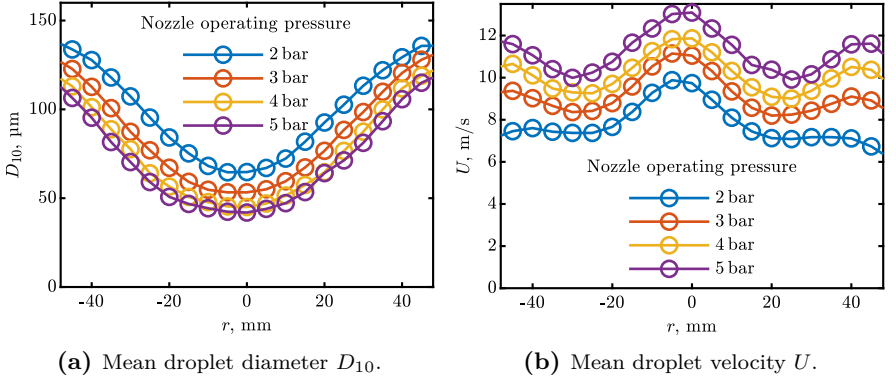


Figure 2.3: Mean droplet diameter and velocity as a function of radial position. Position $r = 0$ mm corresponds to the geometrical center below the orifice. (Adapted from Tenzer et al. (2019b), with permission of Cambridge University Press. © 2019 Cambridge University Press.)

In Fig. 2.3b the mean droplet velocity in the main flow direction U is shown at the same positions and distances as considered before. In the center the velocity attains a maximum and decreases at the outer positions. An increased pressure results in an increased droplet velocity.

Influence of the target as a displacement body. Since the phase Doppler measurements were performed in absence of the target, the question arises whether these free stream results are comparable to those in presence of the heated target. For that reason additional measurements were performed in presence of a bluff body having the same dimensions as the heated target. The measurement plane was located 10 mm above the surface of the target. During data processing we included only those droplets having a mean velocity in the downward direction, to exclude those droplets that had already impacted at the surface and rebounded. In an exemplary case the integral spray characteristics are for free stream conditions: $D_{10} = 59 \mu\text{m}$ and $U = 9.6 \text{ m/s}$. Due to the presence of the bluff body the values changed to: $D_{10} = 81 \mu\text{m}$ and $U = 9.7 \text{ m/s}$. Especially the small droplets are affected by the displacement of the target, resulting in the higher D_{10} , since only a smaller portion of them reach the surface. However, because the largest influence on the heat flux

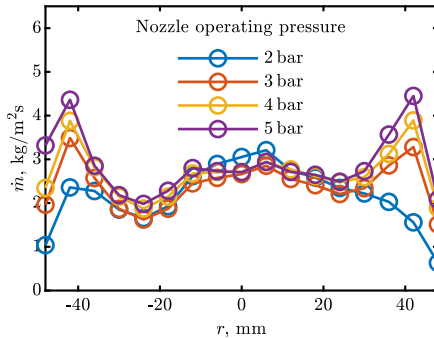


Figure 2.4: Mass flux as a function of the radial position. Position $r = 0$ mm corresponds to the geometrical center below the orifice. (Adapted from Tenzer et al. (2019b), with permission of Cambridge University Press. © 2019 Cambridge University Press.)

is the mass flux and the previously mentioned differences are rather small, we conclude that it is reasonable to use the droplet diameter and velocity acquired under free stream conditions as input data for the present work. Details of the experiments and results regarding the influence of the target can be found in Wolter (2018). Perhaps even more significant is however the fact that the measurement of the mass flux using the patternator does mimic exactly the conditions prevailing with the heated target.

Exemplary results of mass flux In Fig. 2.4 the mass flux at different radial positions is shown for different operating pressures of the atomizer at 100 mm distance to the nozzle. The measurements are performed with the patternator. The plot for 2 bar demonstrates the expected trend of a full-cone atomizer: the highest mass flux appears in the center with a strong decrease towards the outside. This behaviour changes with increasing pressure. Normally one would expect the shape to remain nearly constant with a shift towards higher mass fluxes. From the measurements we see instead a decrease of the mass flux in the center and an increase at the outer region. The entire spray pattern changes with rising pressure and the atomizer appears to behave more like a hollow cone atomizer. This means that the main spray is concentrated in a ring of the radius 40 to 50 mm. This behaviour is typical of a pressure swirl atomizer.

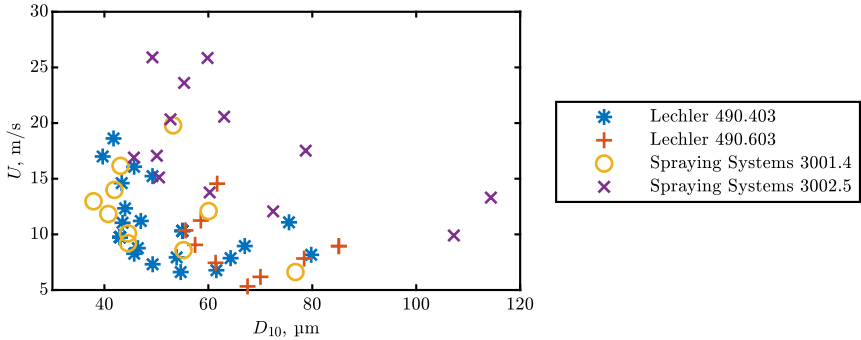


Figure 2.5: Droplet velocity versus diameter for various atomizer in the center region below the atomizer. Operation pressure and distance also varied but not indicated in the figure.

It is interesting that the mass flux at the center depends only weakly on the injection pressure. For the nozzles used in the experiments the pressure influences mainly the mass flux distribution in the outer ring of the spray cross-section.

Overview of the spray parameter range By changing the type of atomizer, operating pressure and distance between the atomizer and target, different kinds of sprays can be produced. The resulting parameter range, which can be achieved by the previously mentioned operation conditions, is shown in Fig. 2.5. Here the mean droplet velocity is plotted versus mean droplet diameter for the central area below the atomizer. The parameters span the range $D_{10} = 38 - 114 \mu\text{m}$ and $U = 5 - 26 \text{ m/s}$. Within these boundaries the parameters scatter highly.

The local mass flux spans the range $\dot{m} = 0.5 - 29.5 \text{ kg/m}^2\text{s}$. An isolated trend for the dependence of the local mass flux on operation conditions cannot be identified, as shown in Fig. 2.4. Nevertheless, decreasing the distance between the atomizer and target obviously increases the mass flux.

Since the outcomes of isothermal drop wall interaction are governed by the droplet velocity and diameter, it is reasonable to introduce the dimensionless parameters, Reynolds and Weber number, as follows:

$$Re = \frac{UD_{10}}{\nu_f} \quad (2.2)$$

$$We = \frac{\rho_f D_{10} U^2}{\sigma_f} \quad (2.3)$$

Here ν_f is the kinematic viscosity, ρ_f the density and σ_f the surface tension of the liquid. The range of parameters used for this experimental study can also be described as $Re = 403 - 1732$ and $We = 26 - 549$.

For the sake of completeness, it is mentioned that the spray parameters of the pneumatic atomizer span the ranges: $\dot{m} = 0.2 - 3.3 \text{ kg/m}^2\text{s}$, $D_{10} = 12 - 24 \text{ }\mu\text{m}$ and $U = 12.7 - 23.4 \text{ m/s}$ or $Re = 200 - 434$ and $We = 32 - 125$.

These ranges of spray parameters are also used for the cooling experiments.

2.3 Cooling test rig

In Fig. 2.6 the heated target and its peripheral equipment are shown as it is used during the cooling experiments. The target (inner surface) is installed in a watertight housing which also contains insulation material. An outer hollow cylinder surrounds the housing and is connected at the bottom to a ventilation system (not shown here). Thus, the slit between outer cylinder and housing acts as a suction channel which extracts the overspray and secondary droplets. The extraction system is necessary to ensure optical access to the heated surface and to protect the surrounding equipment from contamination with water.

The heated target The heated surface of the spray impact target is the top end of a circular cylinder (diameter $d_T = 100 \text{ mm}$ and height $h_T = 53.2 \text{ mm}$). A detailed drawing is found in Fig. 2.8. During the course of this study different targets having the same geometry were used. They were built from various materials and have different surface conditions. Table 2.3 summarizes the different targets and their material properties. Here ρ , c_p and λ are the density, specific heat capacity and thermal conductivity respectively. Each



Figure 2.6: Heated target equipped with watertight housing and ventilation slit.

Table 2.3: Overview of targets and material parameters used of cooling experiments.

Name	Material	Surface condition	ρ , kg/m ³	c_p , J/kgK	λ , W/mK
Stainless steel	1.4841	smooth	7900	542	16
Stainless steel	1.4841	rough	7900	542	16
Hot-work tool steel	1.2365	smooth	7800	510	33
Nickel	2.4068	smooth	8900	500	63

value corresponds to the calculated mean between 100 and 500 °C. The smooth surface condition corresponds to a mirror polished surface made by lapping and polishing. The average roughness of these surfaces is $< 0.03 \mu\text{m}$. The rough surface was produced by sandblasting, resulting in an average roughness of $\approx 10 \mu\text{m}$.

Both stainless steel and nickel exhibit good resistance against corrosion and oxidation. The majority of experiments were performed with stainless steel. This target endured more than 300 cooling experiments. Since the surface suffered from thermo-shock, changes of the surface, like less brightness, are visible. Despite this, the repeatability between the first and last experiments is good.

In contrast, the target built of hot-work tool steel exhibits much more corrosion. Therefore only a few exemplary experiments were performed to fill the gap of thermal properties between stainless steel and nickel.

2.3.1 Mechanical and thermodynamic construction

The main challenges during the construction of the heated target are achieving good thermal insulation and maintaining a watertight housing to ensure that a complete flooding of the target is possible without any damage to components. These difficulties arise from the following two problems:

- Typically insulation materials are porous and therefore not suitable for contact with water.
- The dimensions of the heated target enlarge approximately 1 mm between ambient temperature and operation temperature due to thermal expansion. Any typical sealing material having the flexibility to compensate this enlargement does not withstand the high temperatures of about 500 °C. On the other hand, a rigid connection between the parts would break due to the force of the thermal expansion.

The above mentioned difficulties lead to a rather complicated construction, as shown in Fig. 2.7:

A split copper disk (2) is screwed to the bottom of the target (1) by using four threaded rods (4). For protection of the soft copper, a pressing plate (5) built of stainless steel (1.4841) is used to equally distribute the connection force. Four cartridge heaters (3) (500 W each) are installed inside the split copper disk.

The top cover of the housing is a rigid plate (6). It is built of fiber cement *Kelutherm 700* and has a low thermal conductivity of 0.38 W/mK. This plate is covered by a 0.3 mm thin stainless steel sheet (7), to protect the fiber cement from water. At the outside the fiber cement plate and stainless steel sheet are screwed to the outer cylinder (8) which is built of aluminum. An aluminum ring (9) is installed to equally distribute the pressure of the screws. Since there the temperature is low, conventional silicone sealing plates are used to watertight the interfaces between the different components.

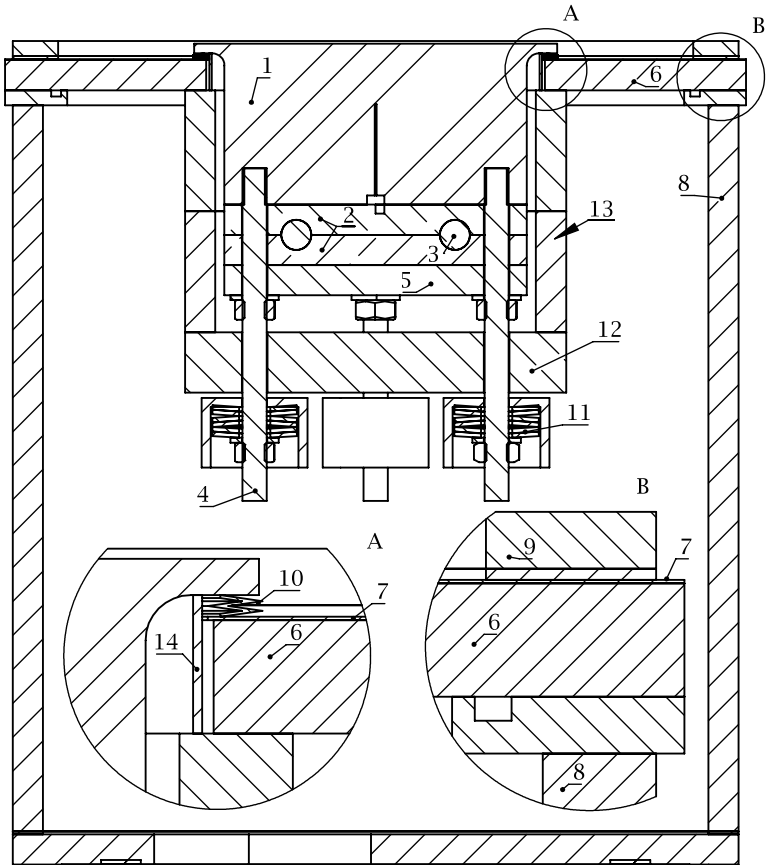


Figure 2.7: Heated target and additional components inside the watertight housing.

The target (1) rests with its collar on the top cover. A metallic seal (10) is installed between the target collar and stainless steel cover to watertight this interface. The seal is a metallic high temperature duct seal type “E-Ring”. It has the benefit of not requiring high sealing forces. These seals are usually custom built parts, except some stock models used in the aviation industry. For simplicity this setup is built using such a stock seal (*AS1895/7-450*), which can be purchased from aviation aftermarket suppliers.

High temperature disk springs (11) built by *Vinsco Spring Limited* are installed at the bottom of the heated target to ensure a nearly constant sealing force, independent of the thermal expansion. These disk springs act between the threaded rods (4) and a compression structure. The structure consists of a plate (12) built of *Kelutherm 800 M* and two hollow cylinders (13) built of *Kelutherm 700*. A spacer (14) limits the compression of the seal to its range of operation. Due to this construction, the insulation material is only subjected to pressure, and the heated parts can freely expand and contract.

The free space inside the cylinder (8) is filled with *Insulfrax S* insulating blanket for insulation propose. Additionally, the inside is filled with Argon gas to protect all materials and especially the copper disk from oxidation. Due to the seals, the housing is nearly gas tight and the pressure inside can be raised to ≈ 0.2 bar above atmosphere. Therefore, failure of any seal or part can be detected by an increased volume flow of the Argon gas. Thus, any damage of the watertight housing is detected before water enters the inside and leads to further destruction.

A temperature controller based on *Labview* is implemented in the measuring PC and controls the desired temperature inside the copper disk by taking temperature readings from a thermocouple inside the copper disk as an input value and by adjusting the heating power.

2.3.2 Measurement technique for heat flux and surface temperature

The aim of this work is to achieve a better understanding of transient spray cooling. Since transient cooling requires a thick target as thermal mass which can be continuously cooled, the possible measurement techniques for heat flux are rather limited. For example, infrared imaging from the bottom is not

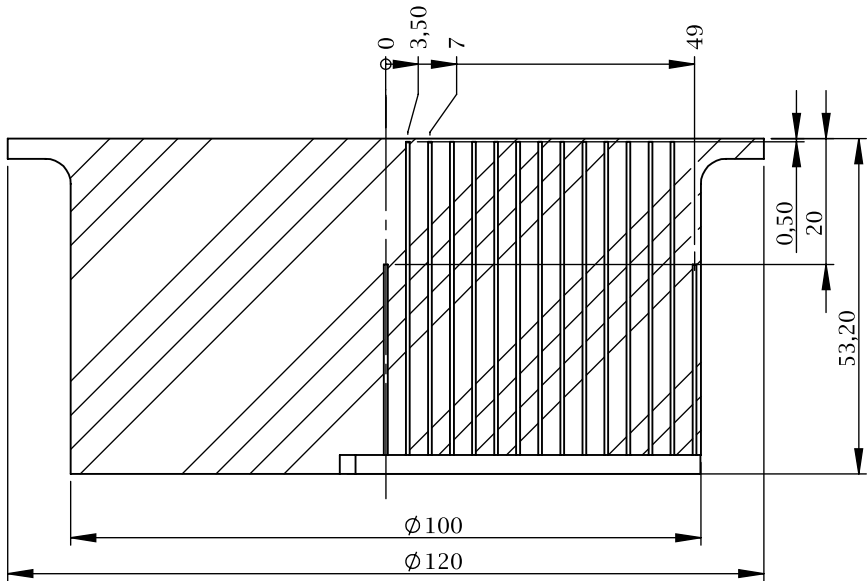


Figure 2.8: Sketch of the sectional view of the heated target showing the thermocouple positions. Dimensions are in mm.

possible due to the presence of the non-transparent target. Infrared imaging from the top suffers from poor optical accessibility caused by the dense spray and an undefined emission coefficient due to changing surface conditions.

The measurement technique used in this work is therefore based on solving the inverse heat conduction problem (IHCP) using temperature readings from inside of the target as input data. By solving the IHCP the boundary conditions can be calculated from data taken inside of the domain. In our case the boundary condition corresponds to the unknown heat flux and the data from inside of the domain to temperature readings from the inside of the target. The temperature is acquired by thermocouples embedded inside the target. In Fig. 2.8 the position of the thermocouples inside the target is shown. They are placed in two rows. The first is located 0.5 mm below the surface to achieve a quick response time. The second is 20 mm below the surface to make the IHCP independent of the boundary condition at the bottom. The radial distance between each sensor in the first row is 3.5 mm to account

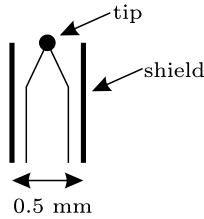


Figure 2.9: Sketch of the thermocouples having an open measuring tip which is aligned with the shield.

for any radial distribution of the heat flux. The problem is assumed to be two-dimensional, axisymmetric and having adiabatic boundary conditions at the curved surface area.

The IHCP is solved using a procedure published by Monde et al. (2003). Furthermore, Monde and coworkers at Saga University developed and made available an inverse heat conduction analysis tool “Invers2D”. In the present work, this tool is used for calculating the heat flux and surface temperature from temperature readings of the thermocouples.

The procedure is described in detail in Woodfield et al. (2006). It solves the problem in Laplace space. Therefore the two-dimensional heat conduction equation is transformed into Laplace space. The measured temperature inside the target is approximated in time as a series of half-power polynomials and in space direction as Fourier-Bessel series. After solving the problem in Laplace space, an inverse Laplace transform leads to the solution.

The thermocouples are type K, class 1, with 0.5 mm shield diameter. The measuring tip is open and aligned with the shield, as shown in Fig. 2.9. This results in a fast rise time.

The holes, inside which the thermocouples are placed, are produced using the spark erosion technique. The resulting hole diameter is 0.6 mm. The sensors are bonded inside the holes using a thermally high conductive adhesive (*Aremco Ceramabond 569 VFG*) to ensure good thermal contact.

The temperatures are sampled at a sample rate of 95 Hz using *National Instruments NI 9212* thermocouple input modules attached to a *National Instruments cRio 9074*.

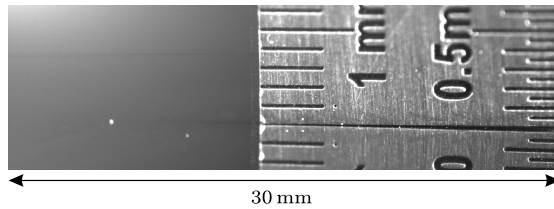


Figure 2.10: Field of view for configuration with *Tamron* 180 mm macro optical lens.

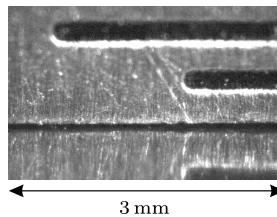


Figure 2.11: Field of view for configuration with *Questar QM-100* long distance microscope objective lens.

2.3.3 Observation system

Since there are only qualitative and no quantitative outcomes based on the visualization, a long description of the visualization system is omitted and only a brief summary of the hardware is given.

The observation system consists of a high-speed camera equipped with two different lenses and a back light illumination source. The camera is either a *Phantom v12.1* or *Phantom v2012*. Depending on the desired field of view a *Tamron* 180 mm macro optical lens (far field) or a *Questar QM-100* long distance microscope (near field) is used. An exemplary image of the surface and scale for both configurations is shown in Figs. 2.10 and 2.11. In addition to the different magnification the depth of view is much smaller in the case of the long distance microscope. This helps to mask the droplets that are outside of the focal plane and therefore prevent these droplets from obstructing the optical accessibility.

The back light illumination consists of a light source and a diffusor plate. In the case of the objective lens, a high power LED is used as light source. For the configuration with the long distance microscope an infrared *Cavilux HF laser* is necessary to achieve short illumination times to prevent motion blur while maintaining high light intensity.

The visualization and heat flux measurements are temporally matched and therefore visual observations can be directly associated with the instantaneous local heat flux and target surface temperature.

3 Typical results of transient spray cooling

This chapter describes the experimental results obtained in this study. First some general outcomes of the heat transfer during spray cooling are shown and afterwards these are connected to the visualization of the hydrodynamics involved in spray impact. The subsequent parts show the influence of various parameters on the heat transfer.

Unless otherwise stated, the underlying experiments of the following results were performed using the stainless steel target having a smooth surface.

Parts of this chapter have already been published in Tenzer et al. (2018, 2019a,b). Furthermore Pham (2018) and Hofmann (2019) supported the experimental investigation and performed some of the measurements.

3.1 Measurements of the heat flux

Contrary to many experimental studies of spray cooling in which the substrate temperature is kept constant, in the present study transient heat transfer is investigated, since this situation is relevant to many industrial applications mentioned in Section 1.1. Therefore, the target is initially heated until it achieves a given uniform initial temperature. The spray parameters are kept constant during the entire experiment. The influence of any start-up phase during the initial development of the spray is avoided by using a shutter in front of the nozzle. The heat transfer measurements are started only after the spray is fully developed, the target has been uniformly heated and the shutter has been opened. At time $t = 0$ the heating of the target is switched off, simultaneous with the opening of the spray shutter. At this instant the substrate temperature starts to change due to the heat flux associated with spray impact.

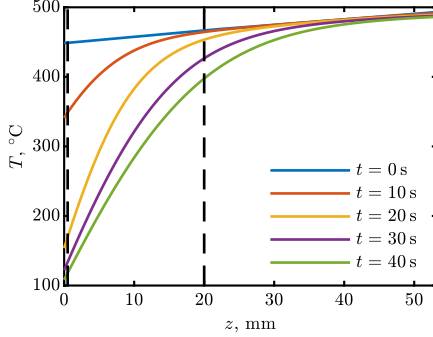


Figure 3.1: Calculated temperature T inside the substrate as a function of the depth z for different times t . The dashed lines indicate the position of the thermocouples at $z_1 = 0.5$ mm and $z_2 = 20$ mm. (Adapted from Tenzer et al. (2019b), with permission of Cambridge University Press. © 2019 Cambridge University Press.)

The typical evolution of the temperature field inside the substrate, the surface temperature and the heat flux are illustrated in Figs. 3.1 to 3.4. The initial wall temperature is $T_{w0} = 450$ °C. The spray parameters for this case are: $\dot{m} = 2.9$ kg/m²s, $D_{10} = 55$ μm and $U = 10.3$ m/s.

The evolution of the temperature profiles $T(z)$ is calculated by solving the inverse heat conduction problem and is shown in Fig. 3.1 for different times t . The z coordinate coincides with the spray axis while the position $z = 0$ corresponds to the wall surface, where the spray impact takes place. The bottom of the heated plate corresponds to $z = 53.2$ mm.

The vertical dashed lines in Fig. 3.1 indicate the position of the thermocouples at $z_1 = 0.5$ mm and $z_2 = 20$ mm. The temperature measurements of the thermocouples are used as the input data for the solution of the inverse heat conduction problem.

The corresponding time series of the surface temperature and heat flux are plotted in Fig. 3.2. In Fig. 3.3 the heat flux is plotted as a function of the surface temperature, which shows good agreement to the schematic diagram in Fig. 1.3. The vertical dashed lines in Figs. 3.2 and 3.3 correspond to the boundaries of the boiling regimes: film boiling, transition boiling and nucleate boiling regime, which are described in more detail in Figs. 3.4 and 3.5.

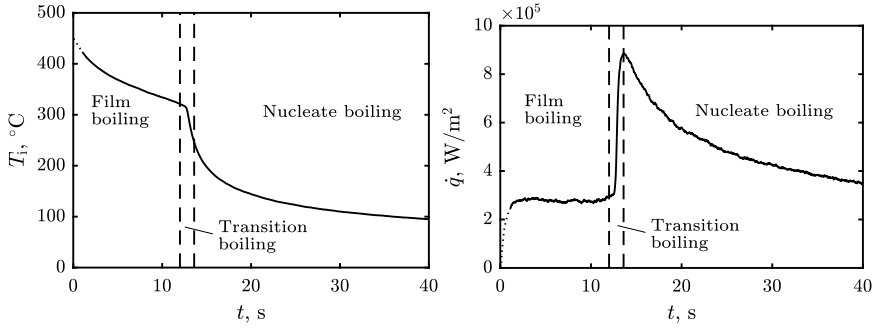


Figure 3.2: Typical temporal evolution of the surface temperature $T_i(t)$ and instantaneous local heat flux $\dot{q}(t)$. The vertical dashed lines indicate the boundaries between film boiling, transition and nucleate boiling. (Adapted from Tenzer et al. (2019b), with permission of Cambridge University Press. © 2019 Cambridge University Press.)

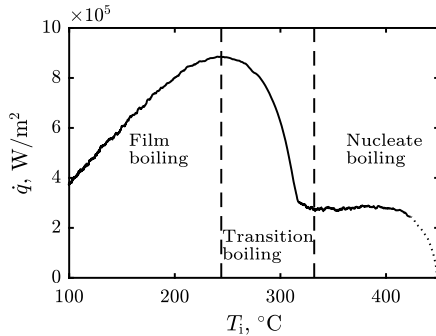


Figure 3.3: Typical evolution of the instantaneous local heat flux $\dot{q}(t)$ as a function of the surface temperature $T_i(t)$. The vertical dashed lines indicate the boundaries between film boiling, transition and nucleate boiling.

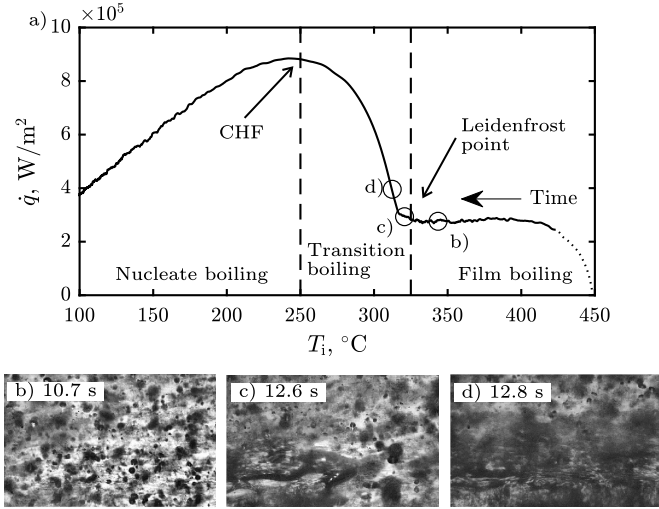


Figure 3.4: Spray cooling regimes at different surface temperatures $T_i(t)$ around the Leidenfrost point. a) Measured heat flux \dot{q} as a function of surface temperature T_i ; b) visualized spray impact in the film boiling regime; c) at the Leidenfrost point, characterized by the first appearance of liquid patches; d) the fast expansion of the liquid spots. (Adapted from Tenzer et al. (2019b), with permission of Cambridge University Press. © 2019 Cambridge University Press.)

3.2 Visualization of the spray impact

Near field observation In Fig. 3.4a the instantaneous local heat flux $\dot{q}(t)$ in the central area of the target and spray is plotted as a function of the surface temperature $T_i(t)$ for the same experimental data as in Figs. 3.1 to 3.3, whereby time t increases following the curve to the left.

The precision of the thermal measurements at the initial stage of cooling is not high, because of the very high temperature gradients that occur in the first instances of cooling. The rise time of the thermocouples is not short enough and the thermal inertia of the material between the tip of the thermocouple and the surface is too high to precisely capture these fast temperature changes. This part of the plot, where the measurement precision is not well quantified, is indicated here and in the following figures by a dotted curve.

In Fig. 3.4b, 3.4c and 3.4d images of spray impact and hydrodynamic phenomena at the surface captured at different instants after the spray cooling begins are shown. The time instants chosen for these images are marked on the graph in Fig. 3.4a.

The hydrodynamic phenomena visualized in Fig. 3.4b, 3.4c and 3.4d are each different, since they correspond to different drop and spray impact thermodynamic regimes. In Fig. 3.4b each drop impact onto the wall leads to its break up, formation of multiple secondary droplets (Roisman et al., 2018) and rebound. The contact time is short and there is no remaining wetting of the surface. As a result the heat flux is low, which is typical for the film boiling regime. At the Leidenfrost point, illustrated in Fig. 3.4c, a few impacting drops start to wet and spread on the surface - a part of the surface is covered by initial liquid patches. At the next instant the area of the wet patches increases, Fig. 3.4d, and the heat flux starts to rapidly increase. This phenomena correspond to the transition boiling regime.

Similar phenomena in the film and transition regimes are observed in Fig. 3.5b and 3.5c, respectively. The images are of higher contrast, since the mass flux of the spray is smaller in the experiment shown in Fig. 3.5. In Fig. 3.5a the measured heat flux is plotted as a function of the surface temperature measured during continuous spraying. In the illustrated case the spray properties are: $\dot{m} = 0.9 \text{ kg/m}^2\text{s}$, $D_{10} = 43 \text{ }\mu\text{m}$ and $U = 9.8 \text{ m/s}$. In this example the target is initially heated to a surface temperature of $306 \text{ }^\circ\text{C}$.

Shortly before the point where the maximum heat flux is achieved a large portion of the surface is wetted by a liquid water film, as shown in Fig. 3.5c. Small nucleation bubbles form, grow and collapse. The heat flux increases significantly, since the wetted area of the substrate increases rapidly. Heat goes into the overheating of the liquid (sensible heat) and into the formation of bubbles.

At the instant corresponding to the critical heat flux, Fig. 3.5d $T_i = 170 \text{ }^\circ\text{C}$, the surface area is almost completely wetted by liquid. The appearance of a corona of an impacting drop is clear evidence that the drop impacts onto a liquid film (Yarin et al., 2017).

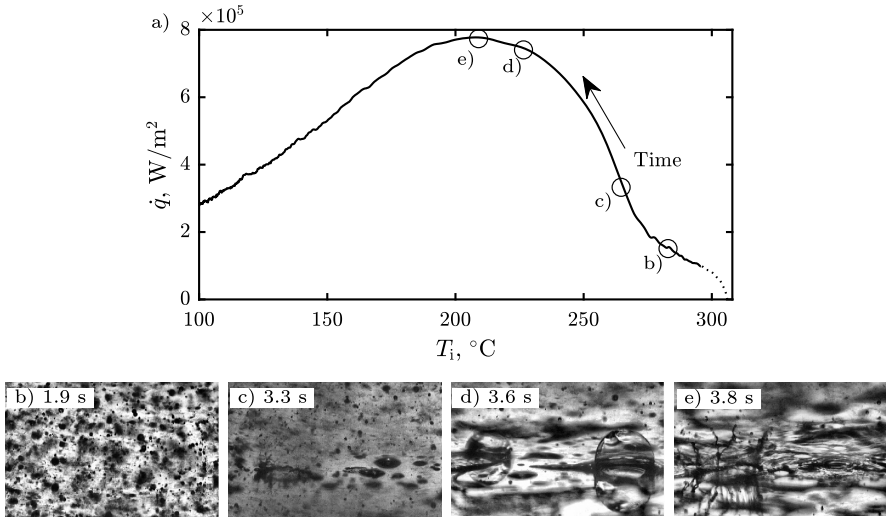


Figure 3.5: Phenomena of spray impact regimes at different surface temperatures $T_i(t)$. a) Measured heat flux \dot{q} as a function of surface temperature T_i ; b) image of the substrate exposed to spray impact in the film boiling regime; c) inception of the transition boiling regime; d) fast expansion of the wetted area; e) apparently completely wetted surface at the instant corresponding to the critical heat flux. (Adapted from Tenzer et al. (2019b), with permission of Cambridge University Press. © 2019 Cambridge University Press.)

At larger times the substrate is completely covered by a thin boiling liquid film. The film is continuously fed by fresh water from the spray and increases in coverage and depth. The heat flux reduces with time. This regime corresponds to fully developed nucleate boiling of spray cooling.

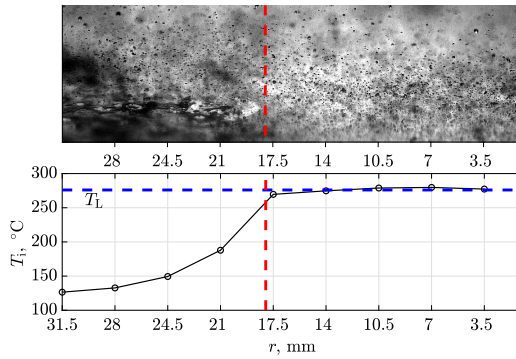
Far field observation By decreasing the magnification of the optical system a larger field of view is achieved. Instead of identifying the individual drop impacts a more macroscopic view of the hydrodynamics and wetting behavior at the surface is possible. Figure 3.6 shows the evolution and movement of the wetting front during spray cooling. The experiment was performed using the *Lechler 490.403* atomizer at 3 bar supply pressure and a distance between atomizer and target of 100 mm. The appropriate radial distribution of the mean droplet diameter, mean droplet velocity and mass flux can be found

in Figs. 2.3a, 2.3b and 2.4. All data and images are taken from the same continuous experiment but at different instants in time. The time t , starting at the moment when the shutter opens, is indicated in the caption of each figure. The images at the top show pictures of the surface where the spray impact takes place. The corresponding radial distribution of surface temperature is indicated in the plot below. The circular markers at the radial positions $r = 3.5, 7, 10.5, \dots$, mm correspond to the positions of the thermocouples. Since the radial positions of picture and plot are matched, a direct comparison between hydrodynamics at the surface and corresponding surface temperature is possible. The vertical dashed line in the picture at the top indicates the area at the surface where the hydrodynamic behavior changes. It is detected from visual observation of the conditions at the surface. The vertical dashed line in the plot at the bottom is simply an elongation and thus corresponds to the same radial position r . In the plot at the bottom, the horizontal dashed line indicates the Leidenfrost temperature, which is determined from the minimum heat flux in the area around $r = 14$ mm.

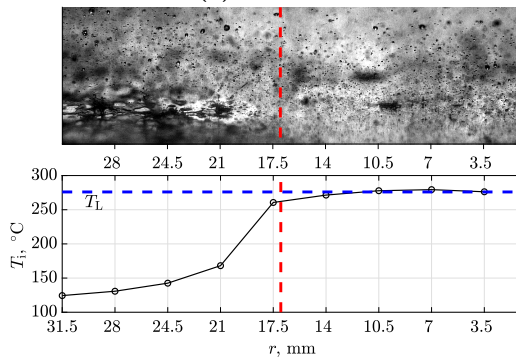
In Fig. 3.6a on the left-hand side of the dashed vertical line a part of the liquid of the impacting droplets remains at the surface after the drop has impacted. A persisting wetting of the surface is present and results in a continuous increase of the amount of water at the surface. This is equivalent to the previously mentioned nucleate boiling regime. The right-hand side of the dashed vertical line corresponds to the film boiling regime: Impacting droplets spread at the surface, atomize and form secondary droplets. However, there is no remaining wetting at the surface. The surface remains dry. Therefore, the vertical dashed line corresponds to the area where the Leidenfrost point is located, which marks the transition between dry and wet droplet impact. The previously discussed transition boiling regime cannot be explicitly identified in this representation. Although not clearly identifiable, this regime also takes place in the area of the dashed line together with the Leidenfrost point.

These observations at the surface correspond to the temperature distribution in the plot at the bottom. On the right side of the vertical dashed line, in the film boiling regime, the temperature is nearly constant. It approximately corresponds to the calculated Leidenfrost temperature (horizontal dashed line). On the left side of the vertical dashed line the temperature strongly decreases. Therefore, the Leidenfrost point corresponds to the point at which the temperature starts to decrease.

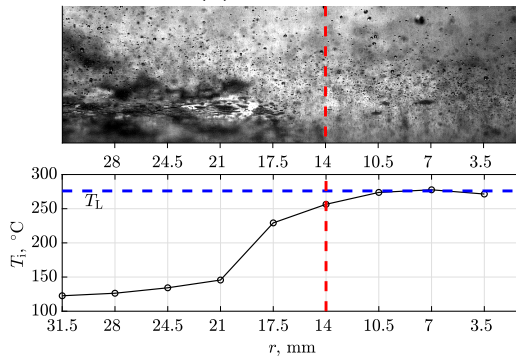
3 Typical results of transient spray cooling



(a) $t = 75.2$ s



(b) $t = 75.5$ s



(c) $t = 76$ s

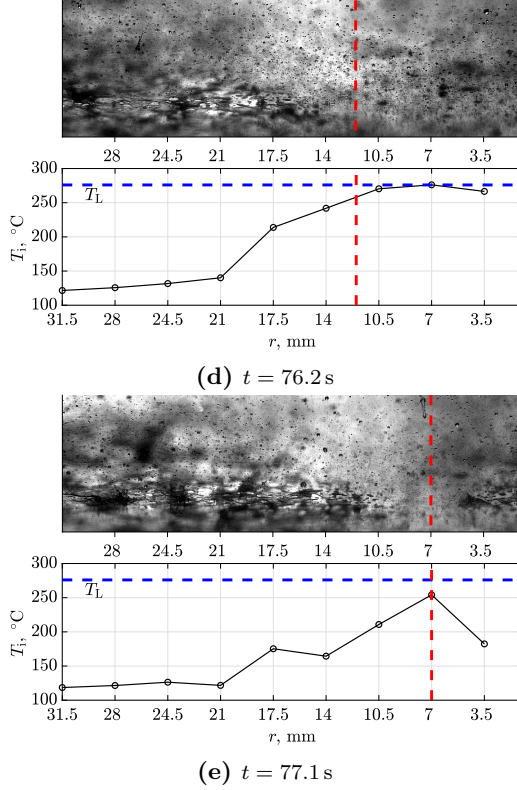


Figure 3.6: Position of the wetting front that follows the Leidenfrost point at different instants of time t . Top image shows the hydrodynamics at the surface. Bottom plot indicates the surface temperature distribution along the radial coordinate r . The vertical dashed line corresponds to the approximate position of the wetting front. The horizontal dashed line indicates the Leidenfrost temperature.

Figs. 3.6b to 3.6d show the same phenomena. Comparing these figures with each other, the movement of the wetting front is visible. Starting at $r = 18$ mm in Fig. 3.6a, the wetting front is at $r = 17$ mm in Fig. 3.6b, at $r = 14$ mm in Fig. 3.6c and finally at $r = 12$ mm in Fig. 3.6d. The movement of the wetting front is a result of the inhomogeneous distribution of the spray properties. As shown in Section 2.2.3, the sprays in this investigation, which were produced using high water supply pressure, tend to have a higher mass

flux at the outer edges of the spray. Therefore at the outer region (left-hand part of the surface in the image) the cooling is more intensive due to the higher mass flux. At the inside (right-hand part of the surface in the image) the mass flux is lower resulting in a less intensive cooling. This results in a wetting front that moves from the outside to the inside with increasing time.

A slightly different behavior can be observed in Fig. 3.6e, which is still the same experiment, but at some instants later. Here a second wetted spot is visible at the inside of the target (right-hand side of the dashed line), which is again a result of the inhomogeneous spray distribution. At this instant the wetting pattern at the surface directly corresponds to the radial distribution of the mass flux, as shown in Fig. 2.4. In summary, we identify a moving wetting front that starts at the outer region. It moves towards the inside and meets at approximately $r = 7$ mm with a second wetting front that forms in the center and moves towards the outside.

The previously shown temporal evolution of the wetting front at the surface is of exemplary nature. Depending on the atomizer, its supply pressure or the distance between atomizer and surface, different wetting patterns are possible. For example in the case of a low atomizer supply pressure, the wetting starts in the center and moves towards the outside, due to the highest mass flux located in the center.

Figure 3.7 summarizes the different hydrodynamic phenomena that occur during spray impact at a hot surface: Film boiling features single drop impacts onto a dry surface. At the Leidenfrost point a small amount of liquid begins to remain on the surface immediately after the drop impact. A first wetting occurs. During the transition boiling regime the amount of liquid wetting the surface increases. Finally, in the nucleate boiling regime a continuous liquid film is formed, which covers the entire surface.

3.3 Influence of various parameters

In the following section the influence of various parameters on the heat transfer is investigated. Some influences are discussed only briefly, since they are addressed again in subsequent chapters. In contrast, others are discussed in more detail, because they are regarded as a prerequisite for further investigation.

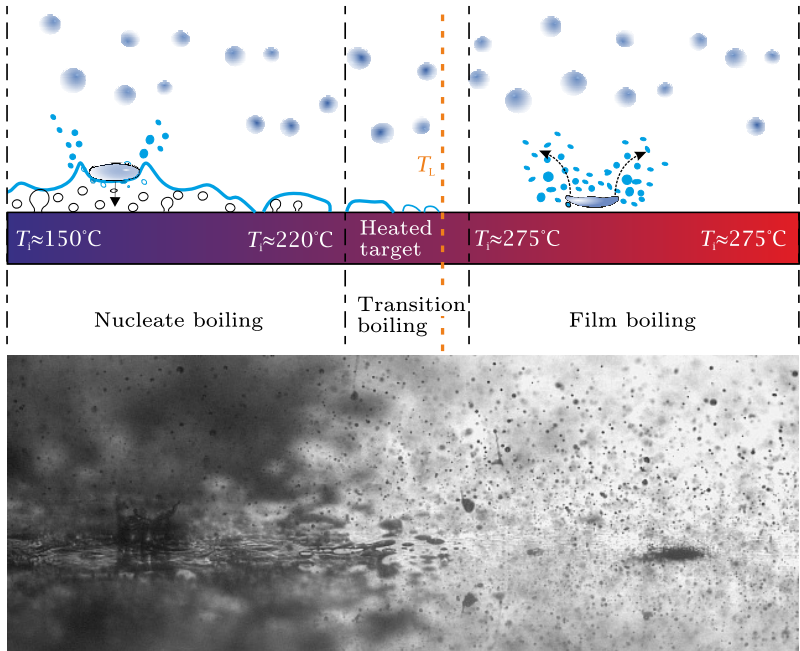


Figure 3.7: Sketch of the hydrodynamics occurring during spray impact. For clarity, the height of the heated target is much smaller than the one used in the experiments. (Adapted from Hofmann (2019).)

3.3.1 Spray impact parameters

To better understand the influence of the main spray parameters on heat transfer, measurements with different mass fluxes were performed. Figure 3.8a shows the heat flux \dot{q} as a function of time t for the mass fluxes 28.1, 9.3, 2.9 and 1.5 kg/m²s. The variation of other spray parameters remain in a relatively narrower range ($D_{10} = 43 - 52 \mu\text{m}$ and $U = 11.2 - 17.4 \text{ m/s}$). The initial substrate temperature is 450 °C for all the tests. The experiments were stopped when the first thermocouple reading reached 100 °C. Increasing the mass flux results in an increased heat flux at all times and boiling regimes. The corresponding surface temperature T_i as a function of time t is shown in Fig. 3.8b. Figure 3.8c shows the same data plotted as heat flux dependence on surface temperature, where the temporal information does not come to the fore.

The slopes of the curves are similar, especially in the nucleate boiling regime, and differ mainly at high temperatures between the start of the cooling experiments and the Leidenfrost point. In this region the heat flux is much lower for sparse sprays (1.5 and 2.9 kg/m²s) than for the more dense sprays (9.3 and 28.1 kg/m²s). Moreover, for $\dot{m} = 9.3$ and 28.1 kg/m²s no film boiling regime can be identified, since the time of the film boiling regime is very short (blue curve in Fig. 3.8a). This can be explained by the limited response time of the thermocouples, which prevents the detection of the Leidenfrost point and film boiling regime in the case of this very fast cooling process. For this reason only those experiments showing the linear trend of the heat flux in the film boiling regime were considered for further analysis of the film boiling regime and the Leidenfrost point.

As shown in Section 2.2.3 the spray parameters cannot be varied independently from one another. For example, increasing the pressure results in faster and smaller droplets, but also changes the mass flux. For this reason a quantitative discussion of the individual dependence of the heat flux on droplet diameter and velocity is avoided, referring instead to Chapter 4. There, the modeling accounts for the influence of each individual parameter. However, it is possible to deduce qualitative trends from Fig. 3.9.

The sprays underlying both experiments in Fig. 3.9 have both the same mass flux ($\dot{m} = 1.2 \text{ kg/m}^2\text{s}$) and the same droplet diameter ($D_{10} = 47 \mu\text{m}$). From the different droplet velocities we can conclude that a higher droplet velocity

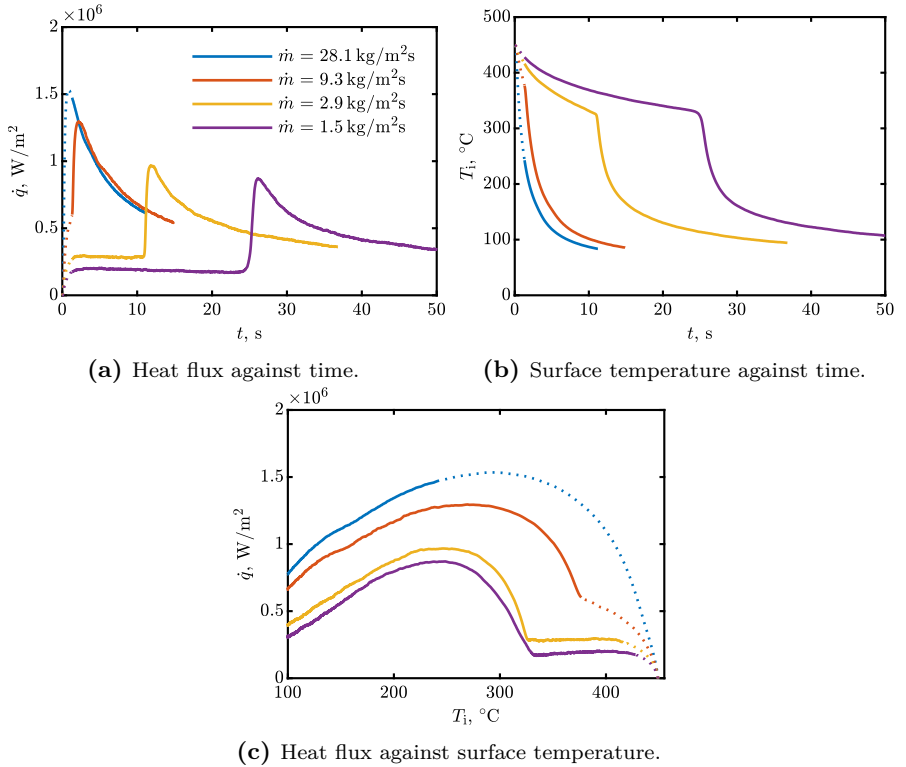


Figure 3.8: Influence of mass flux \dot{m} on the heat transfer. (Adapted from Tenzer et al. (2019b), with permission of Cambridge University Press. © 2019 Cambridge University Press.)

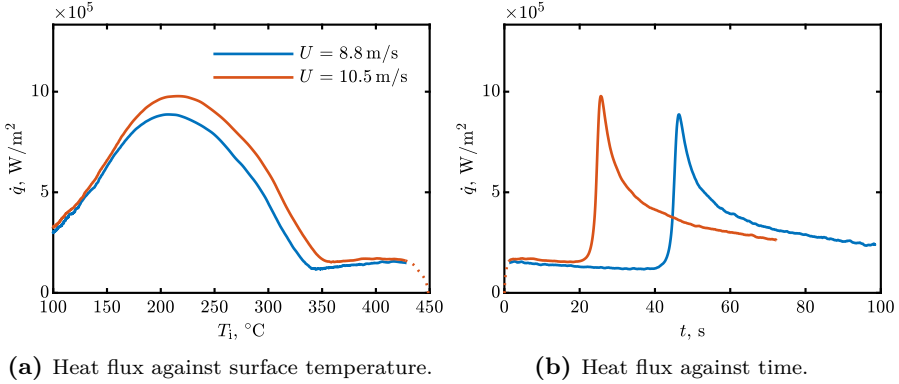


Figure 3.9: Influence of the mean droplet velocity on the heat transfer.

(red curve) results in a higher heat flux, compared to the lower velocity (blue curve). The Leidenfrost point is slightly different, but the overall trend of the curves is comparable. The corresponding plot showing the dependence of the heat flux on time is found in Fig. 3.9b.

Due to the previously mentioned interdependence of the spray parameters, it was not possible to generate sprays with different droplet diameters, but the same velocity and mass flux. Therefore an explicit presentation of the individual influence of the droplet diameter is not possible.

Although for illustration propose only one set of experimental data is shown here, generally the same outcomes are found in the other experiments. Furthermore, the influence of both single drop quantities, droplet diameter and velocity, is rather small compared to that of the mass flux.

Pneumatic atomizing nozzle The present study was conducted primarily using one-component pressure driven atomizers. In contrast, pneumatic atomizers are often used in industrial applications. Due to the compressed air, which is used to support the atomization process, the impacting spray is superimposed on an air stream. To exemplarily capture the influence of an air-assisted spray, a few experiments using a pneumatic atomizing nozzle were performed. These results do not represent a complete parameter study, but provide an initial impression, whether the phenomena are comparable or which new effects occur. A *Lechler 136.115* atomizer is used. For the sake

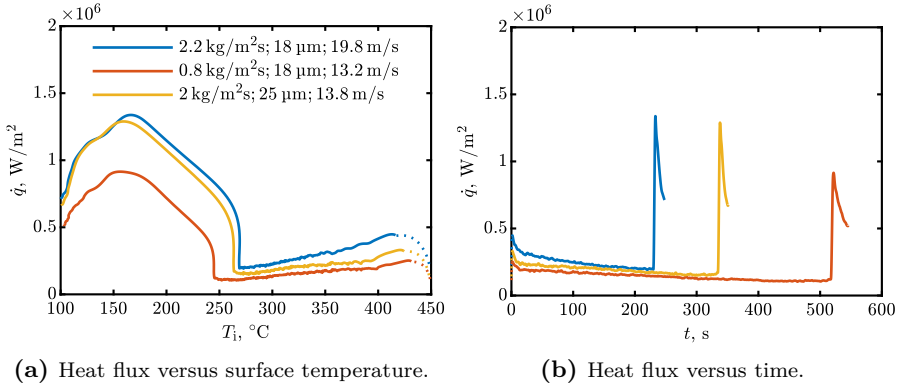


Figure 3.10: Influence of different spray produced by a pneumatic atomizer.

of completeness, it is mentioned that the experiments were performed with the nickel target, whereas the discussion of the influence of different substrate materials follows in Section 3.3.5.

In Fig. 3.10a the heat flux as a function of surface temperature and in Fig. 3.10b of time is shown for different spray properties of a pneumatic atomizing nozzle. Generally the same overall trend can be observed, compared to the previously described experiments performed with one-component atomizers: The Leidenfrost temperatures spread across a comparable range. All boiling regimes are visible. Again a higher mass flux results in a higher heat flux. The experiments take a very long time of up to 600 s, due to very low mass fluxes of some experiments. A quantitative comparison between one-component pressure driven and pneumatic atomizer is not possible because of the large difference in spray properties. Due to its working principle, pneumatic atomizers tend to have smaller and faster droplets than a one-component atomizer. Therefore it is not possible to produce the same kind of spray with the two atomizers.

3.3.2 Spray impact angle

In many spray cooling applications the spray does not impact normal to the surface. Instead there is an inclination between substrate and spray main direction. Figure 3.11 illustrates such an arrangement.

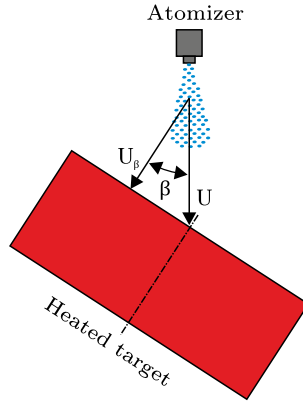


Figure 3.11: Sketch of oblique spray impact.

To capture the influence of an oblique spray impact, experiments with different spray impact angles β (0° , 15° , 30° and 45°) were performed. The angle between target and main spray direction is defined in Fig. 3.11. The exemplary results for one set of spray parameter is shown in Fig. 3.12. The spray parameters are $\dot{m} = 0.9 \text{ kg/m}^2\text{s}$, $D_{10} = 43 \mu\text{m}$ and $U = 10 \text{ m/s}$. Generally, all curves are very similar and correspond to the typical trend, as already discussed in previous sections. A larger spray impact angle results in a lower heat flux inside the film boiling regime. The Leidenfrost temperature moves towards higher temperatures. This influence is nonlinear, meaning the difference between 0° and 15° is smaller than between 30° and 45° . Because the data of the radial distribution of the mass flux is only available for the normal impact case, the shown data is evaluated in the central area below the nozzle.

Since the target is rotated around an axis that is aligned with the geometrical center, it can be assumed that the mass flux in the center remains nearly constant. In this configuration the only changing parameter, when tilting the target surface, is the wall-normal impact velocity of the droplets. This velocity can be calculated by simple geometric considerations,

$$U_\beta = \cos(\beta)U, \quad (3.1)$$

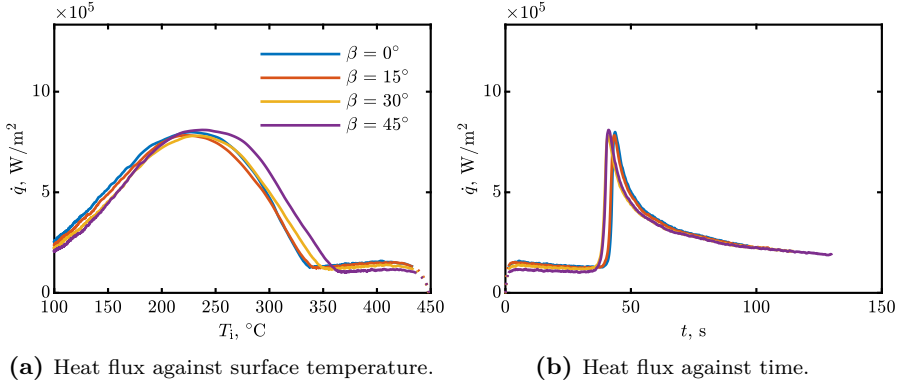


Figure 3.12: Influence of the spray impact angle β .

where U is the mean velocity measured by the phase Doppler system. There is no reason for a changing droplet diameter and the mass flux is assumed to be constant.

In Fig. 3.13 the scaled heat flux in the film boiling regime \dot{q}_β/\dot{q} is plotted as a function of the scaled impact velocity U_β/U for different experiments. Here the indices β correspond to the different impact angles (0° , 15° , 30° and 45°) and \dot{q} is the heat flux obtained during wall-normal impact (0° case). The spray impact parameters of the different experiments are indicated in the figure by different colors. All experimental data collapse onto one straight line having a slope of unity. This indicates that the heat flux in the film boiling regime of an oblique spray impact scales with the wall normal spray impact velocity. Knowing the heat flux of the normal impact \dot{q} , the heat flux for the oblique impact can be calculated according to

$$\dot{q}_\beta = \dot{q} \frac{U_\beta}{U} = \dot{q} \cos \beta. \quad (3.2)$$

3.3.3 Initial spray water temperature

Since there is obviously an influence of the spray fluid temperature on the heat flux, experiments with different spray fluid temperatures $20^\circ\text{C} < T_{f0} < 80^\circ\text{C}$ were performed.

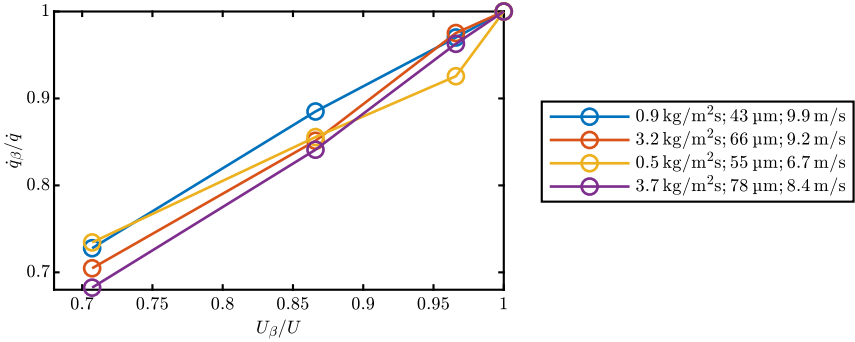


Figure 3.13: Scaled heat flux in the film boiling regime \dot{q}_β/\dot{q} as a function of the scaled impact velocity U_β/U for different spray impact angles β . The different colored lines represent different kinds of sprays.

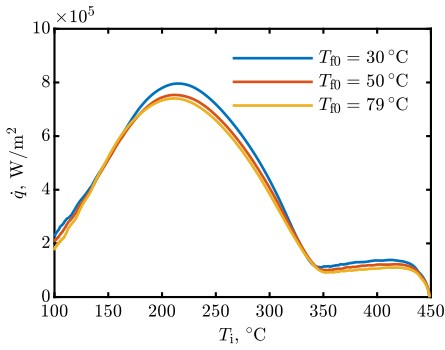


Figure 3.14: Heat flux dependence on the surface temperature for different spray water temperatures. The spray parameters are: $\dot{m} = 0.9 \text{ kg/m}^2\text{s}$, $D_{10} = 43 \text{ }\mu\text{m}$ and $U = 9.9 \text{ m/s}$. (Adapted from Tenzer et al. (2019a).)

In Fig. 3.14 the heat flux \dot{q} is plotted as a function of the surface temperature T_i . Since the surface is continuously cooled and the heating is turned off at the beginning of the spraying process, the curves in this figure can be read as increasing time (t) from higher to lower surface temperatures. The spray parameters are $\dot{m} = 0.9 \text{ kg/m}^2\text{s}$, $D_{10} = 43 \text{ }\mu\text{m}$ and $U = 9.9 \text{ m/s}$. For all different spray water temperatures T_{f0} the commonly known boiling regimes can be identified: film boiling regime, where the heat flux linearly slightly decreases, at high surface temperatures from the beginning of the experiment ($T_i = 450 \text{ }^\circ\text{C}$) until Leidenfrost point is reached ($T_i \approx 340 \text{ }^\circ\text{C}$). After passing the Leidenfrost point the transition boiling regime follows, which is characterized by a strong increase of the heat flux. It ends at the critical heat flux point (maximum heat flux) at $T_i = 215 \text{ }^\circ\text{C}$. After that point the nucleate boiling regime follows, after which the heat flux again decreases.

We can conclude that an increase of the spray water temperature yields a decrease of the heat flux at all surface temperatures and therefore for all boiling regimes. Especially in the film boiling regime and at the critical heat flux, the heat flux is obviously decreased by the higher water temperature. We can further identify the non-linearity of the effect: the drop of the heat flux between $T_{f0} = 30$ and $50 \text{ }^\circ\text{C}$ is higher than that between $T_{f0} = 50$ and $79 \text{ }^\circ\text{C}$.

For further investigation, in Fig. 3.15 we expand the variation of the different water temperatures and only show the film boiling regime and the beginning of the transition boiling regime. The previously mentioned outcomes can easily be confirmed. In addition, the non-linearity results in nearly no difference at high water temperatures (between $T_{f0} = 69$ and $79 \text{ }^\circ\text{C}$). The strongest influence is at low water temperatures and continuously decreases towards higher water temperatures.

Figure 3.15 also leads to a deeper insight into the Leidenfrost point: For the lowest water temperature the Leidenfrost temperature is $T_L \approx 345 \text{ }^\circ\text{C}$ and for the highest water temperature $T_L \approx 350 \text{ }^\circ\text{C}$. The results of the other spray water temperatures are in-between these boundaries. Keeping in mind that the Leidenfrost point is not a distinct point, but more a region where the slope of the curve changes, it is obviously difficult to determine the Leidenfrost point. Therefore, and because of the deviation of only $5 \text{ }^\circ\text{C}$ being very small compared to the change of the water temperature ($50 \text{ }^\circ\text{C}$), the influence of the water temperature on the Leidenfrost point is also weak or even nonexistent.

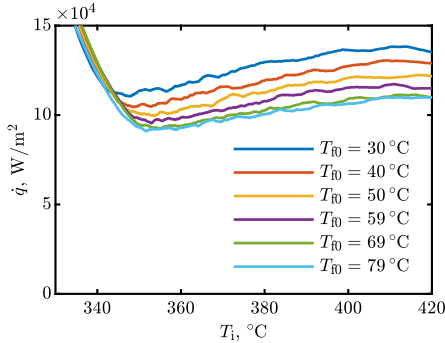


Figure 3.15: Heat flux dependence on the surface temperature for different spray water temperatures. Only film boiling regime, Leidenfrost point and beginning of transition boiling regime are shown. Spray parameters are equivalent to Fig. 3.14. (Adapted from Tenzer et al. (2019a).)

In Fig. 3.16 similar results for a different spray are shown. The inserts show representative pictures of the surface at the corresponding surface temperature and are taken from videos capturing the spray impact. This time the spray properties are $\dot{m} = 2.8 \text{ kg/m}^2\text{s}$, $D_{10} = 54 \mu\text{m}$ and $U = 10.6 \text{ m/s}$. Especially the strong influence of the higher mass flux results in an overall higher heat flux compared to Fig. 3.14. The general trends are comparable to the previously mentioned observations: Higher spray water temperature results in a lower heat flux. The Leidenfrost temperature is only weakly influenced, $T_L \approx 320 \text{ }^\circ\text{C}$.

From the insert on the right we can identify single drop impact onto a dry wall as the leading spray impact mechanism during film boiling at temperatures above Leidenfrost. The insert on the left indicates that at temperatures below Leidenfrost, first small patches of liquid remain and wet the surface (marked in red). From the videos we can identify the Leidenfrost point as the instant, when for the first time a very small wetted spot remains shortly after the impacting drop left the surface, which was already discussed in the previous sections. Also, shown only for one spray water temperature, these observations are independent of the water temperature. We can conclude that different spray water temperatures do not change the hydrodynamics at the surface.

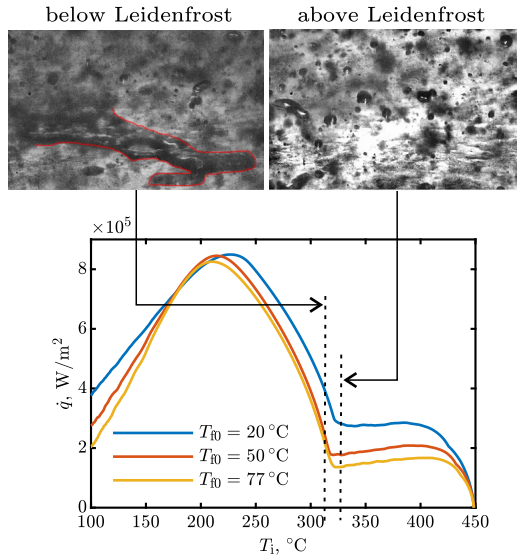


Figure 3.16: Heat flux dependence on the surface temperature for different spray water temperatures. The inserts show the conditions at the surface at the corresponding surface temperature. The shape of the remaining liquid patch at the surface below Leidenfrost is marked in red. The spray parameters are: $\dot{m} = 2.8 \text{ kg/m}^2\text{s}$, $D_{10} = 54 \text{ }\mu\text{m}$ and $U = 10.6 \text{ m/s}$. (Adapted from Tenzer et al. (2019a).)

Compared to Fig. 3.14 the influence of the water temperature on the heat flux, as well as the non-linearity of the effect, are stronger. In addition, the Leidenfrost temperature is lower, $T_L \approx 320^\circ\text{C}$ in contrast to $T_L \approx 345^\circ\text{C}$ in Fig. 3.16.

These results are in strong contrast to the findings in literature. Both experimental studies of Nimi et al. (2012) and Xu & Gadala (2006) conclude a strong decrease of the Leidenfrost temperature for hot water. In our experiments this decrease is not observed, which is confirmed by data from both measurement techniques (inverse heat conduction based on thermocouples and visual observation). From the visual observation we identify single drop impact in the film boiling regime. This leads to the comparison of our spray experimental results to those experimental results of single drop impact: The Leidenfrost temperature of a single drop is not influenced by the water subcooling (Bernardin & Mudawar, 1999), which is in accordance to our results. The Leidenfrost point in sprays and that of single drops share this common feature.

The previously described different Leidenfrost temperature for both series of experiments must be caused by the different sprays of the experiments, since nothing else was changed. The visual observations indicate single drop impact and no film building above Leidenfrost. Therefore we deduce no influence of the mass flux on the Leidenfrost temperature. The remaining possible influencing factors are the drop diameter and velocity. At this stage, from our experiments shown in Figs. 3.14 to 3.16 we identify, that drops having a larger diameter and being faster result in a lower Leidenfrost temperature. This is in contrast to the findings of the influence of the drop velocity on the Leidenfrost temperature of a single drop in the experimental studies of Celata et al. (2006); Bernardin & Mudawar (2004); Testa & Nicotra (2009). Here a higher drop velocity results in a higher drop Leidenfrost temperature.

Let us further try to understand the mechanisms leading to the influence of the water temperature on the heat flux in the film boiling regime. The impacting drop hits the surface and stays in contact with the wall for a very short time. Immediately, heat is transferred from the hot wall to the liquid of the drop by heat conduction. The sensible heat of the drop increases. A thermal boundary layer develops. When the saturation temperature in the liquid is reached at the interface between the drop and the wall, a vapor layer forms and separates the drop from the wall. There is no contact between the

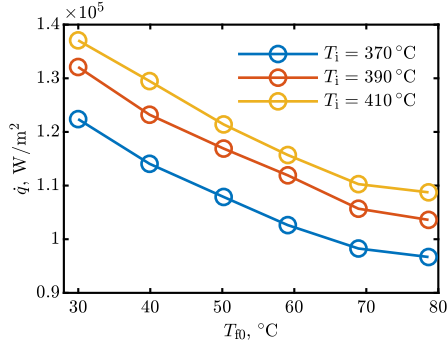


Figure 3.17: Heat flux as a function of the initial spray water temperature. The data and spray parameters are equal to Fig. 3.15. (Adapted from Tenzer et al. (2019a).)

drop and the wall anymore. The drop breaks up due to thermal atomization (Roisman et al., 2018) or inertia. The sensible heat which is necessary to heat the liquid to saturation temperature, so vapor is generated, is higher for a cold water drop. This means more heat from the wall goes into sensible heat of the drop. Therefore, less vapor is generated in the case of cold water compared to the case of a higher initial water temperature. Less vapor results in a smaller vapor layer thickness (Breitenbach et al., 2017b) and a smaller thermal resistance. Therefore the heat flux is higher. Since spray impact in the film boiling regime is a superposition of single drop impacts, the previously discussed behavior of single drop impact can be directly transferred to spray impact.

In Fig. 3.17 we replot the data from Fig. 3.15. This time the heat flux at different surface temperatures T_i is plotted as a function of the spray water temperature. For low water temperatures $T_{f0} < 70$ °C the influence is nearly linear. For higher water temperatures the slope starts to flatten which leads to non-linearity. The slope is comparable for all surface temperatures T_i .

From the experimental results it is obvious, that the sensible heat plays an important role during spray impact at temperatures above Leidenfrost.

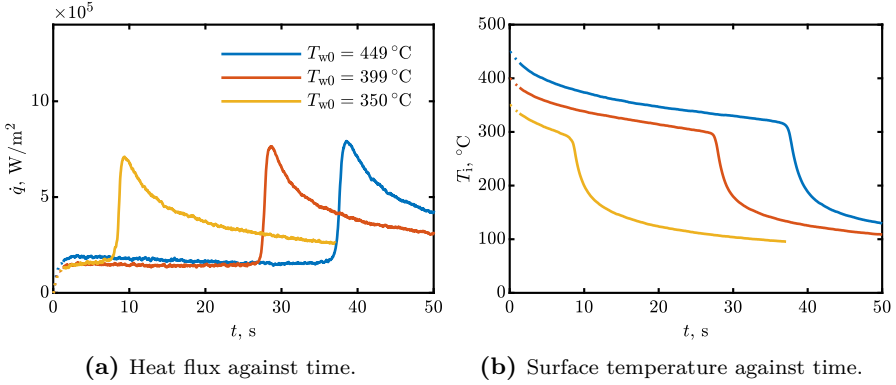


Figure 3.18: Influence of the initial wall temperature T_{w0} for a small mass flux of $\dot{m} = 1.6 \text{ kg/m}^2\text{s}$. (Adapted from Tenzer et al. (2019b), with permission of Cambridge University Press. © 2019 Cambridge University Press.)

3.3.4 Initial substrate temperature

In Fig. 3.18 the heat flux and surface temperature are shown as a function of time for various initial substrate temperatures: 350, 400 and 450 $^\circ\text{C}$. The spray properties are $\dot{m} = 1.6 \text{ kg/m}^2\text{s}$, $D_{10} = 64 \mu\text{m}$ and $U = 8 \text{ m/s}$. To highlight the transient behavior the temporal axis is limited to $t < 50 \text{ s}$. Some minor influence of the initial temperature on the heat flux in the film boiling regime can be identified. However, the overall trend of the curves remain the same. The time shift is a direct result of the different initial substrate temperatures.

Similar curves, but this time for a larger mass flux, are shown in Fig. 3.19. The spray properties are $\dot{m} = 9.3 \text{ kg/m}^2\text{s}$, $D_{10} = 48 \mu\text{m}$ and $U = 15.6 \text{ m/s}$. Again the slopes are comparable but the heat flux at the critical heat flux is higher for the higher initial substrate temperatures. Furthermore, no typical film boiling regime is visible. This can again be explained by the small time scales in the film boiling regime which are of the same order as the rise time of the thermocouples.

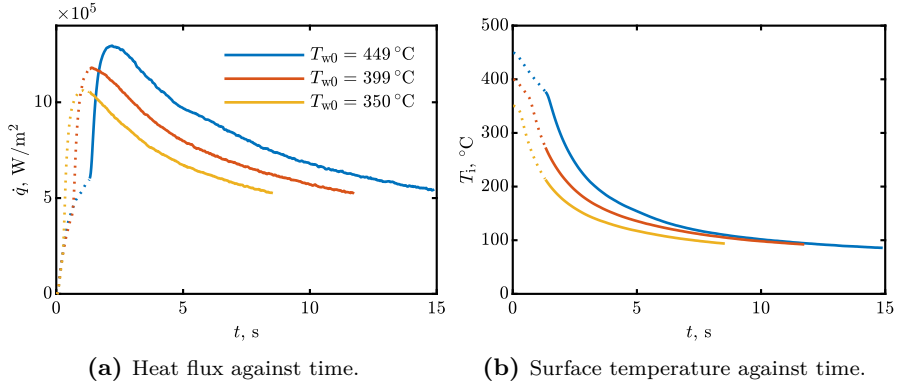


Figure 3.19: Influence of the initial wall temperature T_{w0} for a large mass flux of $\dot{m} = 9.3 \text{ kg/m}^2\text{s}$. (Adapted from Tenzer et al. (2019b), with permission of Cambridge University Press. © 2019 Cambridge University Press.)

3.3.5 Wall thermal properties

Since spray cooling is used in many different cooling applications, there is also a large variety of materials that need to be cooled. This arises the question in which manner the thermal properties of the wall influence the heat flux during spray cooling. To capture this influence, experiments with different wall materials were performed during this investigation. A detailed description of the respective targets and their thermodynamic properties can be found in Table 2.3.

In Fig. 3.20a the heat flux is plotted as a function of the surface temperature for different materials. The spray parameters are held constant for all shown experiments, $\dot{m} = 3.1 \text{ kg/m}^2\text{s}$, $D_{10} = 60 \mu\text{m}$ and $U = 9.3 \text{ m/s}$. The general trend of all curves is comparable and corresponds to the previously described behavior of the other cooling experiments. By comparing the values of the heat flux between each material, we can identify an influence of the substrate material on the heat flux. In all boiling regimes the heat flux is lowest for stainless steel, followed by hot-work tool steel and nickel. Especially in the film boiling regime we can identify that the difference between stainless steel and hot-work tool steel is smaller than between hot-work tool steel and nickel. This indicates a positive correlation between thermal conductivity of the substrate material and heat flux. The critical heat flux as well as the heat flux

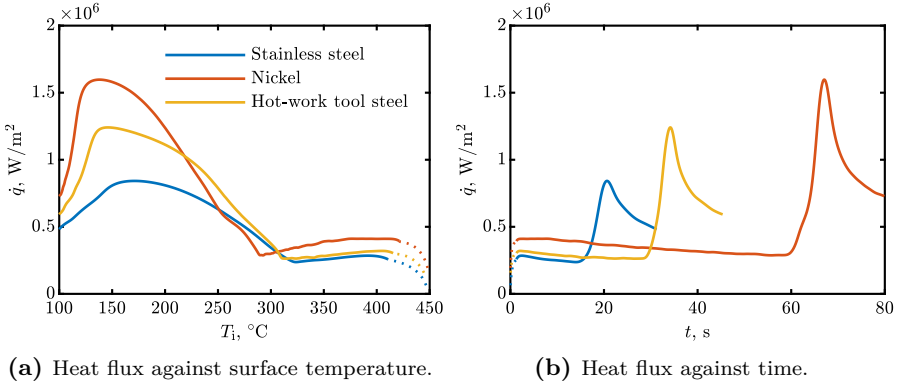


Figure 3.20: Influence of the substrate material on the heat transfer for a constant rather sparse spray.

in the film boiling regime follow the same trend. Comparing the Leidenfrost temperature for the three different materials, a negative correlation between this temperature and the thermal conductivity can be identified. This means a higher thermal conductivity results in a lower Leidenfrost temperature. In Fig. 3.20b the corresponding dependence of the heat flux on time is shown. Here we can again identify the same general slopes for all curves. Since all curves end when a surface temperature of 100°C is reached, the curves show an influence of the substrate material on the cooling time. The experiment performed with stainless steel takes a shorter time, followed by hot-work tool steel and nickel. This temporal difference arises mainly during the film boiling regime. The time between Leidenfrost point, critical heat flux and end of the experiment is comparable for the different materials.

Fig. 3.21 shows a second exemplary set of experiments having the same spray parameters but different substrate materials. This time the spray is much more dense. The properties are $\dot{m} = 11.9 \text{ kg}/\text{m}^2\text{s}$, $D_{10} = 79 \mu\text{m}$ and $U = 10.2 \text{ m}/\text{s}$. The curve shows obviously different general trends. From the curve measured with the stainless steel target (blue) no film boiling can be distinguished. This curve does not exhibit the typical shape and boiling regimes. As previously stated in Section 3.3.1, this is caused by the limited temporal response of the measurement system in combination with the short time until the critical heat flux is reached, as seen in Fig. 3.21b. The curve

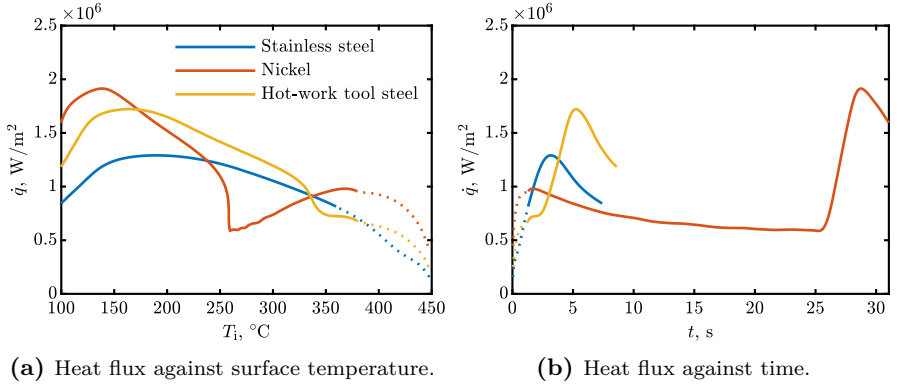


Figure 3.21: Influence of the substrate material on the heat transfer for a constant rather dense spray.

of hot-work tool steel (yellow) slightly resembles the typical trend we know from previous experiments. However, the timescales are rather short, so that the data inside the film boiling regime is not considered so reliable. The experiment performed with nickel (red) clearly shows the typical behavior: We can identify the film boiling, transition and nucleate boiling regime. The slope in the film boiling regime is rather steep compared to previously discussed results. This appears to be connected to the heat flux inside the film boiling regime: A higher heat flux results in a steeper slope. Furthermore this slope is highest at the beginning of the experiment, except for the part indicated by dashed line, where the rise time prevents valid data. It flattens with increasing time. Since the time in the film boiling regime is long (Fig. 3.21b), this data is regarded as valid and can be used for further analysis.

Using nickel as target material, experiments with mass fluxes of up to $30 \text{ kg}/\text{m}^2\text{s}$ can be performed, while still achieving reasonable results in the film boiling regime. For stainless steel this range ends at approximately $8 \text{ kg}/\text{m}^2\text{s}$, depending on the other parameters. Therefore, for nickel a much larger span of spray parameters can be used for investigating the influences on heat transfer.

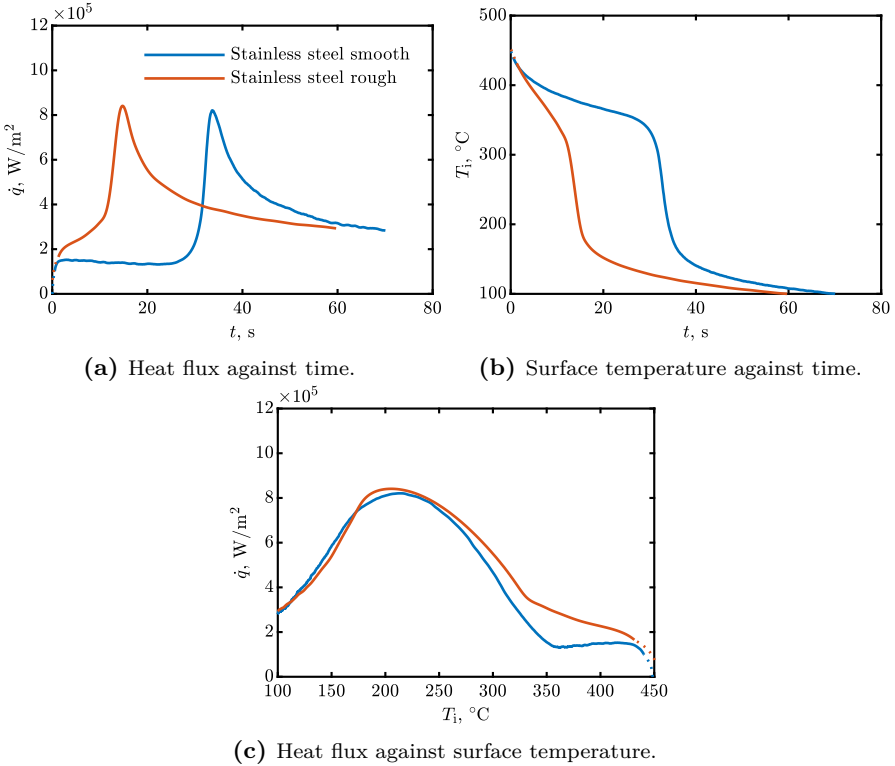


Figure 3.22: Influence of the surface roughness on the heat transfer, for a small mass flux of $1 \text{ kg}/\text{m}^2\text{s}$.

3.3.6 Wall surface roughness

In many industrial processes surfaces spray cooling involves rough surfaces, arising either from abrasive wear or for other reasons. To investigate the influence of surface roughness on the heat transfer some preliminary experiments on a sandblasted surface were performed. The surface material of both targets used in these tests was stainless steel. Further details can be found in Section 2.3.

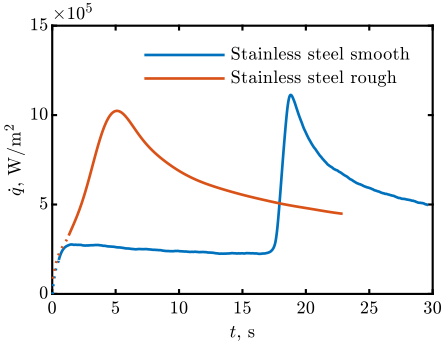
A comparison between a smooth and rough target is shown in Fig. 3.22. The spray properties of both experiments are identical: $\dot{m} = 1 \text{ kg/m}^2\text{s}$, $D_{10} = 51 \text{ }\mu\text{m}$ and $U = 9.4 \text{ m/s}$. The heat flux of the rough target is higher than that of the smooth target. Particularly notable is that for surface temperatures above the Leidenfrost point, the heat flux for the rough surface does not decrease with decreasing temperature, but increases.

In the nucleate boiling regime, after reaching the maximum heat flux, both surfaces result in the same temperature dependence of heat flux (Fig. 3.22c). For the rough surface a distinct Leidenfrost point is no longer distinguishable, since there is no minimum of the heat flux following the film boiling regime. The curve in this diagram suggests a lower Leidenfrost point due to the change of the slope at $T_1 \approx 335 \text{ }^\circ\text{C}$; however, since a minimum heat flux is not achieved, no valid prediction is possible.

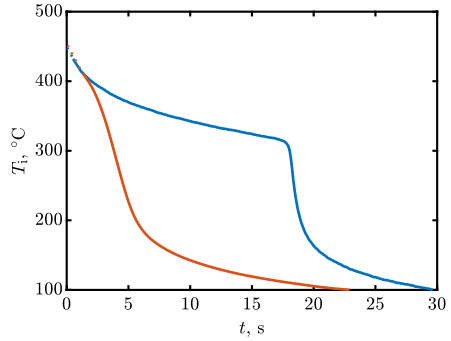
The corresponding temporal evolution in Figs. 3.22a and 3.22b show basically the same outcomes. The time spent in the film boiling regime is shorter for the rough surface compared to the smooth one. This is in accordance with the higher heat flux in the film boiling regime. The timescales spent in the nucleate boiling regime are comparable.

For the sake of completeness Fig. 3.23 shows results for a slightly higher mass flux of $\dot{m} = 3.1 \text{ kg/m}^2\text{s}$. The other parameters are: $D_{10} = 60 \text{ }\mu\text{m}$ and $U = 9.3 \text{ m/s}$. For this case we cannot identify a film boiling regime for the rough target. This is again due to the short timescales resulting from the higher heat flux, which are then comparable to the rise time of the temperature measurement system.

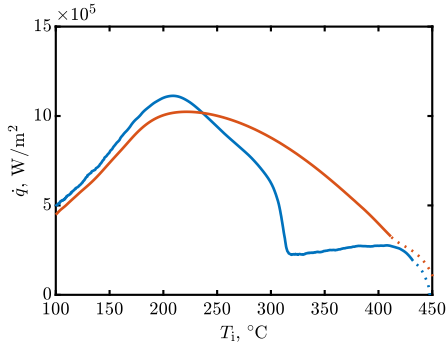
As a conclusion we can summarize that surface roughness strongly increases the heat flux in the film boiling regime, whereas there is no impact on the nucleate boiling regime. It is remarkable that the heat flux in the film boiling does not decrease with decreasing surface temperature, which is well known for smooth surfaces. Instead it exhibits the opposite behavior and increases with decreasing surface temperature. It is not possible to develop a more elaborate theory or explanation for this observation based only on the results of these preliminary experiments. Instead, these results suggest a new topic for further research.



(a) Heat flux against time.



(b) Surface temperature against time.



(c) Heat flux against surface temperature.

Figure 3.23: Influence of the surface roughness on the heat transfer, for a small mass flux of $3.1 \text{ kg/m}^2\text{s}$.

4 Heat transfer in film boiling regime

In this chapter a predictive model for the heat flux and surface temperature in the film boiling regime is developed. Originally the model was derived for the heated target built of stainless steel, which is discussed in the first part of this chapter. In the second part the model is validated against experimental data. Here we also take into account experimental data acquired with other target materials, to show the universality of the theoretical model.

Parts of this chapter have already been published in Tenzer et al. (2019b).

4.1 Analysis of heat transfer during spray cooling

Let us analyze heat transfer during very intensive transient spray cooling of an initially uniformly heated substrate. Consider for simplicity one-dimensional heat conduction in a semi-infinite solid substrate. This assumption is valid for cases when the thickness of the thermal boundary layer, $\sqrt{\alpha t}$, is much smaller than the thickness of the target, and the temperature gradients in this boundary are much higher than the gradients associated with the spray distribution in the radial direction. Here $\alpha = \lambda/\rho c_p$ is the thermal diffusivity, where λ is the thermal conductivity, ρ is the density and c_p is the heat capacity of the target material.

In our case the material properties of the stainless steel substrate are: $\lambda = 16 \text{ W/mK}$, $\rho = 7900 \text{ kg/m}^3$ and $c_p = 542 \text{ J/kgK}$. The longest experiments last about 200 s. This results in a thermal boundary layer thickness of about 30 mm which is comparable to half of the target height. Therefore the heat conduction in the target can be considered as semi-infinite. Since the spray parameters are nearly constant in the central area the assumption of a one-dimensional problem is valid.

Consider also a coordinate system $\{z, t\}$ fixed at the interface $z = 0$ of the semi-infinite target, belonging to the interval $0 < z < \infty$. The temperature field $T(z, t)$ in the target can be calculated by solving the one-dimensional heat equation

$$\frac{\partial T}{\partial t} = \alpha \frac{\partial^2 T}{\partial z^2}. \quad (4.1)$$

Following Duhamel's theorem (Özışık, 1980), the solution which satisfies the boundary condition far from the target interface and the initial condition

$$T = T_{w0} \quad \text{at} \quad (t = 0 \wedge z \in [0, \infty]) \quad \vee \quad (t > 0 \wedge z \rightarrow \infty), \quad (4.2)$$

is

$$T(t) = T_{w0} + \int_0^t A(\tau) \operatorname{erfc} \left[\frac{z}{2\sqrt{\alpha(t-\tau)}} \right] d\tau, \quad (4.3)$$

where $A(\tau)$ is a function determined by the conditions at the target interface $z = 0$, erfc is the complementary error function and T_{w0} is the initial wall temperature. As usual, the limit $z \rightarrow \infty$ denotes a position at a finite distance much larger than the thickness of the thermal boundary layer in the wall. Equation (4.3) allows the general solution for the interface temperature $T_i(t)$ and for the heat flux $\dot{q}(t)$ to be determined

$$T_i(t) = T_{w0} + \int_0^t A(\tau) d\tau, \quad \dot{q}(t) = -\frac{\epsilon_w}{\sqrt{\pi}} \int_0^t \frac{T_i'(\tau)}{\sqrt{t-\tau}} d\tau, \quad (4.4)$$

where

$$\epsilon_w = \sqrt{\lambda \rho c_p} \quad (4.5)$$

is the thermal effusivity of the wall.

4.2 Modelling of temperature and heat flux evolution

The theoretical model published by Breitenbach et al. (2017b) for the heat transfer from a single drop and during spray cooling in the film boiling regime is based on the analysis of the heat conduction in the substrate, heat convection

in the liquid region and in an expanding thin vapor layer emerging between the impacting drop and the very hot substrate. The mass flux of the vapor generated at the lower liquid interface is determined from the energy balance at this interface. This model has already been validated by comparison with experimental results from literature (Wendelstorf et al., 2008). Moreover, the predicted vapor layer thickness agrees well with the direct measurements of Tran et al. (2012) and Chaze et al. (2019). Predictions for the evolution of the heat flux $\dot{q}(t)$ also agree with the accurate measurements based on the infrared technique (Chaze et al., 2019).

The total heat transferred during the impact of a single drop Q_{single} is determined by integration of the heat flux $\dot{q}(t)$ over the “apparent contact area” during the contact time. It should be noted that the contact area cannot be based on the drop spreading diameter, since the free lamella in the remote regions can levitate (Roisman et al., 2018). Therefore the values of D^2 and D/U are used as the scales for the contact area and for the contact duration, where U and D are the impact velocity and drop diameter, respectively.

This analysis (Breitenbach et al., 2017b) allows the heat flux during spray impact in the film boiling regime to be predicted

$$\dot{q} = S\epsilon_w(T_i - T_{\text{sat}}), \quad (4.6)$$

$$S = 8.85\chi \frac{\dot{m}}{\rho_f D_{10}^{1/2} U^{1/2} \left[1 - b + \sqrt{(1 - b)^2 + w} \right]}, \quad (4.7)$$

$$w = \frac{8(T_i - T_{\text{sat}})\epsilon_w^2}{\pi\lambda_v\rho_f L}, \quad b = \frac{2\sqrt{5}\epsilon_w\epsilon_f(T_{\text{sat}} - T_{f0})}{\pi\rho_f\lambda_v L}, \quad (4.8)$$

where L is the latent heat of evaporation, χ is a dimensionless fitting parameter which depends on the substrate wetting properties and roughness (but is of order unity), T_{sat} is the saturation temperature of the liquid and T_{f0} is the initial spray fluid temperature. All terms with the subscript “f” correspond to the liquid (fluid) component, “w” to the wall and “v” to the vapor.

Since the sprays used in the experiments and in practical applications are always polydisperse, the average drop diameter and velocity, D_{10} and U , are used in the model. Thus the parameter χ inherently accounts also for the influence of the drop size and velocity distributions.

Table 4.1: Typical conditions of spray cooling experiments of this study.

Quantity	Value
T_i	340 °C
T_{sat}	99 °C
ϵ_w	8432 J/Km ² s ^{1/2}
λ_v	0.0248 W/mK
ρ_f	998 kg/m ³
L	2453 kJ/kg
ϵ_f	1581 J/Km ² s ^{1/2}
T_{f0}	20 °C

In this study the model (Eqs. (4.6) to (4.8)) is used for prediction of the evolution of the wall temperature in time. The predictions are then compared with our experimental data.

For typical experimental conditions of this study, shown in Table 4.1, the estimated values for w and b defined in Eq. (4.8) are $w \approx 700$ and $b \approx 25$. Since $b \gg 1$ and b^2 and w are of the same order of magnitude, the effect of the dependence of S on the changing temperature T_i in the expression for w can be neglected. The value of S can be estimated by using T_{w0} instead of $T_i(t)$ in the Eq. (4.8).

Equations (4.4) and (4.6) lead to the following integral equation for the surface temperature, presented in the dimensionless form

$$\Theta(\xi) + \int_0^\xi \frac{\Theta'(\zeta)}{\sqrt{\xi - \zeta}} d\zeta = 0, \quad (4.9)$$

where the surface temperature is made dimensionless using

$$\Theta = \frac{T_i(t) - T_{\text{sat}}}{T_{w0} - T_{\text{sat}}}, \quad \xi = t\pi S^2, \quad \zeta = \tau\pi S^2. \quad (4.10)$$

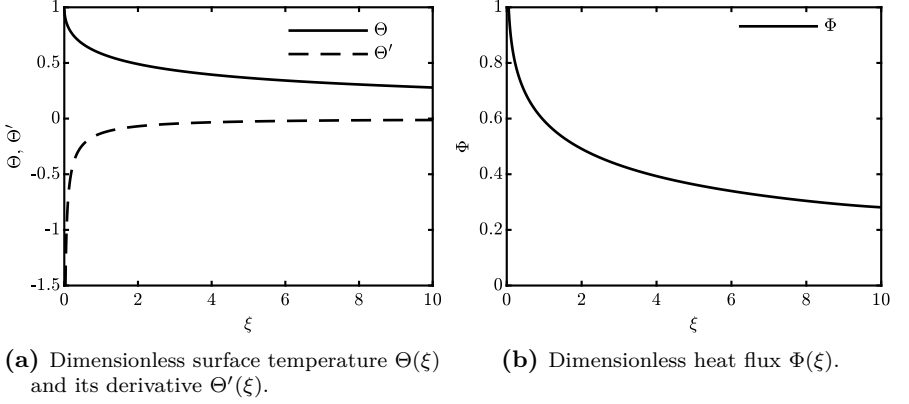


Figure 4.1: Theoretically predicted evolution of the dimensionless quantities as functions of the dimensionless time ξ in the film boiling regime.

This equation can be solved subjected to the initial condition $\Theta(0) = 1$. The analytical solution for $\Theta(\xi)$ can be represented as a series

$$\Theta(\xi) = 1 + \sum_{i=1}^{\infty} a_i \xi^{i/2}, \quad (4.11)$$

$$a_1 = -\frac{2}{\pi}, \quad a_2 = \frac{1}{\pi}, \quad a_3 = -\frac{4}{3\pi^2}, \quad \dots,$$

$$a_{i+1} = -a_i \frac{2^{-i} \Gamma(i+1)}{\Gamma\left[\frac{i+1}{2}\right] \Gamma\left[\frac{i+3}{2}\right]} \quad (4.12)$$

where Γ is the gamma function. The series Eq. (4.12) converges on the interval $0 < i < 22$. Therefore it is sufficient to calculate Eq. (4.11) in this interval.

The corresponding heat flux \dot{q} can be estimated using Eq. (4.4)

$$\dot{q} = S\epsilon_w(T_{w0} - T_{\text{sat}})\Phi(\xi), \quad (4.13)$$

$$\Phi(\xi) = - \int_0^{\xi} \frac{\Theta'(\zeta)}{\sqrt{\xi - \zeta}} d\zeta, \quad \Theta'(\zeta) = \frac{1}{2} \sum_{i=1}^{\infty} a_i i \zeta^{i/2-1}. \quad (4.14)$$

The solution for the dimensionless surface temperature $\Theta(\xi)$, its derivative $\Theta'(\xi)$ and the dimensionless heat flux $\Phi(\xi)$ are shown in Fig. 4.1.

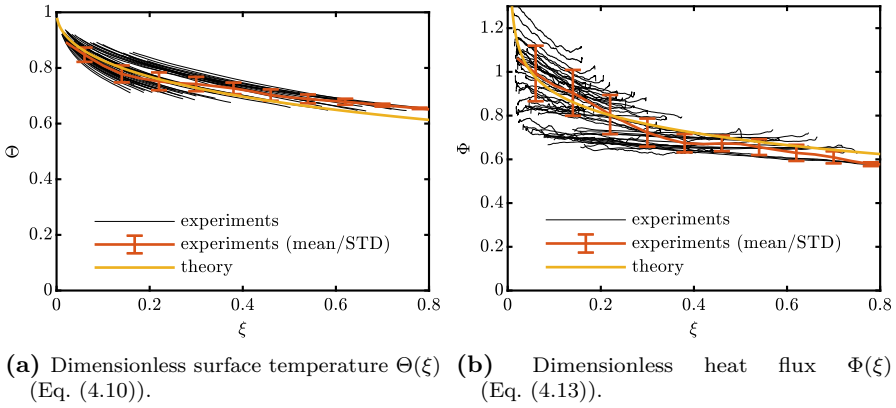


Figure 4.2: Evolution of the dimensionless quantities for the stainless steel target as a function of the dimensionless time ξ for experimental data in the film boiling regime and for the theoretical solution (Eqs. (4.9) and (4.14)). (Adapted from Tenzer et al. (2019b), with permission of Cambridge University Press. © 2019 Cambridge University Press.)

4.3 Model validation

In the following section the model is validated against experimental data, organized according to the material which is being considered.

Stainless steel target In Fig. 4.2a the measured evolution of the dimensionless surface temperature $\Theta(\xi)$ as a function of dimensionless time ξ is plotted for the theoretical prediction (Eq. (4.11)) and for experimental results. The computation of the theoretical solution is based on the first 50 terms of the series. It converges on the interval $0 < \xi < 22$. The line shown for the experiments is the mean and the error bars indicate the standard deviation computed over 49 experiments. For the reduction of the experimental data T_i and t , χ in (Eq. (4.7)) is fitted to the experimental data using a least square fit, resulting in $\chi = 2.2$. Only the experiments exhibiting clear film boiling behaviour are chosen and the experimental data comprising the film boiling regime are plotted. We skip the experiments showing no film boiling behaviour because of the previously mentioned limited temporal response of the measure-

ment system. The experimental parameters corresponding to the experimental data span the following ranges: $\dot{m} = 0.5 - 9.1 \text{ kg/m}^2\text{s}$, $D_{10} = 43 - 78 \text{ }\mu\text{m}$, $U = 6.7 - 15.9 \text{ m/s}$, $T_{w0} = 350 - 450 \text{ }^\circ\text{C}$ and $T_{f0} = 18 - 80 \text{ }^\circ\text{C}$.

In Fig. 4.2b the corresponding evolution of the dimensionless heat flux for the same experiments is shown and compared to theory. Although there is obviously a large scatter in the experimental data, very good agreement between the experiments and theory can be observed. Especially χ , being close to unity, indicates the performance of the theory, which clearly captures all main physical players. The shown data consists of different sources like phase Doppler, patternator and heat flux data, each having numerous sources of uncertainty. Keeping that in mind, the scatter is acceptable and therefore the good agreement between experiment and theory indicates a good understanding of the physics of spray cooling in the film boiling regime.

Hot-work tool steel target This work is motivated amongst others by the hot forging industry and should contribute to a better design of cooling processes. Therefore it is mandatory that the developed models are valid for the materials used in hot forging.

In Fig. 4.3a the dimensionless surface temperature $\Theta(\xi)$ is plotted against the dimensionless time ξ for the experimental data performed with the target built of hot-work tool steel (1.2365) and the theoretical prediction (Eq. (4.11)). Figure 4.3b shows the corresponding evolution of the dimensionless heat flux $\Phi(\xi)$.

The thermal properties of the target, which can be found in Table 2.3 are used for the data reduction and calculation of the theoretical prediction. The parameter χ is again fitted to the experimental data. The resulting value $\chi = 1.9$ is different, but still comparable and quite close to the value of the stainless steel target (as discussed in the previous paragraph). Keeping in mind the limited amount of data for the hot-work tool steel targets, the agreement is very good. This indicates the universality of the model.

Again we can identify a very good agreement between experimental data and theoretical prediction. Compared to Fig. 4.2 the scatter is smaller, which is again a result of the larger time scales due to the larger thermal conductivity of the material, as discussed in Section 3.3.5. Due to the low resistance against corrosion and oxidation, only a few experiments with the target built of hot-work tool steel could be performed. Therefore the amount

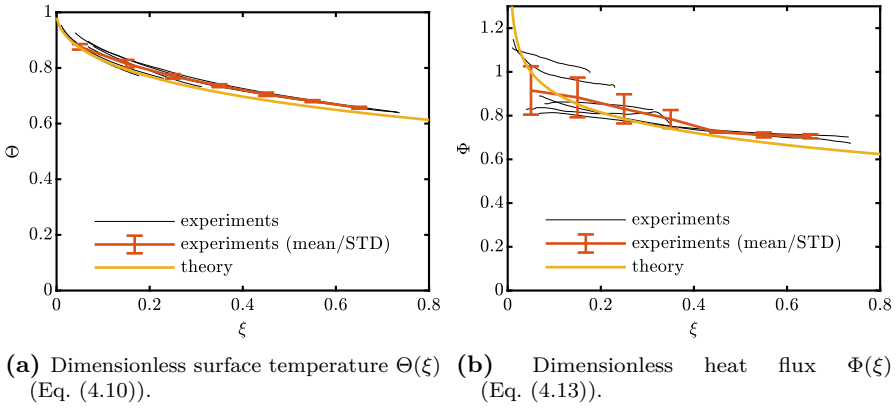


Figure 4.3: Evolution of the dimensionless quantities for the hot-work tool steel target as a function of the dimensionless time ξ for experimental data in the film boiling regime and for the theoretical solution (Eqs. (4.9) and (4.14)).

of data having different spray properties is also much smaller compared to the experiments with other targets. The spray properties of these 6 experiments only spread across the following range: $\dot{m} = 1.1 - 4.4 \text{ kg/m}^2\text{s}$, $D_{10} = 43 - 77 \text{ }\mu\text{m}$, $U = 7.9 - 14.9 \text{ m/s}$, $T_{w0} = 410 - 449 \text{ }^\circ\text{C}$ and $T_{f0} = 19 - 21 \text{ }^\circ\text{C}$.

Nickel target Fig. 4.4 shows again the validation of the model for the film boiling regime against experimental data. This time the data is obtained with the target built of nickel. The parameter χ is again fitted to experiments yielding $\chi = 2.2$, which is the same as for the stainless steel target. As previously stated in Section 3.3.5, the nickel target leads to a much larger span of different sprays which can be used for the cooling experiments. This becomes particularly obvious from the much larger mass flux. The spray properties underlying the 61 experiments are: $\dot{m} = 0.6 - 29.5 \text{ kg/m}^2\text{s}$, $D_{10} = 41 - 117 \text{ }\mu\text{m}$, $U = 5.2 - 23.7 \text{ m/s}$, $T_{w0} = 300 - 462 \text{ }^\circ\text{C}$ and $T_{f0} = 18 - 23 \text{ }^\circ\text{C}$.

Again there is a very good agreement between experimental data and theoretical prediction. Especially the strong decrease of the theoretical prediction for small dimensionless times ξ in Fig. 4.4b is well represented by the experiments. In Fig. 4.4a some small discrepancy between experiment and prediction of the dimensionless surface temperature exist. These are caused

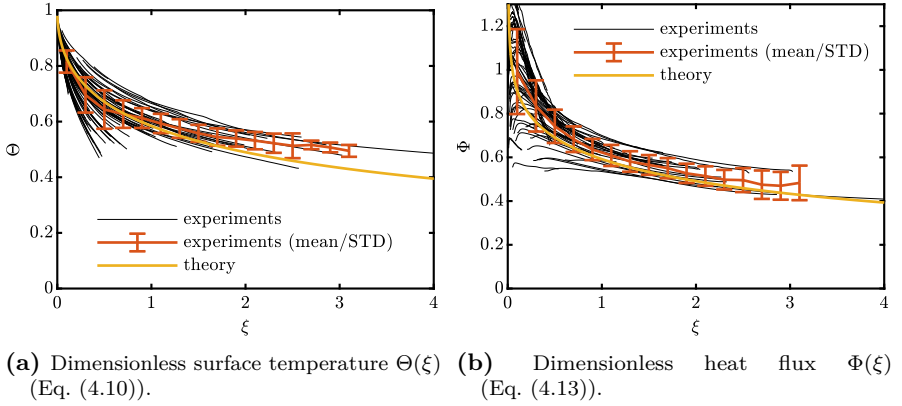


Figure 4.4: Evolution of the dimensionless quantities for the nickel target as a function of the dimensionless time ξ for experimental data in the film boiling regime and for the theoretical solution (Eqs. (4.9) and (4.14)).

by the long duration of the experiments: The longer the experiments last, the larger the thermal boundary layer grows. The higher thermal effusivity supports this increase. Since the developed model is based on the assumption of a semi-infinite substrate; hence, the long duration experiments are no longer covered by the model. Nevertheless, the agreement between experiment and model is still good. In contrast, the dimensionless heat flux is not affected that much by the violation of the semi-infinity of the target. This is because the dependence of the heat flux on the surface temperature (the slope in the film boiling regime in e.g. Fig. 3.3) is rather small for low mass fluxes. Since only the experiments performed with small mass fluxes are the ones that last the longest, the influence of the violated assumption of semi-infinity on the predicted heat flux is rather small.

For pneumatic atomizer For the sake of completeness, Fig. 4.5 shows the comparison between experimental data and theoretical prediction for experiments performed with the nickel target and the pneumatic atomizer. The spray properties of these 5 experiments cover the following narrow range: $\dot{m} = 0.1 - 2.1 \text{ kg/m}^2\text{s}$, $D_{10} = 12 - 24 \text{ }\mu\text{m}$, $U = 12.7 - 20.8 \text{ m/s}$, $T_{w0} = 448 - 450 \text{ }^\circ\text{C}$ and $T_{f0} = 20 - 23 \text{ }^\circ\text{C}$.

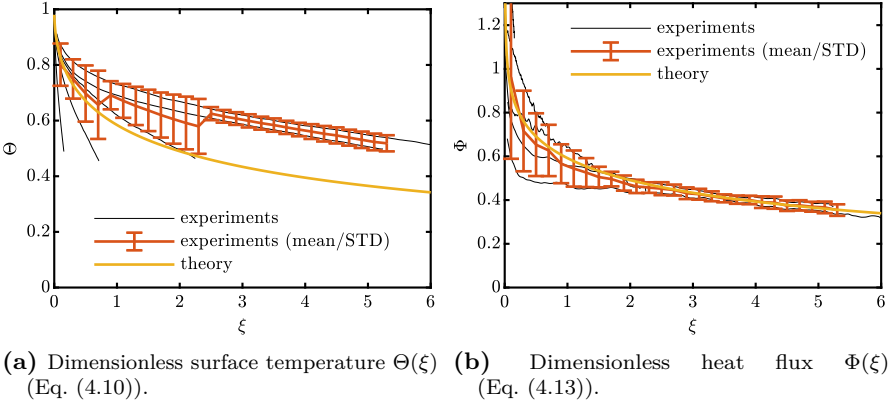


Figure 4.5: Evolution of the dimensionless quantities for the nickel target sprayed with a pneumatic atomizer as a function of the dimensionless time ξ for experimental data in the film boiling regime and for the theoretical solution (Eqs. (4.9) and (4.14)).

Figure 4.5a shows poor agreement between experiments and theoretical prediction of the dimensionless surface temperature. Only a few experiments correspond to the predicted trend. Again, we can explain this by the long duration of the experiments, violating the assumption of semi-infinity. Since most of the experiments in this case have a very low mass flux, the experiments last very long times. In contrast, the agreement of the dimensionless heat flux and its theoretical prediction is again very good.

As previously discussed, the validation of the theoretical prediction against experimental data obtained with various spray parameters and substrate materials clearly indicates the performance of the model. All influences are well captured by the theoretical prediction. The main drawback, that the surface temperature is not well predicted for experiments of long duration, is not too serious: A simple estimation of the thermal conduction inside the substrate can identify in which cases the assumption is valid or not. Nevertheless, the underlying preposition of superimposing single drop impacts in the film boiling regime is still valid. Especially the fact that the parameter χ remains in a very narrow range around ≈ 2 and close to unity, indicates the universality of the model.

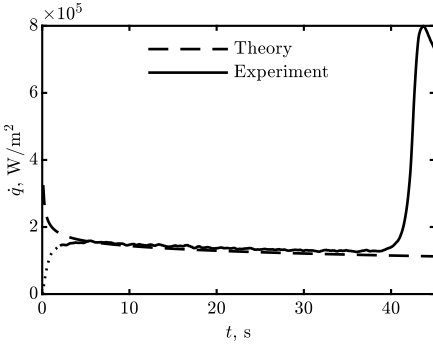
4.4 Application of the model

To better compare theoretical predictions with experimental results, one exemplary case is presented in Fig. 4.6 in dimensional form. The spray parameters for this case are $\dot{m} = 0.9 \text{ kg/m}^2\text{s}$, $D_{10} = 43 \text{ }\mu\text{m}$ and $U = 10 \text{ m/s}$, impacting onto the stainless steel target. These parameters are used in the model (Eqs. (4.9) to (4.14)).

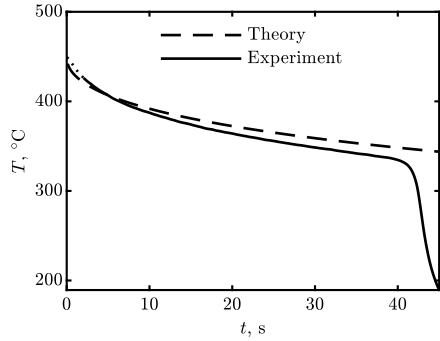
These figures indicate an obviously excellent agreement between experiment and model. Especially the heat flux (Fig. 4.6a) is very well predicted by the model. Slightly larger deviations arise for the surface temperature (Fig. 4.6b). The dotted parts of the experimental curve indicate where the measurements are not valid due to the limited temporal response of the measurement system. The model is not formulated to account for the Leidenfrost effect; hence, the theoretical curve is not valid for $t > 40$.

Examining the initial instants of spray impact (small t in Fig. 4.6a and high T_i in Fig. 4.6c), the theory leads to a better understanding of the process. At the very first instants of the spray impact, the heat flux is very high. Subsequently, it decreases and converges to the well-known linear slope. The very high heat flux in the first instants can be explained by the fact that the first droplets impact onto a substrate having no thermal boundary layer, resulting in an extremely high temperature gradient at the solid-liquid contact interface. With time the thermal boundary layer in the substrate grows and the temperature gradient decrease, leading to a near steady state heat flux.

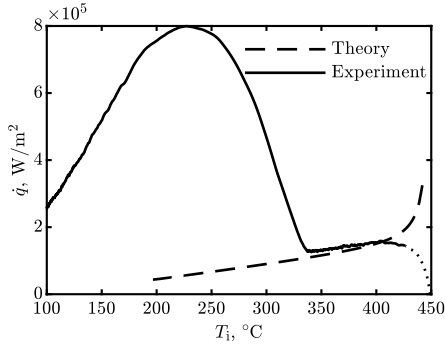
This knowledge is of special interest for pulsed spray cooling, where the spray is continuously switched on and off. During the period when no spray impact occurs, heat flows from the deeper part of the substrate towards the surface and decreases the thermal boundary layer. At the next instant, when the spray is switched on again, spray impact takes place again at a more homogeneously heated surface (compared to the case of continuous spraying). This leads to a heat flux that again starts at a high level. Continuous pulsing of the spray can therefore increase the amount of heat extracted from the substrate while using an overall smaller amount of spray liquid.



(a) Heat flux evolution with time.



(b) Surface temperature evolution with time.



(c) Heat flux as a function of surface temperature.

Figure 4.6: Exemplary comparison between one experiment and the theoretical prediction in the film boiling regime. In a) and b) times are only shown up to shortly after the critical heat flux point is reached.

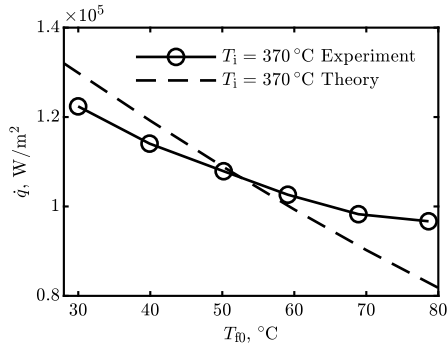


Figure 4.7: Heat flux as a function of the initial spray water temperature. Comparison between experimental data and theoretical prediction. Experimental data is equivalent to those in Fig. 3.17.

Initial spray water temperature In Fig. 4.7 the application of the theoretical prediction for experiments performed with various spray water temperatures T_{f0} is shown. Here the heat flux, evaluated at the surface temperature $T_i = 370^\circ\text{C}$, is plotted as a function of T_{f0} . The experimental data is equivalent to those in Fig. 3.17.

Comparing experiment and theory leads to reasonably good agreement. At low spray temperatures the slope of both lines is comparable. For higher spray temperatures the model predicates a nearly linear decrease of the heat flux, whereas the slope of the experimental data lessens. This deviation can be explained by the following: Since the drops travel some distance between the orifice of the nozzle and the surface, they are affected by the ambient air and they cool down. Warmer drops lose more heat than colder ones, resulting in a higher temperature drop. In the experiments the spray water temperature is measured upstream of the nozzle and therefore differs from the true drop temperature upon impact - the impacting drops are colder than T_{f0} in the experiments. The effect becomes stronger for higher drop temperatures and velocities and for smaller droplets. If this effect was accounted for, the theoretical prediction would correspond better to the experimental results. In conclusion, the theoretical prediction describes well the influence of the spray water temperature on the heat flux.

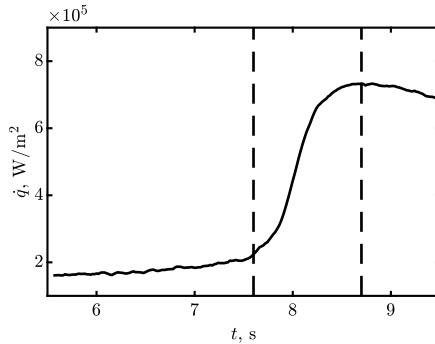


Figure 4.8: Evolution of the heat flux as a function of time for an exemplary experiment. The parameters of the spray are: $\dot{m} = 1.4 \text{ kg/m}^2\text{s}$, $D_{10} = 43 \text{ }\mu\text{m}$ and $U = 11 \text{ m/s}$. The dashed vertical lines bound the transition boiling regime. (Adapted from Tenzer et al. (2019b), with permission of Cambridge University Press. © 2019 Cambridge University Press.)

4.5 Transitional spray cooling regime below the Leidenfrost point

At some instant of time t_L the conditions at the surface correspond to the Leidenfrost point. We identify the Leidenfrost point from the time evolution of the measurement data as the point when the heat flux reaches its minimum in the film boiling regime. The value of the surface temperature corresponding to the Leidenfrost point is not a fixed value and will be discussed in further detail in Chapter 6.

Denote the surface temperature at the Leidenfrost point as T_{iL} . The corresponding heat flux \dot{q}_L can be estimated using Eq. (4.6).

Further cooling leads to a rapid increase of the heat flux, caused by partial wetting of the surface. The area of the wetted patches grows rapidly, promoted by the decreasing surface temperature. The duration of this transitional spray cooling regime is rather short. During this period, two modes of drop impact can be observed: drop impact onto dry regions in the film boiling regime and drop impact onto wetted patches.

In Fig. 4.8 an exemplary dependence of the heat flux on time is shown. Here we limit the temporal span to the time between the end of the film boiling regime and the beginning of the nucleate boiling regime in order to illustrate the behaviour in the transition boiling regime. The corresponding spray parameters are: $\dot{m} = 1.4 \text{ kg/m}^2\text{s}$, $D_{10} = 43 \text{ }\mu\text{m}$ and $U = 11 \text{ m/s}$. We can clearly identify the instant when the Leidenfrost point occurs (t_L), at around 7.6 s, and the instant when the critical heat flux is reached (t_{CHF}), at 8.7 s. This short time of slightly more than 1 s between both events is similar to the rise time of the thermocouples. Therefore, we can obtain no reasonable temperature readings in the range between both events and can make no prediction of the surface temperature and the heat flux in the transition boiling regime or at the critical heat flux.

This short time in the transition boiling regime is very small compared to the overall cooling process and therefore the heat which is transferred during this short time can be neglected. In the present case the transition boiling regime plays no role with respect to the cooling process. Having this short time in mind, we can imagine the transition boiling regime to be non-existent and replaced by a jump of the heat flux towards a very high value at the Leidenfrost point. The typical trend we see in our measurements of heat flux is only due to the limited temporal resolution of the measurement equipment and is probably only valid for very low mass flux or cooling rates in general. The above mentioned time of 1 s is the result of an experiment having a small mass flux. Typical experiments having a higher mass flux lead to even smaller times, which support the previously described understanding of the transition boiling regime in our experiments.

5 Heat transfer in nucleate boiling regime

This chapter describes the development and application of a model for the heat flux in the nucleate boiling regime. First, the underlying assumptions of the model are presented, followed by the formulation, validation and exemplary application of the model. Initially the model was developed for the stainless steel target; however, other target materials are also taken into account.

Parts of this chapter have already been published in Tenzer et al. (2019b).

5.1 Modelling heat flux as a remote asymptotic solution

For longer times $t > t_L$, during the nucleate boiling regime of spray cooling, the heat flux can be estimated from Eq. (4.4) accounting for the very short duration of the transient boiling regime and the very high time derivation of temperature during this regime. Denote ΔT_L as the temperature jump during the transition boiling. In this case Eq. (4.4) yields

$$\dot{q}(t) = -\frac{\epsilon_w}{\sqrt{\pi}} \int_0^{t_L} \frac{T'_{i,\text{film}}(\tau)}{\sqrt{t-\tau}} d\tau + \frac{\epsilon_w}{\sqrt{\pi}} \frac{\Delta T_L}{\sqrt{t-t_L}} - \frac{\epsilon_w}{\sqrt{\pi}} \int_{t_L}^t \frac{T'_{i,\text{nucleate}}(\tau)}{\sqrt{t-\tau}} d\tau. \quad (5.1)$$

On the right-hand side of Eq. (5.1) the first term is associated with the thermal history during the film boiling regime, the second term is associated with the temperature jump ΔT_L during the transition regime at $\tau = t_L$, and the last term is based on the temperature evolution during the nucleate boiling at times $t_L < \tau < t$.

In order to model the heat flux in the nucleate boiling regime the values of ΔT_L and the evolution of the surface temperature $T_i(\tau)$ (which is required for the computation of the time derivative $T'_i(\tau)$) are necessary.

In the estimation of an upper bound for heat flux during the nucleate boiling regime of single drop impact the temperature at the wetted part of the wall interface is approximated by the saturation temperature T_{sat} (Breitenbach et al., 2017a).

The nucleate boiling regime is characterized by intensive nucleation and expansion of vapor bubbles. The temperature in the vicinity of the contact line of the each expanding bubble is close to the saturation temperature. However, some overheating of the surrounding liquid is required for the bubble growth. The heat transfer in the liquid phase during the nucleate boiling regime is governed by the convection in the liquid flow between the bubbles. The heat mainly goes into vaporization at the bubble interfaces where $T = T_{\text{sat}}$. Therefore, the upper bound for the heat flux during nucleate boiling regime can be estimated invoking the assumption that the temperature at the wetted wall interface is T_{sat} . Using this rough estimation of \dot{q} the predicted duration of a single drop evaporation in the nucleate boiling regime agrees very well with numerous experimental data (Abu-Zaid, 2003; Itaru & Kunihide, 1978; Tartarini et al., 1999).

In this study the upper bound for the heat flux \dot{q} during spray cooling is also estimated, as in the case of a single drop impact, using the assumption that the substrate temperature is equal to the saturation temperature at $t > t_L$. The third term on the right-hand side of Eq. (5.1), associated with the time gradient of the surface temperature at $t > t_L$, can be neglected in comparison to the effect of the temperature jump at the Leidenfrost point. The temperature jump during the transition boiling regime can be estimated as $\Delta T_L = T_{iL} - T_{\text{sat}}$.

The heat flux can be obtained from Eq. (5.1), neglecting the value of the last term, in the form

$$\dot{q} = \frac{\epsilon_w}{\sqrt{\pi}} \frac{T_{iL} - T_{\text{sat}}}{\sqrt{t - t_L}} - S\epsilon_w \frac{T_{w0} - T_{\text{sat}}}{2} \sum_{i=1}^{\infty} a_i i B \left[\frac{\xi_L}{\xi}; \frac{i}{2}, \frac{1}{2} \right] \xi^{\frac{i-1}{2}}, \quad (5.2)$$

where $B[\cdot; \cdot, \cdot]$ is the incomplete beta function. Equation (5.2) is valid only for very fast substrate cooling, when the time interval between the Leidenfrost point and the point corresponding to the critical heat flux is very short. It

can be further modified using Eq. (4.10)

$$\dot{q} = \frac{\epsilon_w}{\sqrt{\pi}} \frac{T_{w0} - T_{\text{sat}}}{\sqrt{t - t_L}} \left[\Theta(\xi_L) - \frac{S\sqrt{\pi}\sqrt{t - t_L}}{2} \sum_{i=1}^{\infty} a_i i \text{B} \left[\frac{\xi_L}{\xi}; \frac{i}{2}, \frac{1}{2} \right] \xi^{\frac{i-1}{2}} \right]. \quad (5.3)$$

Moreover, at large times, $t \gg t_L$, Eq. (5.3) approaches the following remote asymptotic solution

$$\dot{q} \approx \frac{\epsilon_w}{\sqrt{\pi}} \frac{T_{w0} - T_{\text{sat}}}{\sqrt{t - t_L}} \left[\Theta(\xi_L) + \frac{2S\sqrt{t_L}}{\sqrt{\pi}} \right]. \quad (5.4)$$

Rearranging Eq. (5.4) leads to

$$\mathcal{T} \equiv k \frac{\epsilon_w^2 \Delta T^2}{\pi \dot{q}(t)^2} \approx t - t_L, \quad (5.5)$$

where k is a constant which can be determined from the experiments and $\Delta T = T_{w0} - T_{\text{sat}}$.

5.2 Model validation

Stainless steel target In Fig. 5.1 the values of the term $\mathcal{T} = k\epsilon_w^2 \Delta T^2 / \pi \dot{q}^2$, measured for various spray parameters and different initial substrate temperatures, are shown as a function of $t - t_L$. The constant $k = 1.05$ is determined for all the sets of the operational parameters to best fit the theory. The parameters of the 86 experiments used in the plotting of the data in Fig. 5.1 are varied over wide ranges: mass flux \dot{m} from 0.5 to 29.5 kg/m²s, average drop diameter D_{10} from 43 to 78 μm , average impact velocity U from 6.7 to 17.7 m/s, initial wall temperature T_{w0} from 350 to 450 °C and spray fluid temperature T_{f0} from 18 to 80 °C. Additionally, a line corresponding to the average value of \mathcal{T} for all the experiments and the error bars indicating one standard deviation are shown in the graph.

We can identify an excellent agreement between theoretical prediction and experimental data over a broad range of spray parameters. As predicted by the remote asymptotic solution (Eq. (5.5)), the term \mathcal{T} is very close to the time increment $t - t_L$ in all the experiments.

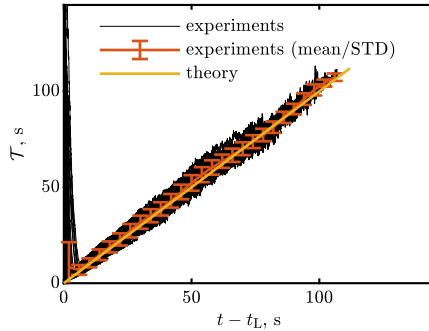


Figure 5.1: Scaling of the heat flux, expressed through \mathcal{T} defined in Eq. (5.5), plotted as a function of time for the stainless steel target. The straight line has a slope of unity and indicates good agreement between the theory and the experimental data. (Adapted from Tenzer et al. (2019b), with permission of Cambridge University Press. © 2019 Cambridge University Press.)

Hot-work tool steel target Similarly, Fig. 5.2 shows the comparison between theoretical prediction and experiential data for the target built of hot-work tool steel. The spray properties of these 6 experiments cover the following narrow range: $\dot{m} = 1.1 - 4.6 \text{ kg/m}^2\text{s}$, $D_{10} = 43 - 79 \text{ }\mu\text{m}$, $U = 7.8 - 14.3 \text{ m/s}$, $T_{w0} = 410 - 449 \text{ }^\circ\text{C}$ and $T_{f0} = 19 - 21 \text{ }^\circ\text{C}$.

The constant $k = 1.05$ is the same as in the previous case of the stainless steel target. Again we can identify very good agreement between theoretical prediction and experimental data for larger times, when the critical heat flux has been passed.

Nickel target In Fig. 5.3a the same comparison is shown for the target built of nickel. The spray properties of these 59 experiments span the following ranges: $\dot{m} = 0.6 - 30.3 \text{ kg/m}^2\text{s}$, $D_{10} = 43 - 114 \text{ }\mu\text{m}$, $U = 5.1 - 22.5 \text{ m/s}$, $T_{w0} = 300 - 462 \text{ }^\circ\text{C}$ and $T_{f0} = 18 - 23 \text{ }^\circ\text{C}$. In contrast to the other materials, we identify good agreement between theory and experimental data only for small times $t < 20 \text{ s}$. At larger times the experiments differ from the theoretical prediction. This can be explained by the thermal boundary layer inside the substrate. Since the thermal diffusivity of nickel is significantly larger than those of stainless steel and hot-work tool steel, the thermal boundary layer grows much faster for experiments performed with nickel. At some instant

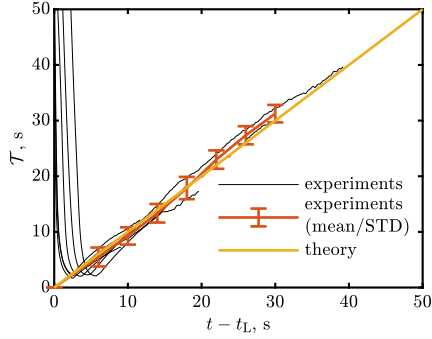


Figure 5.2: Scaling of the heat flux, expressed through \mathcal{T} , defined in Eq. (5.5), plotted as a function of time for the target built of hot-work tool steel.

the boundary layer reaches the bottom of the target and the assumption of semi-infinity is violated. Therefore the theory (Eq. (5.5)) is no longer valid and experimental data and theoretical predictions differ.

In Fig. 5.3b we show only those experiments where the assumption of semi-infinity is justifiable. If the temperature difference at the bottom between the beginning and the end of the experiment is larger than 30°C , the experiments are treated as significantly not semi-infinite and are not included in Fig. 5.3b. It turns out that this constraint leads to basically the same amount of experimental data that spans across the same temporal range ($t < 20\text{ s}$) as observed in Fig. 5.3a.

Finally, we observe good agreement between experimental data and theoretical predictions as long as the assumption of semi-infinity is valid. Our experiments show that the heat flux in the fully developed nucleate boiling regime depends significantly on time. It is estimated as

$$\dot{q} \approx \frac{\epsilon_w}{\sqrt{\pi}} \frac{T_{w0} - T_{\text{sat}}}{\sqrt{t - t_L}}. \quad (5.6)$$

Note that the measured values for \mathcal{T} deviate significantly from the theoretical predictions at small times, associated with the film boiling and transition regimes, for which the scaling (Eq. (5.5)) is not applicable.

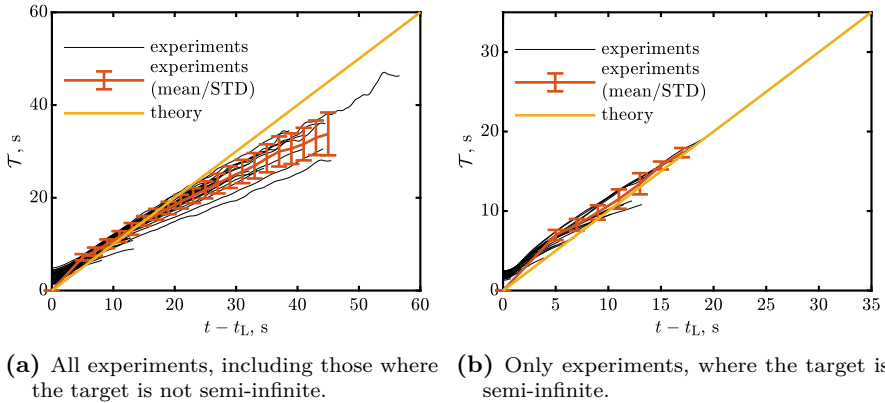


Figure 5.3: Scaling of the heat flux, expressed through \mathcal{T} defined in Eq. (5.5), plotted as a function of time for the nickel target.

The remote asymptotic solution (Eq. (5.6)) is valid only for a semi-infinite hot substrate and uniform spray. In practice this means that the thickness and the width of the substrate are larger than the thickness of the thermal boundary layer in the substrate $\sqrt{\alpha t}$.

5.3 Heat flux and its upper boundary

The measured heat flux during nucleate boiling regime is described very well by the upper boundary estimation (Eq. (5.6)) obtained from the assumption that the interface temperature is equal to T_{sat} . The reason for this agreement is not immediately clear since some liquid overhear is expected during the nucleate boiling.

This interesting result can be explained by the fact that the interface temperature oscillates due to the nucleation of multiple bubbles, their expansion and subsequent collapse (Carey, 2018). The bubble contact lines of the wall-bounded bubbles, whose temperatures are close to T_{sat} , quickly propagate along the interface. The characteristic time of bubble formation t_{bubble} in the experiments is approximately 1 ms (Breitenbach et al., 2017a). Therefore, the thickness of the thermal boundary layer associated with a single bubble

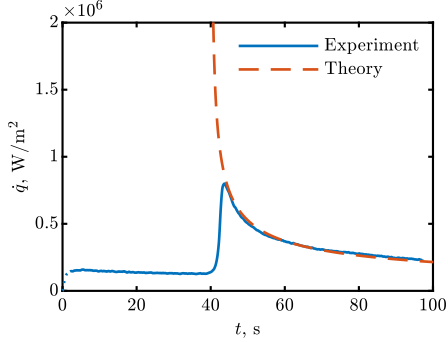


Figure 5.4: Exemplary comparison between one experiment and the theoretical prediction in the nucleate boiling regime (Eq. (5.6)). Heat flux evolution with time.

event is $h_{\text{bubble}} \sim \sqrt{\alpha_w t_{\text{bubble}}}$. This value is approximately $70 \mu\text{m}$ in our case. In any case, our measurement system is not able to detect such rapid temperature fluctuations.

At any given location on the wall surface the temperature jumps to the saturation temperature each time the contact line propagates through this position. Our measurements allow estimation of only the averaged value of the temperature fluctuations above the saturation temperature. Nevertheless, the contribution of the temperature fluctuations (consisting of positive and negative jumps above T_{sat}) to the time averaged heat flux \dot{q} is negligibly small.

5.4 Application of the model

To better compare the theoretical predictions with experimental results, one exemplary case is shown in Fig. 5.4 in dimensional form. The experiment corresponds to that in Section 4.4, but this time we focus on the nucleate boiling regime. Accordingly, the spray parameters for this case are $\dot{m} = 0.9 \text{ kg/m}^2\text{s}$, $D_{10} = 43 \mu\text{m}$ and $U = 10 \text{ m/s}$.

The dashed line representing the theoretical prediction is calculated using Eq. (5.6). For clarification it is mentioned that the Leidenfrost point and time when it occurs t_L is taken from the experimental data. In the present case $t_L = 40 \text{ s}$.

Although the curve shows the entire experiment, the theoretical prediction is only valid after the Leidenfrost point is passed. This range corresponds to $t > t_L = 40$ s. At these first instants the predicted heat flux starts at infinity and strongly decreases. The agreement between experiment and model is obviously not good in this interval. Keeping in mind the limited temporal resolution of the measurement system, the disagreement is not unexpected. A few instants later, roughly at the critical heat flux (maximum heat flux), the prediction matches almost perfectly the experimental data. The excellent agreement persists until the end of the experiment.

In summary, we find excellent agreement between experiment and theoretical prediction (Eq. (5.6)) after the first instants. Furthermore, the very good agreement leads to a new understanding of the heat transfer in the nucleate boiling regime during transient spray cooling: The heat flux is limited by the thermal effusivity ϵ_w of the substrate and the initial wall temperature T_{w0} . It depends on time. There is no or only a very weak dependence of the heat flux on the spray properties. In other words, the heat flux is limited by the thermal inertia of the material. This means that there is no possibility to influence the heat transfer in the nucleate boiling regime with different spray properties. Even the smallest mass flux of all our experiments is sufficiently large enough to lead to this state of saturation where the material limits the heat flux even if the spray could lead to a higher one.

The complete heat flux dependence on time for the entire experiment is calculated by combining the heat fluxes predicted by the models for both regimes (Eqs. (4.9) to (4.14) and (5.6)) as

$$\dot{q}_S(t) = \begin{cases} S\epsilon_w(T_{w0} - T_{\text{sat}})\Phi(\xi) & \text{for } t < t_L \\ \frac{\epsilon_w}{\sqrt{\pi}} \frac{T_{w0} - T_{\text{sat}}}{\sqrt{t - t_L}} & \text{for } t > t_L. \end{cases} \quad (5.7)$$

As described and justified in Section 4.5 the transition boiling regime is skipped and replaced by a jump at the Leidenfrost point. Again, the only necessary addition information is $t_L = 40$ s, which is taken from the experiments. For the sake of completeness, the temporal evolution of the resulting overall heat flux expressed by Eq. (5.7) is shown in Fig. 5.5. Obviously, the heat flux in the transition boiling regime is strongly over-estimated due to replacing this regime with a jump. From the experimental point of view we are not able to confirm or disprove whether this jump is reasonable or in which way the

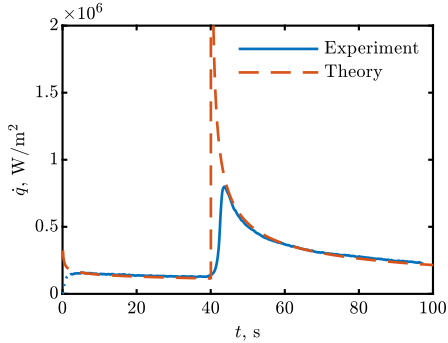


Figure 5.5: Exemplary comparison between one experiment and the theoretical prediction of the entire cooling process (Eq. (5.7)). Heat flux evolution with time.

jump is attenuated. Since the Leidenfrost point corresponds to the onset of remaining wetting, we can assume a change of the entire physics governing heat transfer. Furthermore, the visual observations in Section 3.2 show that the transition boiling regime exhibits the beginning of the formation of a closed liquid film at the surface. Both are consistent with a jump of the heat flux. Nevertheless, it is obvious that the formation of the liquid film is not an instantaneous event and instead takes some time. The duration is longer for lower mass fluxes, since the lower mass flux leads to longer times until the liquid film is formed. Therefore, the agreement between prediction of the overall heat flux (Eq. (5.7)) and experiment can be expected to improve with increasing mass flux.

For higher cooling efficiency, the independence of the heat flux on the spray parameters suggests a cooling process that consists of two stages: Spraying with high mass fluxes in the film boiling regime to reach a maximum heat flux. Subsequently, switching to a lower mass flux in the nucleate boiling regime, reduces the necessary spray fluid while maintaining the heat flux, since it is no longer influenced by the spray properties.

6 Leidenfrost point

The Leidenfrost point corresponds to the instant when the minimum heat flux is reached and afterwards strongly increases. For this reason it is of major interest to reliably predict this point in any spray cooling process. Moreover, it is the last remaining part of the boiling curve which has yet to be described to finally predict the heat flux during the entire spray cooling process.

The following chapter is dedicated to a better understanding of the Leidenfrost point. In the first part the experiential results of this study are analyzed to identify any possible dependence on the various spray parameters. Subsequently, our results are compared to published predictions in literature. Finally we identify the dependence on the substrate and derive a new understanding and universal prediction for the Leidenfrost point.

Parts of this chapter have already appeared in Tenzer et al. (2020).

6.1 Influences on the Leidenfrost point

The visual observations in Section 3.2 indicate that the Leidenfrost point corresponds closely to the first instants in which fluid remains on the surface. At temperatures higher than the Leidenfrost temperature, no sessile drops or wetted patches are observed on the surface. When the surface temperature is slightly lower, the amount of liquid remaining on the surface immediately after the drop impact begins to increase. This trend continues for even lower temperatures: the amount of remaining liquid rises and larger patches of liquid form, as shown in Fig. 3.16.

The experimental data of this study span a large parameter range. This allows quantitative investigation of the Leidenfrost point and its influencing parameters. The Leidenfrost point and its temperature is determined for each experiment, where film boiling can be clearly identified by the minimum heat flux. Figure 6.1 illustrates this procedure, where q_{\min} is the minimum heat flux and T_L the Leidenfrost temperature. These experiments are characterized

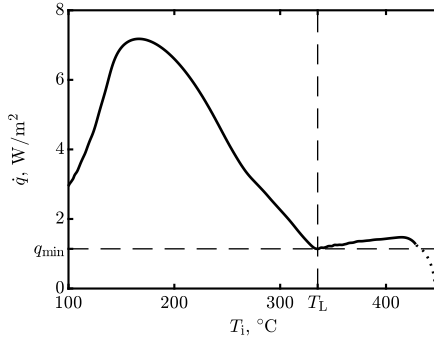


Figure 6.1: Determination of the Leidenfrost point T_L as the temperature at the minimum heat flux q_{\min} .

by a typical linear increasing heat flux in the film boiling regime. Other experiments not showing this behavior are discarded, since in these cases the cooling is too intensive and the timescales are too short to be properly captured by the thermocouples. Although the linear slope is also present in these discarded experiments, it cannot be detected by the measurement technique, as previously discussed in Section 3.3.1.

Even though the literature survey in Section 1.2 reveals no clear picture of the dependencies of the Leidenfrost point, there is general agreement that the mass flux plays an important role. To check whether this influence is present in our experimental data Fig. 6.2 shows the Leidenfrost temperature T_L as a function of the local mass flux \dot{m} . Here the different materials of the target, stainless steel and nickel, are indicated by different markers and colors. Since only a few experiments were performed with hot-work tool steel, these results are not shown here and in the following discussion. Although the data scatters a lot, there is no dependence of the Leidenfrost temperature on the mass flux for both materials. This clearly becomes apparent from the experiments performed with nickel. For the very large range of mass fluxes the Leidenfrost temperature remains constant. Due to high cooling rate in the experiments performed with stainless steel, the data only spans a narrow range of mass flux. But even in this case no influence is visible. Compared to literature we detect no influence of the mass flux on the Leidenfrost temperature. Additionally,

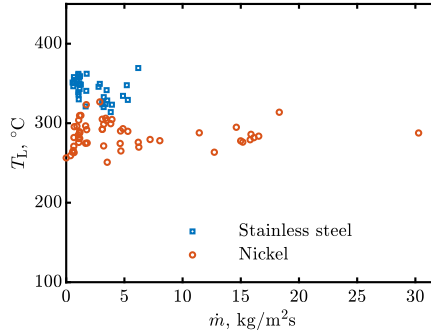


Figure 6.2: Leidenfrost temperature T_L as a function of the mass flux \dot{m} . (as can be read in Tenzer et al. (2020).)

the Leidenfrost temperature is higher for stainless steel than for nickel. This leads to the assumption that the Leidenfrost point is dependent on the target material.

The observations in Section 3.2 and the modeling in the film boiling regime in Chapter 4 have shown that spray impact in the film boiling regime consists of a superposition of single drop impacts. Since the Leidenfrost point temporally follows the film boiling regime and starts to take place during this regime, we can assume that the Leidenfrost point is connected to the impact of a single drop.

To check this assumption Fig. 6.3 shows the dependence of the Leidenfrost temperature on the spray properties: mean drop diameter D_{10} in Fig. 6.3a and mean drop velocity U in Fig. 6.3b. In both cases no dependence can be observed. Despite the scatter, the Leidenfrost temperature is constant and independent of the mean drop diameter or mean drop velocity of the spray. The shown data also includes the experiments performed with the pneumatic atomizer. Due to the smallest drop diameter of $\approx 20\ \mu\text{m}$, these points are clearly visible in Fig. 6.3a. In this case the Leidenfrost temperature is also constant and comparable to the other experiments. It is remarkable that even for sprays produced by different principles of atomization, the Leidenfrost temperature is constant.

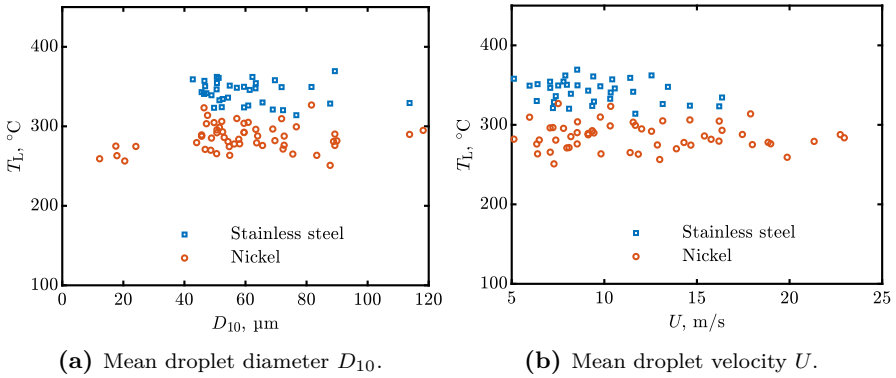


Figure 6.3: Dependence of the Leidenfrost temperature T_L on the spray properties. (as can be read in Tenzer et al. (2020).)

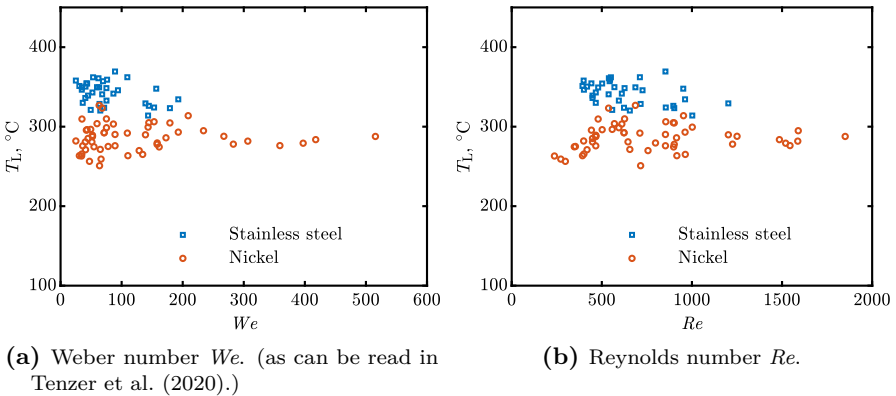


Figure 6.4: Dependence of the Leidenfrost temperature T_L on dimensionless numbers.

Furthermore, the influence of two combinations of these quantities are presented as dimensionless numbers: the single drop Weber number We in Fig. 6.4a and the single drop Reynolds number Re in Fig. 6.4b, both defined in Section 2.2.3. In both cases there is again no dependence of the Leidenfrost point on the Weber number or the Reynolds number. The lowest Weber number of the experiments is $We_{\min} = 25$. The literature survey in Section 1.2 showed an influence of the Weber number on the Leidenfrost temperature during single drop impact. This dependence shows an asymptotic behavior towards large Weber numbers: The influence is large for small Weber numbers and becomes very small for large ones. The independent and constant Leidenfrost temperature in Fig. 6.4a indicates, that $We_{\min} = 25$ of this experiments is already sufficiently large enough and in the asymptotic range. Thus, the Weber number has no identifiable influence on the Leidenfrost temperature anymore.

Following the previous discussion, we conclude that there is no influence of any spray parameter on the Leidenfrost temperature, which is in strong contrast to the findings in literature. Except for some small scatter the temperature at the Leidenfrost point is constant in our study. This scatter can be explained by the inhomogeneity of the spray: The atomization process of a conventional atomizer is not perfectly uniform due to mechanical tolerances and imperfections. Therefore larger drops or even large non-spherical ligaments occur randomly. These non-uniformities of the spray result in a strong local and non-homogeneous heat flux which influences the local wetting behavior at the surface. The randomness of this process is not captured by the spray characterization or by the two-dimensional heat flux calculation. Thus, their effect is not visible in the previously discussed dependencies of the Leidenfrost point in Figs. 6.2 to 6.4. Instead, this is likely the explanation for the observed scatter of the observed Leidenfrost temperature.

6.2 Comparison with literature

As already discussed in Section 1.2 there exist only a few models to describe or predict the Leidenfrost point. In the following section our results are compared to those models or correlations found in literature that are explicitly meant for sprays.

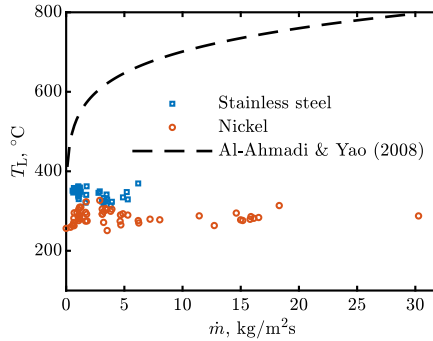


Figure 6.5: Comparison between own data and the correlation proposed by Al-Ahmadi & Yao (2008) (Eq. (1.2)).

Figure 6.5 shows the experimental data of this study in comparison to the correlation proposed by Al-Ahmadi & Yao (2008) which presumes an influence of the mass flux (Eq. (1.2)). As discussed before, the data of this study shows no influence of the mass flux on the Leidenfrost temperature. Therefore there is obviously no agreement between our experiments and the proposed correlation. Instead the correlation strongly over-predicts the Leidenfrost temperature of up to 800 °C.

In Fig. 6.6 the experimental data of this thesis is compared to the model proposed by Bernardin & Mudawar (2004) (Eq. (1.6)). This model predicts an influence of the droplet velocity. As can be seen, the Leidenfrost temperature predicted by the model and the experimental data span approximately the same range. But again, the experimental data show no influence of the droplet velocity. In contrast the model forecasts that the Leidenfrost temperature increases with an increasing droplet velocity. We can identify no agreement between prediction and our experimental data.

As already shown in Section 1.2, Yao & Cox (2002) plotted the experimental data of various researchers (Yao & Choi, 1987; Choi & Yao, 1987; Hoogendoorn & den Hond, 1974; Mizikar, 1970; Ito et al., 1991; Shoji et al., 1984; Cox & Yao, 1999) as a function of the spray Weber number We_s . They assumed that the Leidenfrost temperature depends on We_s and fitted a correlation resulting in Eq. (1.5). Figure 6.7 shows an adaption of their original illustration. To provide a good comparison to the original illustration, the logarithmic axes

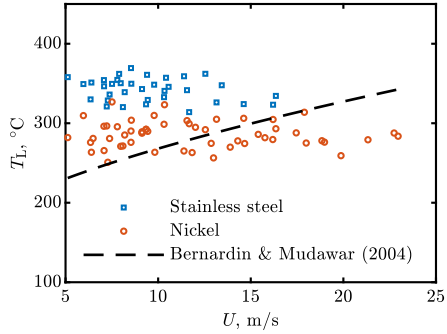


Figure 6.6: Comparison between own data and the correlation proposed by Bernardin & Mudawar (2004) (Eq. (1.6)).

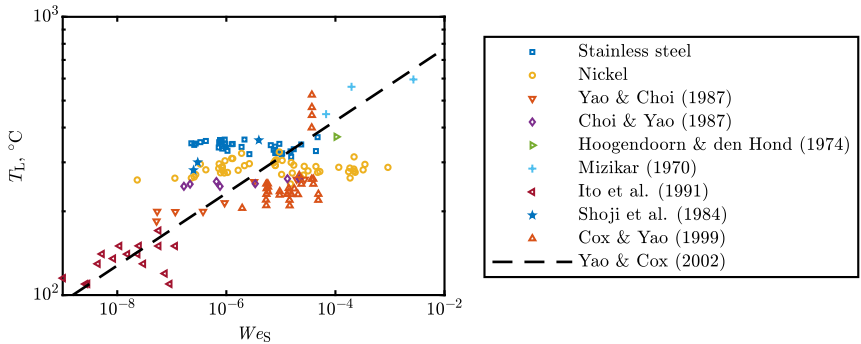


Figure 6.7: Comparison between own data, those of other researchers and the correlation proposed by Yao & Cox (2002) (Eq. (1.5)). (Adapted from Yao & Cox (2002), with permission of Taylor & Francis. © 2002 Taylor & Francis.)

and their scale are kept the same. In addition the experimental data of the present study is added. The correlation seems to fit quite well to the ensemble of all data. Taking a closer look at the individual data sets of each group, the agreement is however much worse. Especially the data of this study (stainless steel and nickel), is not well described by their correlation. Instead, the data presented from each study could be considered as being approximately constant and independent of the spray Weber number.

In summary, there is no agreement between models and empirical correlations published in the literature and the data of this study. All publications maintain that the Leidenfrost temperature is significantly influenced by spray properties. This assertion cannot be corroborated by the data from the present study, in fact the present results indicates that the Leidenfrost temperature is independent of any spray property.

6.3 Theoretical prediction of the Leidenfrost point

The previous discussion of the experimental results has shown that the Leidenfrost point is independent of the spray properties. In contrast it is influenced by the substrate material.

This leads to the central question: *What happens at the Leidenfrost point?* This question is first pursued by examining possible mechanisms for stabilizing the vapor-liquid interface occurring in the film boiling condition. These mechanisms are sketched in Fig. 6.8. One mechanism is the enhancement of vaporization in the thinner regions of the vapor layer due to the higher heat flux there, as shown schematically in Fig. 6.8a. Such a mechanism counteracts the Rayleigh-Taylor instability. Thus, the transition to the nucleate boiling regime is not possible, since the heat flux, and thus the evaporation rate, become infinite as soon as the vapor layer thickness tends to zero.

Another potential reason for instability of the film boiling regime could be the homogeneous nucleation which is initiated in the liquid at a certain temperature (Avedisian, 1985), as illustrated in Fig. 6.8b. This assumption has been used in models for the Leidenfrost temperature (Wang et al., 2019b; Bjornard & Griffith, 1977; Wang et al., 2019a), in particular, for the explanation of the dependence of the Leidenfrost temperature on the thermal effusivity of

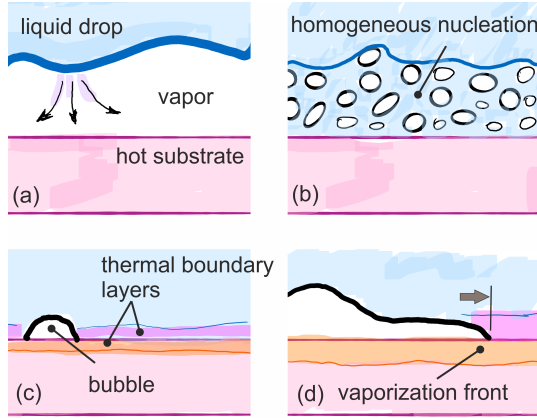


Figure 6.8: Possible mechanisms of film boiling: (a) stabilization of a liquid-vapor interface by the vapor generation and (b) homogeneous nucleation at a certain temperature. A single bubble (c) can also expand along the substrate due to strong vaporization at the contact line (d). (as can be read in Tenzer et al. (2020).)

the target material. The estimated homogeneous nucleation temperature is $T_h = 306^\circ\text{C}$, computed from the data for the Leidenfrost temperature (Wang et al., 2019a). Another estimation (Avedisian, 1985) for the homogeneous nucleation temperature is $T_h = 202^\circ\text{C}$. However this assumption contradicts the observations of film boiling below T_h on substrates with very high thermal effusivity, where the Leidenfrost point approaches the saturation temperature.

To confirm the appearance of low Leidenfrost temperatures, we performed a simple experiment by placing a sessile water drop on a polished copper surface at various substrate temperatures T_i . The exemplary outcomes are shown in Fig. 6.9. In Fig. 6.9b at $T_i = 138^\circ\text{C}$ we can clearly identify Leidenfrost phenomena: The drop is separated from the surface by a vapor layer. The lifetime of the drop is very high. At a lower surface temperature of $T_i = 124^\circ\text{C}$ in Fig. 6.9b the drop immediately starts to evaporate after first contact with the surface. Extensive nucleation and formation of secondary droplets is visible. We were able to identify Leidenfrost behavior at temperatures $T_i > 125^\circ\text{C}$. Therefore the measured Leidenfrost temperature for water drops on copper targets is 124°C for a sessile drop or 134°C for impacting drops in

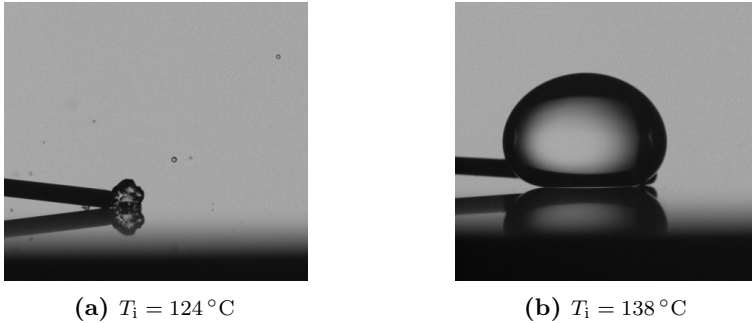


Figure 6.9: A sessile drop on a heated copper surface at different surface temperatures T_i .

a spray (Ito et al., 1991), which are both lower than the limit for superheat of distilled water. Moreover, neither of these hypotheses can explain the observed significant influence of nano-structures, surface morphology or wettability of the substrate on the Leidenfrost temperature, (Auliano et al., 2016; Kruse et al., 2013; Romashevskiy et al., 2016; Kim et al., 2012; Takata et al., 2005).

Consider however the first stage of heat transfer, just after the contact of the liquid with the solid substrate. In the nucleate boiling regime the contact is followed by the emergence of numerous bubbles on the solid substrate as a result of heterogeneous nucleation. The heat transfer can be described by the heat conduction in two expanding thermal boundary layers in the liquid and the substrate respectively. The thickness of the thermal boundary layer is $h_w \sim \sqrt{\alpha_w t}$ where α_w is the thermal diffusivity of the corresponding material, liquid or solid. This phenomenon is depicted schematically in Fig. 6.8c.

The typical heat flux at the solid-liquid interface in the nucleate boiling regime is determined by the thickness of the boundary layer in the solid substrate and by the fact that the temperature of the vapor bubble interface is close to the saturation temperature T_{sat}

$$\dot{q} \sim \frac{\epsilon_w(T_{w0} - T_{\text{sat}})}{\sqrt{t}}, \quad (6.1)$$

where T_{w0} is the initial substrate temperature prior to contact with the liquid and ϵ_w is the thermal effusivity of the wall material. Equation (6.1) has been recently validated by comparison with the experimental data for single drops (Breitenbach et al., 2017a) and sprays (Tenzer et al., 2019b).

At some elevated wall temperature, characterized by intensive heating, vaporization fronts appear instead of local bubbles and expand along the substrate with a certain velocity. For a high enough velocity, the front leads to the formation of a thin, near-wall vapor layer (as shown in the sketch in Fig. 6.8d). The propagation velocity of the vaporization front, depending on the heating rate and liquid properties, can be constant (Okuyama et al., 2006; Avksentyuk & Ovchinnikov, 2000; Stutz & Simões-Moreira, 2013; Aktershev & Ovchinnikov, 2011) or can grow exponentially (Staszal & Yarin, 2018) in time.

We can roughly estimate the characteristic velocity $U_v \sim \dot{q}/\rho_f L$ of the vaporization front using Eq. (6.1)

$$U_v \sim \frac{\epsilon_w(T_{w0} - T_{\text{sat}})}{\rho_f L \sqrt{t}}, \quad (6.2)$$

where L is the latent heat of evaporation and ρ_f is the density of the liquid. A similar approach has been successfully used to predict the velocities of secondary drops in the thermal atomization regime (Breitenbach et al., 2018a; Roisman et al., 2018).

The only available characteristic thickness in the liquid region associated with the vaporization front is the thickness of the thermal boundary layer in the fluid $h_f \sim \sqrt{\alpha_f t}$, where α_f is the thermal diffusivity of the fluid. Therefore, the Weber and the capillary numbers based on the typical vaporization front velocity (Eq. (6.2)) are singular at $t \rightarrow 0$, which means the influence of surface tension on the formation of the vaporization front is initially negligibly small. The Reynolds number $Re_v = \rho_f h_f U_v / \nu_f$, in contrast, is finite

$$Re_v = \frac{\epsilon_w \sqrt{\alpha_f} (T_{w0} - T_{\text{sat}})}{\nu_f L}. \quad (6.3)$$

The viscous stresses therefore play an important role during the entire process of the vaporization front formation. The characteristic superheat ΔT^* at which the inertia and viscous terms are comparable can be determined assuming

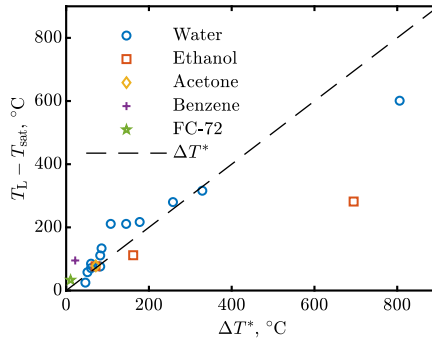


Figure 6.10: Substrate superheat at the Leidenfrost point, $T_L - T_{\text{sat}}$, as a function of ΔT^* for sessile drops. The data for different liquids, from this study and from Baumeister & Simon (1973); Bernardin & Mudawar (1999); Emmerson (1975); Wachters et al. (1966); Wang et al. (2019a), are listed in Table 6.1. (as can be read in Tenzer et al. (2020).)

$Re_v = 1$ in Eq. (6.3)

$$\Delta T^* = \frac{\nu_f L}{\epsilon_w \sqrt{\alpha_f}} \quad (6.4)$$

In Fig. 6.10 the experimental data for $T_L - T_{\text{sat}}$ of sessile drops of different liquids on various substrates is shown as a function of ΔT^* . The liquid properties for calculation of ΔT^* are taken at the saturation temperature.

For data taken from the literature, the substrate materials and their thermal properties, type of experiment and the resulting Leidenfrost temperature are summarized in Table 6.1. The thermal properties of the designated substrate materials are taken from general literature and handbooks. Since these properties are temperature dependent, they have been calculated at the corresponding Leidenfrost temperature. In all cited studies the surface is polished. Since the spray or drop impact occurs at the surface, the thermal properties of the plating material is used in the case of a plated substrate, (Yao & Choi, 1987; Choi & Yao, 1987; Yao & Cox, 2002; Bernardin et al., 1997). Data from Wang et al. (2019a) were measured for different Weber numbers: those with a large We were treated as spray data, whereas those with a small We is treated as sessile drops.

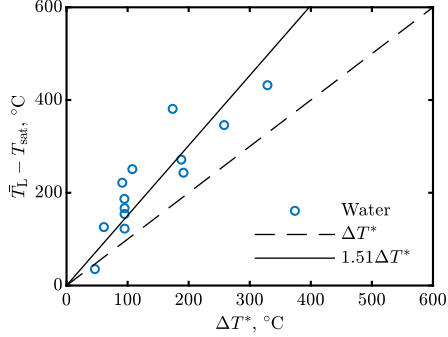


Figure 6.11: Mean substrate superheat at the Leidenfrost point $\bar{T}_L - T_{\text{sat}}$ as a function of ΔT^* for spray cooling. The data for distilled water from this study and from Hoogendoorn & den Hond (1974); Shoji et al. (1984); Ito et al. (1991); Yao & Choi (1987); Choi & Yao (1987); Yao & Cox (2002); Bernardin et al. (1997); Tran et al. (2012); Wang et al. (2019a) are listed in Table 6.1. (as can be read in Tenzer et al. (2020).)

It seems that for a wide range of targets the value of $T_L - T_{\text{sat}}$ can be predicted rather well as $T_L - T_{\text{sat}} = \Delta T^*$. For wall materials with very low thermal effusivity the values for the Leidenfrost temperature deviate significantly from the prediction. In both cases, for water and for ethanol, the measured wall temperatures are above the critical temperature. In this case additional physics has to be accounted for.

The corresponding data for spray impact or high Weber number drop impact are shown in Fig. 6.11. The superheat associated with the Leidenfrost temperature also follows a linear dependence on ΔT^* . The best fit of the data is $\bar{T}_L - T_{\text{sat}} = 1.51\Delta T^*$. The Leidenfrost temperature in the impacting drops increases, since the thickness of the thermal boundary in the liquid and the propagation of the vaporization front are influenced by the flow in the spreading drop (Roisman, 2010).

The fact that the value of $T_L - T_{\text{sat}}$ is comparable with ΔT^* for a range of different liquids and substrates indicates that the initiation of the film boiling can indeed be explained by the propagation of the vaporization front along the substrate, assuming that the wall temperature does not exceed the critical value for the studied liquid. Note that propagation of the vaporization front is also influenced by the conditions at the moving contact line. This

explains the sensitivity of the Leidenfrost temperature to the substrate micro- and nano-morphology and wettability, identified in the existing literature. In summary the theoretical prediction describes very well the dependence of the Leidenfrost temperature on thermal fluid and substrate properties.

Table 6.1: Overview the thermal properties of the materials and the value of the Leidenfrost temperature. (as can be read in Tenzer et al. (2020).)

Study	Type of experiment	Fluid	Substrate material	$\epsilon_w, W_s^{1/2} / m^2K$	$T_L, ^\circ C$
This study	Spray	Water	Stainless steel 1.4841	8.8501e+03	342
This study	Spray	Water	Nickel Alloy 201	1.7892e+04	286
Hoogendoorn & den Hond (1974)	Spray	Water	Stainless steel 1.4301	9.0193e+03	371
Shoji et al. (1984)	Spray	Water	Nickel	1.8569e+04	321
Ito et al. (1991)	Spray	Water	Copper	3.6476e+04	134
Yao & Choi (1987)	Spray	Water	Copper with chrome plating	1.7831e+04	222
Choi & Yao (1987)	Spray	Water	Copper with chrome plating	1.7831e+04	253
Yao & Cox (2002)	Spray	Water	Copper with chrome plating	1.7831e+04	266
Bernardin et al. (1997)	Drop chain	Water	Copper with gold plating	2.7701e+04	225
Tran et al. (2012)	Drop	Water	Silicon wafer	9.7544e+03	480
Wang et al. (2019a)	Drop	Water	FeCrAl	6.5664e+03	445
Wang et al. (2019a)	Drop	Water	Sintered SiC	1.5733e+04	350
Wang et al. (2019a)	Drop	Water	Zr-4	5.1511e+03	531

Table 6.1 continued

Study	Type of experiment	Fluid	Substrate material	ϵ_w , $Ws^{1/2}/m^2K$	T_L , $^{\circ}C$
This study	Sessile drop	Water	Copper	3.6476e+04	124
Baumeister & Simon (1973)	Sessile drop	Water	Pyrex	2.1030e+03	700
Baumeister & Simon (1973)	Sessile drop	Water	Brass	1.9804e+04	233
Baumeister & Simon (1973)	Sessile drop	Water	Gold	2.8174e+04	184
Baumeister & Simon (1973)	Sessile drop	Water	Aluminium	2.0594e+04	210
Bernardin & Mudawar (1999)	Sessile drop	Water	Aluminium	2.0594e+04	175
Emmerson (1975)	Sessile drop	Water	Monel	9.5390e+03	316
Bernardin & Mudawar (1999)	Sessile drop	Water	Silver	3.2925e+04	157
Bernardin & Mudawar (1999)	Sessile drop	Water	Graphite	1.1690e+04	310
Wachters et al. (1966)	Sessile drop	Water	Gold	2.8174e+04	170
Wang et al. (2019a)	Sessile drop	Water	FeCrAl	6.5664e+03	379
Wang et al. (2019a)	Sessile drop	Water	Sintered SiC	1.5733e+04	310

Table 6.1 continued

Study	Type of experiment	Fluid	Substrate material	$\epsilon_w, Ws^{1/2}/m^2K$	$T_L, ^\circ C$
Wang et al. (2019a)	Sessile drop	Water	Zr-4	5.1511e+03	415
Baumeister & Simon (1973)	Sessile drop	Ethanol	Pyrex	2.1030e+03	360
Baumeister & Simon (1973)	Sessile drop	Ethanol	Aluminium	2.0594e+04	155
Baumeister & Simon (1973)	Sessile drop	Ethanol	Stainless steel	9.0193e+03	190
Bernardin & Mudawar (1999)	Sessile drop	Acetone	Aluminium	2.0594e+04	134
Bernardin & Mudawar (1999)	Sessile drop	Benzene	Aluminium	2.0594e+04	175
Bernardin & Mudawar (1999)	Sessile drop	FC-72	Aluminium	2.0594e+04	90

7 Conclusion and outlook

The present study deals with the investigation of transient spray cooling of a heated thick target. Spray cooling is used in a great variety of applications like cooling of high power electronics or quenching during steel making. Although widely used, the overall physical picture is not complete and predictions for the heat transfer are mainly of empirical nature. The drawback of these predictions is the lack of universality and therefore limited range in which they produce reliable results. To overcome this lack of knowledge several experiments of transient spray cooling were conducted. The initially homogeneously heated target was continuously cooled by various kinds of sprays. The local heat flux and surface temperature were acquired and compared to visual observations of the hydrodynamics during spray impact captured by a high speed observation system.

In the film boiling regime the spray impact can be treated as single drop impacts onto a dry surface and thus, can be regarded as a superposition of single drop impacts. With decreasing temperature, and after the Leidenfrost point has been passed, first small patches of water remain immediately after the drop impact. Subsequently, in the transition boiling regime, the amount of liquid remaining on the surface increases. Since the time spent in transition boiling is very short, it is reasonable to simplify and replace this condition by a jump of the heat flux. After passing the maximum heat flux (critical heat flux) the entire surface is covered by a liquid film.

The mass flux of the impinging spray turns out to be the key factor for achieving high cooling performance, whereas the mean droplet velocity and diameter have only a smaller influence. Oblique spray cooling of a surface, when the main spray direction is inclined towards the surface normal, results in a lower heat transfer compared to the perpendicular impact. The decrease turns out to be linearly dependent on the normal component of the spray mean velocity. Furthermore, the heat transfer is influenced by the initial spray water temperature. Cooling with hot water results in an decreased heat flux

and therefore lower cooling performance. Although this influence is present, it is rather small compared to that of the mass flux. Another strong influencing parameter is the material of the target substrate. Experiments on a nickel surface exhibited much higher heat fluxes compared to those on a stainless steel target. Thus, the heat flux is influenced by the thermal effusivity of the substrate: A higher thermal effusivity results in a higher heat flux.

The analysis of the heat transfer during spray cooling leads to a predictive model for the heat flux and surface temperature in the film boiling regime. The model is based on the superposition of single drop impacts and the assumption of a semi-infinite target. It accounts for different surface materials, spray properties, spray temperature and initial wall temperatures. There is excellent accordance between experimental results and theoretical predictions for all experimental data, covering a large range of parameters.

In the nucleate boiling regime the heat flux dependence on time indicates some kind of a universal character, which is nearly independent of the spray parameters. Assuming an instantaneous jump of the surface temperature to saturation temperature and a semi-infinite wall, results in a heat flux dependence on time, which is only influenced by the substrate material and the initial temperature. This upper bound of the heat flux in the nucleate boiling regime agrees well with experimental data as long as the semi-infinite assumption is valid. The upper bound is reached, even when spraying with low mass fluxes. This leads to the conclusion that in many cases the material is the limiting factor for heat flux and that further increasing the spray mass flux is of little benefit in the nucleate boiling regime.

A consequence of this insight is that it may be beneficial to construe a cooling strategy consisting of two stages: In the film boiling regime a dense spray having a high mass flux is used to achieve a high cooling efficiency. When the Leidenfrost point is passed and the nucleate boiling regime is reached, the mass flux is then reduced, since the heat flux is limited by the substrate and not by the spray. This would reduce the amount of spray fluid necessary while maintaining a high cooling performance. This is of paramount interest when special fluids are used instead of ordinary water. To what extent such a strategy would be advantageous will depend on the specific properties of the spray liquid, substrate material and temperature range of operation.

Measurements of the Leidenfrost point, identified as the minimum heat flux, indicate an independence on the spray characteristics, which is in strong contrast to findings in literature. Instead, the Leidenfrost point is solely influenced by the material of the target surface. A theoretical prediction based on the formation of a vaporization front, assuming that the inertial and viscous effects are comparable, agrees well with the experimental data for sessile drops and sprays.

The general outcomes and derived models from this study provide a comprehensive set of predictions and new knowledge for developing and improving reliable cooling processes which can be adapted to the special needs of each individual cooling application.

The fact that the heat flux at the first instants of spray impact above the Leidenfrost point is extremely high suggests another novel cooling strategy based on the results of this study. Since the thermal boundary layer inside the substrate has a significant influence on the cooling performance, it is promising to use pulsating sprays for increasing the cooling efficiency, i.e. the spray is continuously switched on and off. During the off-phase heat from the lower portions of the substrate can flow to the top and decrease the thermal boundary layer thickness. When the spray is again switched on, the spray impact takes place on a substrate which has a thin boundary layer, leading to an initial higher heat flux. Depending on the exact material properties and temperature range, this may lead to an increased overall heat flux while decreasing the required amount of spray fluid. The model developed in this study for the film boiling regime accounts for the very high heat flux at the initial phase of spray impact and can therefore be used to design and assess such spray strategies.

Nevertheless, a number of topics should be addressed in future investigations: Due to the short timescales in the transition boiling regime it seems reasonable to neglect this regime in some cases. But in others this simplification leads to large errors. Since the physics of the formation and growth of the liquid patches is not yet completely understood, no predictive models exist. Furthermore, there must be some lower bound under which no complete wetting of the surface can accrue. This boundary has to be identified and described. Therefore future studies should deal with the transition boiling regime.

Although the upper bound for the heat flux in the nucleate boiling regime agrees well with the experimental data in this study, it is in fact an upper bound which can only be valid if certain conditions are met. These circumstances must be investigated so that models can be developed which describe when to use this upper boundary. Additionally, a prediction for the heat flux, if the upper boundary is not reached, has to be developed.

The theory for the Leidenfrost temperature is only valid for temperatures below the critical temperature of the fluid, which is sufficient for many industrial applications. Future investigations should find explanations for the physical processes to achieve a prediction covering also the cases when the temperature exceeds the critical value. Furthermore, the experimental data found in literature for different fluids is often quite old and rather sparse. Acquisition of an accurate and complete set of Leidenfrost temperatures with dependence on various fluids and substrates could further enhance research in this field.

Nomenclature

Capital roman letters

A	m^2	surface
$A(\tau)$	$^\circ\text{C}/\text{s}$	function
B	-	incomplete beta function
C_1, C_2	-	empirical constants
D	m	drop diameter
D_{10}	m	mean drop diameter
L	J/kg	heat of evaporation
Q	J	heat
Re	-	Reynolds number
Re_S	-	spray Reynolds number
Re_v	-	Reynolds number associated with the vaporization front
S	$\text{s}^{-1/2}$	parameter
T	$^\circ\text{C}$	temperature
T_{f0}	$^\circ\text{C}$	initial fluid temperature
T_h	$^\circ\text{C}$	homogeneous nucleation temperature
T_i	$^\circ\text{C}$	surface temperature
T_{iL}	$^\circ\text{C}$	surface temperature at Leidenfrost point
T_L	$^\circ\text{C}$	Leidenfrost temperature
\bar{T}_L	$^\circ\text{C}$	mean Leidenfrost temperature
T_{Ld}	$^\circ\text{C}$	dynamic Leidenfrost temperature
T_{Ls}	$^\circ\text{C}$	static Leidenfrost temperature
T_{sat}	$^\circ\text{C}$	saturation temperature
T_{w0}	$^\circ\text{C}$	initial wall temperature
ΔT	$^\circ\text{C}$	temperature difference
ΔT_L	$^\circ\text{C}$	temperature difference
ΔT^*	$^\circ\text{C}$	characteristic superheat
\mathcal{T}	s	predicted parameter

U	m/s	mean droplet velocity
U_β	m/s	normal component of the droplet velocity during oblique spray impact at β
U_v	m/s	velocity of the vaporization front
We	-	Weber number
We_s	-	spray Weber number

Lowercase roman letters

a_i	-	series, $i \in [1, 2, \dots, \infty]$
b	-	dimensionless parameter
c_p	J/kgK	specific heat at constant pressure
d_T	m	diameter of target
h_T	m	height of target
h_{bubble}	m	thermal boundary layer in substrate due to vaporization bubble
h_i	m	boundary layer thickness in the phase i , $i \in [f, w]$
i	-	control variable
k	-	fitting parameter
m	kg	mass
\dot{m}	kg/m ² s	local mass flux
\dot{q}	W/m ²	local heat flux
\dot{q}_L	W/m ²	local heat flux at Leidenfrost point
\dot{q}_S	W/m ²	predicted local heat flux of entire cooling experiment
r	m	radial coordinate of the target
t	s	time
t_{CHF}	s	time at critical heat flux
t_L	s	time at Leidenfrost point
t_{bubble}	s	characteristic time of bubble formation
w	-	dimensionless parameter
z	m	wall-normal coordinate of the target

Capital greek letters

Θ	-	dimensionless surface temperature
----------	---	-----------------------------------

Φ - dimensionless heat flux

Lowercase greek letters

α m^2/s thermal diffusivity
 α_i m^2/s thermal diffusivity of the phase i , $i \in [\text{f}, \text{w}]$
 β $^\circ$ spray impact angle
 ϵ $\text{J}/\text{s}^{1/2}\text{m}^2\text{K}$ thermal effusivity
 ϵ_i $\text{J}/\text{s}^{1/2}\text{m}^2\text{K}$ thermal effusivity of the phase i , $i \in [\text{f}, \text{w}]$
 ζ - dimensionless parameter
 η kg/ms dynamic viscosity
 λ W/mK thermal conductivity
 λ_v W/mK thermal conductivity of the phase v
 ν m^2/s kinematic viscosity
 ν_f m^2/s kinematic viscosity of phase f
 ξ - dimensionless time
 ξ_L - dimensionless time at Leidenfrost point
 ρ kg/m^3 density
 ρ_f kg/m^3 density of phase f
 σ kg/s^2 surface tension
 σ_f kg/s^2 surface tension of phase f
 τ s parameter
 χ - fitting parameter

Abbreviations

CHF critical heat flux
DPSS diode pumped solid state
f fluid
film film boiling regime
HS high speed
IHCP inverse heat conduction problem
L Leidenfrost
min minimum
nucleate nucleate boiling regime
PC personal computer
PD phase Doppler
PDA phase Doppler analyzer

v	vapor
w	wall

Bibliography

- Abu-Zaid, M. (2003). An experimental study of the evaporation characteristics of emulsified liquid droplets. *Heat and Mass Transfer*, 40(9):737–741.
- Aktershev, S. P. & Ovchinnikov, V. V. (2011). Modeling of the vaporization front on a heater surface. *Journal of Engineering Thermophysics*, 20(1):77–88.
- Al-Ahmadi, H. M. & Yao, S. C. (2008). Spray cooling of high temperature metals using high mass flux industrial nozzles. *Experimental Heat Transfer*, 21(1):38–54.
- Albrecht, H.-E., Borys, M., Damaschke, N., & Tropea, C. (2013). *Laser Doppler and Phase Doppler Measurement Techniques*. Springer, Berlin Heidelberg.
- Araneo, L. & Tropea, C. (2000). Improving phase Doppler measurements in a diesel spray. In *SAE Technical Paper 2000-01-2047*.
- Auliano, M., Fernandino, M., Zhang, P., & Dorao, C. A. (2016). The Leidenfrost phenomenon on silicon nanowires. In *ASME 2016 14th International Conference on Nanochannels, Microchannels, and Minichannels, ICNMM 2016*. American Society of Mechanical Engineers.
- Aursand, E., Davis, S. H., & Ytrehus, T. (2018). Thermocapillary instability as a mechanism for film boiling collapse. *Journal of Fluid Mechanics*, 852:283–312.
- Avedisian, C. T. (1985). The homogeneous nucleation limits of liquids. *Journal of Physical and Chemical Reference Data*, 14(3):695–729.
- Avksentyuk, B. P. & Ovchinnikov, V. V. (2000). Shape of the vapor bubble upon explosive boiling. *Journal of Applied Mechanics and Technical Physics*, 41(2):317–318.

- Bar-Cohen, A., Arik, M., & Ohadi, M. (2006). Direct liquid cooling of high flux micro and nano electronic components. *Proceedings of the IEEE*, 94(8):1549–1570.
- Baumeister, K. J. & Simon, F. F. (1973). Leidenfrost temperature—Its correlation for liquid metals, cryogenes, hydrocarbons, and water. *Journal of Heat Transfer*, 95(2):166–173.
- Bernardin, J. D. & Mudawar, I. (1996). An experimental investigation into the relationship between temperature-time history and surface roughness in the spray quenching of aluminum parts. *Journal of Engineering Materials and Technology, Transactions of the ASME*, 118(1):127–134.
- Bernardin, J. D. & Mudawar, I. (1999). The Leidenfrost point: experimental study and assessment of existing models. *Journal of Heat Transfer*, 121(4):894.
- Bernardin, J. D. & Mudawar, I. (2004). A Leidenfrost point model for impinging droplets and sprays. *Journal of Heat Transfer*, 126(2):272.
- Bernardin, J. D., Stebbins, C. J., & Mudawar, I. (1997). Mapping of impact and heat transfer regimes of water drops impinging on a polished surface. *International Journal of Heat and Mass Transfer*, 40(2):247–267.
- Bertola, V. (2015). An impact regime map for water drops impacting on heated surfaces. *International Journal of Heat and Mass Transfer*, 85:430–437.
- Biance, A.-L., Clanet, C., & Qu  r  , D. (2003). Leidenfrost drops. *Physics of Fluids*, 15(6):1632.
- Bjornard, T. A. & Griffith, P. (1977). PWR blowdown heat transfer. In *Winter annual meeting of the American Society of Mechanical Engineers*, pages 17–41, Atlanta, GA, USA.
- Breitenbach, J., Kissing, J., Roisman, I. V., & Tropea, C. (2018a). Characterization of secondary droplets during thermal atomization regime. *Experimental Thermal and Fluid Science*, 98:516–522.
- Breitenbach, J., Roisman, I. V., & Tropea, C. (2017a). Drop collision with a hot, dry solid substrate: Heat transfer during nucleate boiling. *Physical Review Fluids*, 2(7):074301.

- Breitenbach, J., Roisman, I. V., & Tropea, C. (2017b). Heat transfer in the film boiling regime: Single drop impact and spray cooling. *International Journal of Heat and Mass Transfer*, 110:34–42.
- Breitenbach, J., Roisman, I. V., & Tropea, C. (2018b). From drop impact physics to spray cooling models: a critical review. *Experiments in Fluids*, 59(3):55.
- Cai, C., Mudawar, I., Liu, H., & Si, C. (2020). Theoretical Leidenfrost point (LFP) model for sessile droplet. *International Journal of Heat and Mass Transfer*, 146:118802.
- Carey, V. P. (2018). *Liquid Vapor Phase Change Phenomena: An Introduction to the Thermophysics of Vaporization and Condensation Processes in Heat Transfer Equipment*. Taylor and Francis, New York, 2. ed edition.
- Castanet, G., Caballina, O., & Lemoine, F. (2015). Drop spreading at the impact in the Leidenfrost boiling. *Physics of Fluids*, 27(6).
- Cebo-Rudnicka, A., Malinowski, Z., & Buczek, A. (2016). The influence of selected parameters of spray cooling and thermal conductivity on heat transfer coefficient. *International Journal of Thermal Sciences*, 110:52–64.
- Celata, G. P., Cumo, M., Mariani, A., & Zummo, G. (2006). Visualization of the impact of water drops on a hot surface: effect of drop velocity and surface inclination. *Heat and Mass Transfer*, 42(10):885–890.
- Chandra, S. & Avedisian, C. T. (1991). On the collision of a droplet with a solid surface. *Proceedings of the Royal Society A: Mathematical, Physical and Engineering Sciences*, 432(1884):13–41.
- Chaze, W., Caballina, O., Castanet, G., Pierson, J. F., Lemoine, F., & Maillet, D. (2019). Heat flux reconstruction by inversion of experimental infrared temperature measurements – Application to the impact of a droplet in the film boiling regime. *International Journal of Heat and Mass Transfer*, 128:469–478.
- Chen, R.-H. H., Chow, L. C., & Navedo, J. E. (2002). Effects of spray characteristics on critical heat flux in subcooled water spray cooling. *International Journal of Heat and Mass Transfer*, 45(19):4033–4043.

- Chen, S. J. & Tseng, A. A. (1992). Spray and jet cooling in steel rolling. *International Journal of Heat and Fluid Flow*, 13(4):358–369.
- Cheng, W. L., Zhang, W. W., Chen, H., & Hu, L. (2016). Spray cooling and flash evaporation cooling: The current development and application. *Renewable and Sustainable Energy Reviews*, 55:614–628.
- Choi, K. J. & Yao, S. C. (1987). Mechanisms of film boiling heat transfer of normally impacting spray. *International Journal of Heat and Mass Transfer*, 30(2):311–318.
- Cox, T. L. & Yao, S. C. (1999). Heat transfer of sprays of large water drops impacting on high temperature surfaces. *Journal of Heat Transfer*, 121(2):446–450.
- Ebadian, M. A. & Lin, C. X. (2011). A review of high-heat-flux heat removal technologies. *Journal of Heat Transfer*, 133(11):110801.
- Emmerson, G. S. (1975). The effect of pressure and surface material on the Leidenfrost point of discrete drops of water. *International Journal of Heat and Mass Transfer*, 18(3):381–386.
- Estes, K. A. & Mudawar, I. (1995). Correlation of sauter mean diameter and critical heat flux for spray cooling of small surfaces. *International Journal of Heat and Mass Transfer*, 38(16):2985–2996.
- Gottfried, B. S., Lee, C. J., & Bell, K. J. (1966). The Leidenfrost phenomenon: film boiling of liquid droplets on a flat plate. *International Journal of Heat and Mass Transfer*, 9(11):1167–1188.
- Hiroyasu, H., Kadota, T., & Senda, T. (1974). Droplet evaporation on a hot surface in pressurized and heated ambient gas. *Bulletin of JSME*, 17(110):1081–1087.
- Hofmann, J. (2019). *Experimental investigation of the Leidenfrost point during spray- and single drop impact*. Master’s thesis, Technische Universität Darmstadt, Darmstadt, Germany.
- Hoogendoorn, C. J. & den Hond, R. (1974). Leidenfrost temperature and heat transfer coefficients for water sprays impinging on a hot surface. In *IFTH International Heat Transfer Conference*, volume 4, pages 135–138.

- Itaru, M. & Kunihide, M. (1978). Heat transfer characteristics of evaporation of a liquid droplet on heated surfaces. *International Journal of Heat and Mass Transfer*, 21(5):605–613.
- Ito, T., Takata, Y., Mousa, M. M. M., & Yoshikai, H. (1991). Studies on the water cooling of hot surfaces (experiment of spray cooling). *Memoirs of the Faculty of Engineering, Kyushu University*, 51(2):119–144.
- Jerome, B. P. (1960). Transition boiling heat transfer from a horizontal surface. Technical report, Massachusetts Institute of Technology, Heat Transfer Laboratory no. 17, Cambridge, Mass.
- Kakac, S. & Bon, B. (2008). A review of two-phase flow dynamic instabilities in tube boiling systems. *International Journal of Heat and Mass Transfer*, 51:399–433.
- Kaupe, T. (2017). *Design and setup of a spray patternator for measuring the mass flux density*. Master's thesis, Technische Universität Darmstadt, Darmstadt, Germany.
- Kim, H., Truong, B., Buongiorno, J., & Hu, L. W. (2012). Effects of micro/nano-scale surface characteristics on the Leidenfrost point temperature of water. *Journal of Thermal Science and Technology*, 7(3):453–462.
- Kim, J. (2007). Spray cooling heat transfer: The state of the art. *International Journal of Heat and Fluid Flow*, 28(4):753–767.
- Klinzing, W. P., Rozzi, J. C., & Mudawar, I. (1992). Film and transition boiling correlations for quenching of hot surfaces with water sprays. *Journal of Heat Treating*, 9(2):91–103.
- Kruse, C., Anderson, T., Wilson, C., Zuhlke, C., Alexander, D., Gogos, G., & Ndao, S. (2013). Extraordinary shifts of the Leidenfrost temperature from multiscale micro/nanostructured surfaces. *Langmuir*, 29(31):9798–9806.
- Labergue, A., Gradeck, M., & Lemoine, F. (2015). Comparative study of the cooling of a hot temperature surface using sprays and liquid jets. *International Journal of Heat and Mass Transfer*, 81:889–900.
- Lefebvre, A. (1988). *Atomization and Sprays*. CRC Press, Boca Raton.

- Leidenfrost, J. G. (1966). On the fixation of water in diverse fire. *International Journal of Heat and Mass Transfer*, 9(11):1153–1166.
- Liang, G. & Mudawar, I. (2017a). Review of drop impact on heated walls. *International Journal of Heat and Mass Transfer*, 106:103–126.
- Liang, G. & Mudawar, I. (2017b). Review of spray cooling – Part 1: Single-phase and nucleate boiling regimes, and critical heat flux. *International Journal of Heat and Mass Transfer*, 115(September):1174–1205.
- Liang, G. & Mudawar, I. (2017c). Review of spray cooling – Part 2: High temperature boiling regimes and quenching applications. *International Journal of Heat and Mass Transfer*, 115:1206–1222.
- Mizikar, E. A. (1970). Spray cooling investigation for continuous casting of billets and blooms. *Iron and Steel Engineer*, 47(6):53–60.
- Monde, M., Arima, H., Liu, W., Mitutake, Y., & Hammad, J. A. (2003). An analytical solution for two-dimensional inverse heat conduction problems using Laplace transform. *International Journal of Heat and Mass Transfer*, 46(12):2135–2148.
- Mudawar, I. (2001). Assessment of high-heat-flux thermal management schemes. *IEEE Transactions on Components and Packaging Technologies*, 24(2):122–141.
- Mudawar, I. & Deiters, T. A. (1994). A universal approach to predicting temperature response of metallic parts to spray quenching. *International Journal of Heat and Mass Transfer*, 37(3):347–362.
- Nimi, M., Pri, O., Ulivanju, K., Raudensky, M., Hnizdil, M., Hwang, J. Y., Lee, S. H., & Kim, S. Y. (2012). Influence of the water temperature on the cooling intensity of mist nozzles in continuous casting. *Materiali in tehnologije*, 46(3):311–315.
- Nižetić, S., Čoko, D., Yadav, A., & Grubišić-Čabo, F. (2016). Water spray cooling technique applied on a photovoltaic panel: The performance response. *Energy Conversion and Management*, 108:287–296.

- Nukiyama, S. (1966). The maximum and minimum values of the heat Q transmitted from metal to boiling water under atmospheric pressure. *International Journal of Heat and Mass Transfer*, 9(12):1419–1433.
- Okuyama, K., Kim, J. H., Mori, S., & Iida, Y. (2006). Boiling propagation of water on a smooth film heater surface. *International Journal of Heat and Mass Transfer*, 49(13-14):2207–2214.
- Özışık, M. N. (1980). *Heat conduction*. John Wiley & Sons, New York, Chichester, Brisbane, Toronto.
- Pham, M. K. (2018). *Study of the influence of the fluid temperature on the heat transfer and hydrodynamics during spray cooling*. Bachelor's thesis, Technische Universität Darmstadt, Darmstadt, Germany.
- Pola, A., Gelfi, M., & La Vecchia, G. M. (2013). Simulation and validation of spray quenching applied to heavy forgings. *Journal of Materials Processing Technology*, 213(12):2247–2253.
- Puschmann, F. & Specht, E. (2004). Transient measurement of heat transfer in metal quenching with atomized sprays. *Experimental Thermal and Fluid Science*, 28(6):607–615.
- Quéré, D. (2013). Leidenfrost dynamics. *Annual Review of Fluid Mechanics*, 45(1):197–215.
- Roisman, I. V. (2010). Fast forced liquid film spreading on a substrate: Flow, heat transfer and phase transition. *Journal of Fluid Mechanics*, 656:189–204.
- Roisman, I. V., Breitenbach, J., & Tropea, C. (2018). Thermal atomisation of a liquid drop after impact onto a hot substrate. *Journal of Fluid Mechanics*, 842:87–101.
- Romashevskiy, S. A., Agranat, M. B., & Dmitriev, A. S. (2016). Thermal training of functional surfaces fabricated with femtosecond laser pulses. *High Temperature*, 54(3):461–465.
- Sargunanathan, S., Elango, A., & Mohideen, S. T. (2016). Performance enhancement of solar photovoltaic cells using effective cooling methods: A review. *Renewable and Sustainable Energy Reviews*, 64:382–393.

- Shoji, M., Wakunaga, T., & Kodama, K. (1984). Heat transfer from a heated surface to impinging subcooled droplets : Heat transfer characteristics in non-wetting region. *Transactions of the Japan Society of Mechanical Engineers Series B*, 50(451):716–723.
- Sienski, K., Eden, R., & Schaefer, D. (1996). 3-D electronic interconnect packaging. In *IEEE Aerospace Applications Conference Proceedings*, volume 1, pages 363–373. IEEE.
- Sozbir, N., Chang, Y. W., & Yao, S. C. (2003). Heat transfer of impacting water mist on high temperature metal surfaces. *Journal of Heat Transfer*, 125(1):70.
- Sozbir, N., Yigit, C., Issa, R. J., Yao, S.-C., Guven, H. R., & Ozcelebi, S. (2010). Multiphase spray cooling of steel plates near the Leidenfrost temperature-experimental studies and numerical modeling. *Atomization and Sprays*, 20(5):387–405.
- Spiegler, P., Hopenfeld, J., Silberberg, M., Bumpus, C. F., & Norman, A. (1963). Onset of stable film boiling and the foam limit. *International Journal of Heat and Mass Transfer*, 6(11):987–989.
- Staat, H. J. J., Tran, T., Geerdink, B., Riboux, G., Sun, C., Gordillo, J. M., & Lohse, D. (2015). Phase diagram for droplet impact on superheated surfaces. *Journal of Fluid Mechanics*, 779:R3.
- Staszal, C. & Yarin, A. L. (2018). Exponential vaporization fronts and critical heat flux in pool boiling. *International Communications in Heat and Mass Transfer*, 98:171–176.
- Stutz, B. & Simões-Moreira, J. R. (2013). Onset of boiling and propagating mechanisms in a highly superheated liquid - The role of evaporation waves. *International Journal of Heat and Mass Transfer*, 56(1-2):683–693.
- Takata, Y., Hidaka, S., Cao, J. M., Nakamura, T., Yamamoto, H., Masuda, M., & Ito, T. (2005). Effect of surface wettability on boiling and evaporation. *Energy*, 30:209–220.

- Tartarini, P., Lorenzini, G., & Randi, M. R. (1999). Experimental study of water droplet boiling on hot, non-porous surfaces. *Heat and Mass Transfer*, 34(6):437–447.
- Tenzer, F. M., Hofmann, J., Roisman, I. V., & Tropea, C. (2020). Leidenfrost temperature in sprays: role of the substrate and liquid properties. *Manuscript submitted for publication*, (arXiv:2001.05426).
- Tenzer, F. M., Pham, M. K., Roisman, I. V., & Tropea, C. (2019a). Fast spray cooling: Effect of the liquid temperature. In *HEFAT 2019, 14th International Conference on Heat Transfer, Fluid Mechanics and Thermodynamics*, pages 706–710, Wicklow, Ireland.
- Tenzer, F. M., Roisman, I. V., & Tropea, C. (2018). Spray cooling in the nucleate boiling regime: Hydrodynamics and heat transfer. In *ICLASS 2018, 14th Triennial International Conference on Liquid Atomization and Spray Systems*, page 123, Chicago, IL.
- Tenzer, F. M., Roisman, I. V., & Tropea, C. (2019b). Fast transient spray cooling of a hot thick target. *Journal of Fluid Mechanics*, 881:84–103.
- Testa, P. & Nicotra, L. (2009). Influence of pressure on the Leidenfrost temperature and on extracted heat fluxes in the transient mode and low pressure. *Journal of Heat Transfer*, 108(4):916.
- Tran, T., Staat, H. J. J., Prosperetti, A., Sun, C., & Lohse, D. (2012). Drop impact on superheated surfaces. *Physical Review Letters*, 108(3):1–5.
- Tropea, C. (2011). Optical particle characterization in flows. *Annual Review of Fluid Mechanics*, 43(1):399–426.
- Tropea, C., Xu, T.-H., Onofri, F., Géhan, G., Haugen, P., & Stieglmeier, M. (1996). Dual-mode phase-Doppler anemometer. *Particle & Particle Systems Characterization*, 13(2):165–170.
- Wachters, L. H., Bonne, H., & van Nouhuis, H. J. (1966). The heat transfer from a hot horizontal plate to sessile water drops in the spheroidal state. *Chemical Engineering Science*, 21(10):923–936.

- Wang, Z., Qu, W., Xiong, J., Zhong, M., & Yang, Y. (2019a). Investigation on effect of surface properties on droplet impact cooling of cladding surfaces. *Nuclear Engineering and Technology*.
- Wang, Z. F., Xiong, J., Yao, W., Qu, W., & Yang, Y. (2019b). Experimental investigation on the Leidenfrost phenomenon of droplet impact on heated silicon carbide surfaces. *International Journal of Heat and Mass Transfer*, 128:1206–1217.
- Wendelstorf, J., Spitzer, K. H., & Wendelstorf, R. (2008). Spray water cooling heat transfer at high temperatures and liquid mass fluxes. *International Journal of Heat and Mass Transfer*, 51(19-20):4902–4910.
- Wolter, S. (2018). *Spray characterization of one- and two-component nozzles for the investigation of spray cooling of hot surfaces*. Master's thesis, Technische Universität Darmstadt, Darmstadt, Germany.
- Woodfield, P. L., Monde, M., & Mitsutake, Y. (2006). Improved analytical solution for inverse heat conduction problems on thermally thick and semi-infinite solids. *International Journal of Heat and Mass Transfer*, 49(17-18):2864–2876.
- Xu, F. & Gadala, M. S. (2006). Heat transfer behavior in the impingement zone under circular water jet. *International Journal of Heat and Mass Transfer*, 49(21-22):3785–3799.
- Yang, J., Chow, L. C., & Pais, M. R. (1996). Nucleate boiling heat transfer in spray cooling. *Journal of Heat Transfer*, 118(3):668.
- Yao, S. C. & Cai, K. Y. (1988). The dynamics and Leidenfrost temperature of drops impacting on a hot surface at small angles. *Experimental Thermal and Fluid Science*, 1(4):363–371.
- Yao, S. C. & Choi, K. J. (1987). Heat transfer experiments of mono-dispersed vertically impacting sprays. *International Journal of Multiphase Flow*, 13(5):639–648.
- Yao, S. C. & Cox, T. L. (2002). A general heat transfer correlation for impacting water sprays on high-temperature surfaces. *Experimental Heat Transfer*, 15(4):207–219.

- Yarin, A. L., Roisman, I. V., & Tropea, C. (2017). *Collision phenomena in liquids and solids*. Cambridge University Press, Cambridge.
- Zuber, N. (1958). On the stability of boiling heat transfer. *Transactions of the American Society of Mechanical Engineers*, 80.

List of Figures

1.1	Heat transfer coefficient of different cooling technologies. . . .	2
1.2	Exemplary temporal evolution of the temperature 1 mm below the surface of a workpiece during a hot forging process. . . .	3
1.3	Exemplary evolution of the heat flux as a function of the surface temperature during spray cooling.	5
1.4	Dependence of the Leidenfrost temperature on the spray Weber number.	8
2.1	Schematic of experimental setup.	14
2.2	Detailed sketch of the atomizer and water supply system used for spray generation.	15
2.3	Mean droplet diameter and velocity as a function of radial position.	19
2.4	Mass flux as a function of the radial position.	20
2.5	Droplet velocity versus diameter for various atomizer in the center region below the atomizer.	21
2.6	Heated target equipped with watertight housing and ventilation slit.	23
2.7	Heated target and additional components inside the watertight housing.	25
2.8	Sketch of the sectional view of the heated target showing the thermocouple positions. Dimensions are in mm.	27
2.9	Sketch of the thermocouples having an open measuring tip which is aligned with the shield.	28
2.10	Field of view for configuration with <i>Tamron</i> 180mm macro optical lens.	29
2.11	Field of view for configuration with <i>Questar QM-100</i> long distance microscope objective lens.	29

3.1	Calculated temperature T inside the substrate as a function of the depth z for different times t	32
3.2	Typical temporal evolution of the surface temperature $T_i(t)$ and instantaneous local heat flux $\dot{q}(t)$	33
3.3	Typical evolution of the instantaneous local heat flux $\dot{q}(t)$ as a function of the surface temperature $T_i(t)$	33
3.4	Spray cooling regimes at different surface temperatures $T_i(t)$ around the Leidenfrost point.	34
3.5	Phenomena of spray impact regimes at different surface temperatures $T_i(t)$	36
3.6	Position of the wetting front that follows the Leidenfrost point at different instants of time t	39
3.7	Sketch of the hydrodynamics occurring during spray impact.	41
3.8	Influence of mass flux \dot{m} on the heat transfer.	43
3.9	Influence of the mean droplet velocity on the heat transfer.	44
3.10	Influence of different spray produced by a pneumatic atomizer.	45
3.11	Sketch of oblique spray impact.	46
3.12	Influence of the spray impact angle β	47
3.13	Scaled heat flux in the film boiling regime \dot{q}_β/\dot{q} as a function of the scaled impact velocity U_β/U for different spray impact angles β	48
3.14	Heat flux dependence on the surface temperature for different spray water temperatures.	48
3.15	Heat flux dependence on the surface temperature for different spray water temperatures. Only film boiling regime, Leidenfrost point and beginning of transition boiling regime are shown.	50
3.16	Heat flux dependence on the surface temperature for different spray water temperatures. The inserts show the conditions at the surface at the corresponding surface temperature.	51
3.17	Heat flux as a function of the initial spray water temperature. The data and spray parameters are equal to Fig. 3.15.	53
3.18	Influence of the initial wall temperature T_{w0} for a small mass flux.	54
3.19	Influence of the initial wall temperature T_{w0} for a large mass flux of $\dot{m} = 9.3 \text{ kg/m}^2\text{s}$	55

3.20	Influence of the substrate material on the heat transfer for a constant rather sparse spray.	56
3.21	Influence of the substrate material on the heat transfer for a constant rather dense spray.	57
3.22	Influence of the surface roughness on the heat transfer, for a small mass flux of $1 \text{ kg/m}^2\text{s}$	58
3.23	Influence of the surface roughness on the heat transfer, for a small mass flux of $3.1 \text{ kg/m}^2\text{s}$	60
4.1	Theoretically predicted evolution of the dimensionless quantities as functions of the dimensionless time ξ in the film boiling regime.	65
4.2	Evolution of the dimensionless quantities for the stainless steel target as a function of the dimensionless time ξ	66
4.3	Evolution of the dimensionless quantities for the hot-work tool steel target as a function of the dimensionless time ξ	68
4.4	Evolution of the dimensionless quantities for the nickel target as a function of the dimensionless time ξ	69
4.5	Evolution of the dimensionless quantities for the nickel target sprayed with a pneumatic atomizer as a function of the dimensionless time ξ	70
4.6	Exemplary comparison between one experiment and the theoretical prediction in the film boiling regime.	72
4.7	Heat flux as a function of the initial spray water temperature.	73
4.8	Evolution of the heat flux as a function of time for an exemplary experiment.	74
5.1	Scaling of the heat flux plotted as a function of time for the stainless steel target.	80
5.2	Scaling of the heat flux plotted as a function of time for the target built of hot-work tool steel.	81
5.3	Scaling of the heat flux plotted as a function of time for the nickel target.	82
5.4	Exemplary comparison between one experiment and the theoretical prediction in the nucleate boiling regime.	83

5.5	Exemplary comparison between one experiment and the theoretical prediction of the entire cooling process.	85
6.1	Determination of the Leidenfrost point T_L as the temperature at the minimum heat flux q_{\min}	88
6.2	Leidenfrost temperature T_L as a function of the mass flux \dot{m}	89
6.3	Dependence of the Leidenfrost temperature T_L on the spray properties.	90
6.4	Dependence of the Leidenfrost temperature T_L on dimensionless numbers.	90
6.5	Comparison between own data and the correlation proposed by Al-Ahmadi & Yao (2008) (Eq. (1.2)).	92
6.6	Comparison between own data and the correlation proposed by Bernardin & Mudawar (2004) (Eq. (1.6)).	93
6.7	Comparison between own data, those of other researchers and the correlation proposed by Yao & Cox (2002).	93
6.8	Possible mechanisms of film boiling.	95
6.9	A sessile drop on a heated copper surface at different surface temperatures T_i	96
6.10	Substrate superheat at the Leidenfrost point, $T_L - T_{\text{sat}}$, as a function of ΔT^* for sessile drops.	98
6.11	Mean substrate superheat at the Leidenfrost point $\bar{T}_L - T_{\text{sat}}$ as a function of ΔT^* for spray cooling.	99

List of Tables

2.1	Overview of atomizers used for the experiments and their operational parameters.	16
2.2	Parameters of the phase Doppler measurement system.	17
2.3	Overview of targets and material parameters used of cooling experiments.	23
4.1	Typical conditions of spray cooling experiments of this study.	64
6.1	Overview the thermal properties of the materials and the value of the Leidenfrost temperature.	100